

# MELTING IN TEMPERATURE SENSITIVE SUSPENSIONS

Ahmed M. Alsayed

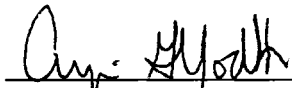
A Dissertation

in

Physics and Astronomy

Presented to the Faculties of the University of Pennsylvania in Partial  
Fulfillment of the Requirements for the Degree of Doctor of Philosophy


2006



---

Arjun G. Yodh

Supervisor of Dissertation



---

Andrea J. Liu

Graduate Group Chairperson

UMI Number: 3225424

### INFORMATION TO USERS

The quality of this reproduction is dependent upon the quality of the copy submitted. Broken or indistinct print, colored or poor quality illustrations and photographs, print bleed-through, substandard margins, and improper alignment can adversely affect reproduction.

In the unlikely event that the author did not send a complete manuscript and there are missing pages, these will be noted. Also, if unauthorized copyright material had to be removed, a note will indicate the deletion.

**UMI<sup>®</sup>**

---

UMI Microform 3225424

Copyright 2006 by ProQuest Information and Learning Company.

All rights reserved. This microform edition is protected against unauthorized copying under Title 17, United States Code.

ProQuest Information and Learning Company  
300 North Zeeb Road  
P.O. Box 1346  
Ann Arbor, MI 48106-1346

© Copyright

by

Ahmed M. Alsayed

# Acknowledgements

During the course of my graduate study I benefited from many people, in Yodh's group, in the physics department and in other places at the university. I would like to thank first, Arjun G. Yodh, who supervised me in my study. He gave me freedom, guided and supported me to explore many new ideas. Some of them worked and others didn't. I also would like to thank the "Ministry of Higher Education" in Egypt who supported me for few years and gave me the opportunity to study in United States. Besides Arjun I would like to thank other members of the faculty in the physics department who also played advisory roles. I would like to thank Tom Lubensky, who was the first to advise me to work with NIPA polymer. I've benefited a lot from Peter Collings during his sabbatical leave in our department and I thank him too. I have also had many useful discussions with Randy Kamien, Douglas Durian, Andrea Liu, and Jay Kikkawa. I would like to thank Paul Janmey, who let me use his lab for many weeks to grow *fd* virus. Finally I also acknowledge the help of Dennis Discher, who showed me how to polymerize NIPA.

Perhaps I owe the most to fellow postdocs and graduate students in Arjun's lab. They were supportive, and without their help most of this thesis wouldn't have been possible. I especially want to thank Zvonimir Dogic and Jian Zhang. They helped me to understand the field in the beginning of my graduate career. They also taught me how to synthesis colloidal particles. Zvonimir taught me how to grow *fd* virus, while Jian taught me how to synthesis PMMA colloidal spheres. Without their help this thesis wouldn't be possible.

There are many other persons I have worked with during my stay and I think I owe my thanks to them too. They are Mohammad Islam, Jean-Christophe Loudet, Subrata Sanyal, Daniel Chen, Mateusz Bryning, Keng-hui Lin, M. Nobili, Lawrence Hough, and Yilong Han.

Finally, I thank my parents and my family for their understanding and support.

# Abstract

## MELTING IN TEMPERATURE SENSITIVE SUSPENSIONS

Ahmed M. Alsayed

Arjun G. Yodh

We describe two experimental studies about melting in colloidal systems. In particular we studied melting of 1-dimensional lamellar phases and 3-dimensional colloidal crystals.

In the first set of experiments we prepared suspensions composed of rodlike *fd* virus and the thermosensitive polymer, poly(N-isopropylacrylamide). The phase diagram of this systems is temperature and concentration dependent. Using video microscopy, we directly observed melting of lamellar phases and single lamellae into nematic phase. We found that lamellar phases swell with increasing temperature before melting into the nematic phase. The highly swollen lamellae can be superheated as a result of topological nucleation barriers that slow the formation of the nematic phase.

In another set of experiments we prepared colloidal crystals from thermally responsive microgel spheres. The crystals are equilibrium close-packed three-dimensional structures. Upon increasing the temperature slightly above room temperature, particle volume fraction decreased from 0.74 to less than 0.5. Using video microscopy, we observed pre-melting at grain boundaries and dislocations within bulk colloidal crystals. Premelting is the localized loss of crystalline order at surfaces and defects at sample volume fractions above the bulk melting transition. Particle tracking revealed increased disorder in crystalline regions bordering defects, the amount of which depends on the type of defect, distance from the defect, and particle volume fraction. In total these observations suggest that interfacial free energy is the crucial parameter for premelting in colloidal and in atomic scale crystals.

# Contents

<b>Acknowledgements</b>	<b>iii</b>
<b>Abstract</b>	<b>iv</b>
<b>List of Tables</b>	<b>viii</b>
<b>List of Figures</b>	<b>xvi</b>
<b>1 Introduction</b>	<b>1</b>
<b>2 Colloidal Crystal and Crystal Defects</b>	<b>6</b>
2.1 Equilibrium Phase Behavior of Hard Sphere Suspensions . . . . .	6
2.2 Crystal Defects . . . . .	8
2.3 Point Defects . . . . .	9
2.3.1 Linear Defects . . . . .	11
2.3.2 Planar Defects . . . . .	12
2.3.2.1 Grain Boundaries . . . . .	12
2.3.2.2 Shockley Partial Dislocation in fcc Crystals . . . . .	13
<b>3 Melting &amp; Phase transitions (Solid-Liquid)</b>	<b>17</b>
3.1 Phase Transitions . . . . .	17
3.2 Melting and Premelting of Crystal . . . . .	24
3.2.1 Lindemann Criterion of Melting . . . . .	24

3.2.2	Dislocation mediated Melting . . . . .	26
3.2.3	Melting of 2D systems . . . . .	28
3.3	Surface Melting . . . . .	29
3.4	Experiments on Surface Melting . . . . .	34
3.5	Phenomenological Theory on Surface Melting . . . . .	41
3.6	Molecular-Dynamics Simulations of Surface Melting . . . . .	43
3.7	Density Functional Theory . . . . .	44
3.8	Density Functional Theory and melting . . . . .	48
3.9	Grain Boundary Premelting . . . . .	49
<b>4</b>	<b>Phase Transitions in Liquid Crystals</b>	<b>53</b>
4.1	fd Virus and Its Phase Behavior . . . . .	53
<b>5</b>	<b>Temperature Sensitive Polymers</b>	<b>57</b>
5.1	Thermoresponsive poly(N-isopropylacrylamide) polymers and colloids . .	57
<b>6</b>	<b>Sample Preparation and Characterization</b>	<b>61</b>
6.1	Emulsion Polymerization . . . . .	61
6.1.1	Free Radical Polymerization . . . . .	62
6.1.2	Polymerization In Emulsion Systems . . . . .	63
6.1.3	Aqueous Colloidal Synthesis Using Emulsion Polymerization . .	66
6.2	Synthesis of NIPA Particles . . . . .	68
6.3	Synthesis of NIPA Polymer . . . . .	71
6.4	Dynamic Light Scattering . . . . .	72
6.5	Preparation of the Filamentous Bacteriophage <i>fd</i> . . . . .	79
6.5.1	Colonize Bacteria in Hard Media . . . . .	79
6.5.2	Large Scale Bacterial and <i>fd</i> Growth . . . . .	80
6.5.3	Isolating <i>fd</i> virus from Bacteria . . . . .	80
6.5.4	Purifying <i>fd</i> virus . . . . .	81

6.5.5	Determining $fd$ concentration . . . . .	81
<b>7</b>	<b>Video Microscopy</b>	<b>82</b>
7.1	Optical Microscopes . . . . .	82
7.2	Video Microscopy and Particle Tracking . . . . .	87
<b>8</b>	<b>Premelting at Defects Within Bulk Colloidal Crystals</b>	<b>91</b>
8.1	Introduction . . . . .	91
8.2	Microscopy and temperature control . . . . .	93
8.3	Sample preparation . . . . .	93
8.4	Positional fluctuations . . . . .	97
8.5	Premelting from grain boundaries . . . . .	105
8.6	Premelting from dislocations . . . . .	107
8.7	Conclusion . . . . .	110
<b>9</b>	<b>Melting of lamellar phases in temperature sensitive colloid-polymer suspen- sions</b>	<b>113</b>
9.1	Introduction . . . . .	113
9.2	Sample preparation . . . . .	115
9.3	Melting of Bulk Lamellar Phase . . . . .	116
9.4	Melting of Lamellar Droplets and Isolated Lamellar Membranes . . . . .	118
9.5	Stability of Isolated Lamellar Membranes . . . . .	122
9.6	Conclusion . . . . .	124
<b>10</b>	<b>Conclusions and Future Work</b>	<b>125</b>
	<b>Bibliography</b>	<b>128</b>



# List of Tables

6.1	Diameter (D) and polydispersity (Poly.) of NIPA particles at two different temperatures . . . . .	77
-----	---	----

# List of Figures

2.1	Phase behavior of monodisperse hard colloidal spheres. . . . .	8
2.2	Some common point defects in crystal lattice. $V$ is a vacancy. $II$ is a interstitial impurity. $SI$ is a self-interstitial. $S$ is a substitutional. If the substitutional atom is bigger (smaller) than the original lattice atom, the created stress goes outward (inward). Frenkel and Schottky defects occur in ionic crystals. . . . .	10
2.3	An edge dislocation. Burger vector $b$ is parallel to Burger circuit. . . . .	12
2.4	A screw dislocation. Burger vector $b$ is normal to Burger circuit. . . . .	13
2.5	Small angle grain boundary illustrated as an array of dislocations. Simple geometry can show that the angle between the two grains can be calculated from; $\theta \simeq \frac{d}{L}$ , where $d$ is the lattice constant and $L$ is the dislocation separation. . . . .	14
2.6	Stacking spheres in close-packed structure. The first layer is in position A, the second layer either take position B or C, both positions cannot be occupied in the same time. The vectors a, b, and c connect positions A, B, and C as shown in the figure. The vectors a, b, and c are $\frac{1}{6}[\bar{2}11]$ , $\frac{1}{6}[1\bar{2}1]$ , and $\frac{1}{6}[11\bar{2}]$ respectively. The vectors d, e, and f connect the nearest A positions. The vectors d, e, and f are $\frac{1}{2}[\bar{1}10]$ , $\frac{1}{2}[10\bar{1}]$ , and $\frac{1}{2}[0\bar{1}1]$ respectively. 15	15

2.7	Stacking fault in a face-centered-cubic structure. The second layer in the right-lower part stacked in the C position instead of the B position. The fault ended inside the crystal and the faulted region (lower-right) displaced by $\frac{1}{6}[11\bar{2}]$ . The boundary between the faulted region and the normal region (left) is a Shockley partial dislocation. If the two region stack normally after the second layer, the partial dislocation will be two gaps cut the crystal along (100) plane and have $120^\circ$ with respect one to the other. . . . .	16
3.1	Gibbs free energy as a function of $1/T$ for two phases <i>A</i> and <i>B</i> . . . . .	19
3.2	P-T phase diagram of gas-liquid-solid phases of a pure material. . . . .	20
3.3	Order parameter as a function of temperature in a first-order phase transition. . . . .	21
3.4	Order parameter as a function of temperature in a second-order phase transition. . . . .	21
3.5	The free energy as a function of order parameter for a second-order phase transition for temperatures less than, equal to, and greater than the phase transition temperature. . . . .	23
3.6	The free energy as a function of order parameter for a first-order phase transition for temperatures less than, equal to, and greater than the phase transition temperature. . . . .	23
3.7	A bound pair of dislocations. This configuration has a little effect on the translational and orientational order. Blue spheres represent the extra layer due to dislocation, pink sphere has seven nearest neighbors, and red sphere has five nearest neighbors. . . . .	30
3.8	A single dislocation has a large effect on the translational order while the rotational order is not effected substantially. Blue spheres represent the extra layer due to dislocation, pink sphere has seven nearest neighbors, and red sphere has five nearest neighbors. . . . .	31

3.9	Complete wetting and partial wetting of a solid by its own melt. . . . .	33
3.10	Schematic representation of shadowing and blocking effects of ion beam scattering of $[110]$ surface. Ion beam and detector are aligned with the $[\bar{1}01]$ and $[011]$ directions. . . . .	35
3.11	Experimental energy spectra obtained from ion backscattering in the temperature range 295-600.8 K, (a) to (g). $T_m = 600.7K$ [77, 76]. . . . .	36
3.12	No. of molten layers as a function of temperature of $[110]$ lead surface. [77, 76]. . . . .	36
3.13	Fcc (110) surface . . . . .	40
3.14	Fcc (110) surface . . . . .	40
3.15	Density profile throughout the interface of a liquid-gas system . . . . .	47
3.16	Density profile throughout the interfaces of a solid-liquid-gas system . . .	49
4.1	Optical microscopy micrograph of smectic phase in $fd$ virus suspension.	54
4.2	Phase behavior of $fd$ virus suspensions at different ionic strengths [61]. .	55
4.3	Phases behavior of a hard rod suspension. The illustration shows stable phases that appear in a system of hard rods. The transitions in hard particle suspensions are temperature independent; concentration is the only parameter that determines the phase diagram. Hard rods form stable isotropic, nematic, and smectic phases with increasing rod concentration.	56
5.1	NIPA monomer molecule. . . . .	58
5.2	Equilibrium radius of N-isopropylacrylamide/sodium acrylate copolymer gels in pure water plotted as a function of temperature The mM value indicates the concentration of ionizable monomer, sodium acrylate, which is incorporated into the gel network at the preparation. The total monomer concentration is fixed to be 700 mM [138]. . . . .	59
6.1	Some common monomer molecules. . . . .	63
6.2	Dissociation of sodium persulfate upon heating. . . . .	64
6.3	Dissociation of benzoyl peroxide upon heating. . . . .	64

6.4	Initiation step of polymerization. . . . .	64
6.5	Propagation step of polymerization where molecular weight of the polymer increases. . . . .	65
6.6	Termination step of polymerization where the reaction stops. . . . .	65
6.7	Diagram of emulsion polymerization system. . . . .	67
6.8	NIPA particles synthesizing setup. . . . .	69
6.9	2,2'-azobis(2-methylpropionamidine) (azobis) molecule. . . . .	70
6.10	2-aminoethylmethacrylate hydrochloride (AEMA) molecule. . . . .	70
6.11	Didodecyldimethylammonium bromide (DTAB) molecule. . . . .	71
6.12	Methylene-bis-acrylamide (BIS) molecule. . . . .	71
6.13	Dynamic light scattering setup. . . . .	75
6.14	The decay of the intensity autocorrelation function with time for NIPA particles at 20 °C. . . . .	76
6.15	Autocorrelation function as a function of time for NIPA particles at 20°C and 31.4°C. . . . .	77
6.16	Glass chamber containing NIPA particle suspension at high volume fraction. The color indicates that the suspension is in crystalline phase. . . .	78
6.17	Hydrodynamic diameter of NIPA particles as a function of temperature. NIPA particle radius undergoes first order transition at about 32.0°C. . .	78
7.1	(A) Simple microscope composes of two lenses, (B) infinity-corrected microscope where the objective forms the image at infinity. . . . .	84
7.2	Image beam path (left) and illumination beam path (right) in Köhler illumination design. . . . .	86
7.3	The interference of the direct light (from the light source) and the diffracted light (from the specimen) at the objective back focal plane and the intermediate image plane [102]. . . . .	87

7.4	Airy disks and associated intensity profiles of one and two particles. Microscope resolving power is not strong enough to differ between the two particles in (B) [102]. . . . .	88
7.5	(A) Raw bright field image of NIPA crystal. (B) The image after a spatial bandpass filter was applied. . . . .	90
8.1	Bragg diffraction (wavelength = 405 nm) of 0.75 $\mu\text{m}$ diameter NIPA particle colloidal crystal. . . . .	94
8.2	Bright field image of a layer in the NIPA particle colloidal crystal showing very few defects; the slice is of the 7th layer from the cover slip. Each bright spot corresponds to the central region of a 0.75 $\mu\text{m}$ diameter particle. . . . .	95
8.3	Bright field image of the NIPA particle colloidal crystal showing many defects (part of the image is in focus while the other part is out of focus); the slice is of the 15th layer from the cover slip. Due to sample preparation and annealing, the primary defects are partial dislocations that exist in the interior of the crystal. Scale bar is 5 $\mu\text{m}$ . . . . .	96
8.4	Time evolution of 2D particle mean square displacement (MSD); $L$ is derived from the MSD plateau value. . . . .	99
8.5	Measured microgel particle hydrodynamic radius as a function of temperature. . . . .	100
8.6	Lindemann parameter, $L$ , as a function of colloidal crystal temperature (and computed particle volume fraction $\phi$ ). This data are for regions far from defects. The curve exhibits a change in slope at 24.7 $^{\circ}\text{C}$ . The crystal melts at 28.3 $^{\circ}\text{C}$ , $\phi \sim 0.55$ . The error bars for $\phi$ , $L$ , and temperature are 0.02, .004, and 0.1 $^{\circ}\text{C}$ , respectively. . . . .	101
8.7	Pair correlation function of NIPA crystal at different temperatures. (A) first few peaks and (B) first peak shows that the lattice constant doesn't change as the temperature is increased up to premelting temperature. The base lines are displaced for clarity. . . . .	102

8.8	The lattice constant (obtained from the pair correlation function) in the solid regions of a NIPA crystal as a function of temperature. . . . .	103
8.9	The local Lindemann parameter, $L$ , as a function of distance from a vacancy, a partial dislocation, and a melt front. Within $1\mu\text{m}$ of the defects, the particle motion was too rapid and calculation of $L$ was unreliable. . .	104
8.10	Premelting of the colloidal crystal at a grain boundary. The figure shows bright field images at different temperatures (i.e particle volume fractions) of two crystallites separated by a grain boundary ( $\theta \sim 13^\circ$ ). (A) Sample at $27.2^\circ\text{C}$ . The solid and dashed lines show the grain boundary and a partial dislocation respectively. The grain boundary cuts the two crystals along two different planes (yellow line has two slopes). It is composed of an array of dislocations; the two extra planes are indicated by lines in the inset. (B) Sample at $28.0^\circ\text{C}$ . The grain boundary starts to premelt; nearby particles undergo liquid like diffusion, inset. The partial dislocation, denoted by the dashed line, is not affected. (C) and (D) The same sample at $28.1^\circ\text{C}$ and $28.2^\circ\text{C}$ , respectively. The width of the premelt region near the grain boundary increases. Scale bars are $5\mu\text{m}$ . . .	106
8.11	Bright field image of a layer in the NIPA particle colloidal crystal showing grain boundaries at $26.4^\circ\text{C}$ . Scale bar is $5\mu\text{m}$ . . . . .	107
8.12	Bright field image of the same layer of the NIPA particle colloidal crystal as in Fig. 8.11 showing grain boundaries at $28.2^\circ\text{C}$ . Scale bar is $5\mu\text{m}$ . . .	108
8.13	Bright field image of the same layer of the the NIPA particle colloidal crystal as in Fig. 8.11 and Fig. 8.12 showing grain boundaries at $28.3^\circ\text{C}$ . Scale bar is $5\mu\text{m}$ . . . . .	109

8.14	Melting of a colloidal crystal initiated at a Shockley partial dislocation in the absence of grain boundaries. (A) and (B) are bright field images of the 61st and 62nd layers at 25.0 °C, respectively. Colloidal particles fluctuate more in the 62nd layer due to the gap created by the dislocation. (C), Superposition of 61st (green) and 62nd (red and yellow) layers. The image shows particles in positions A (green), B (red), and C (yellow). Inset, 3D illustration of the 61st-64th layers (bottom to top) showing the displacement of the yellow spheres in the 62nd-64th layers. (D), 62nd layer at 28.2 °C where the crystal starts to premelt at the dislocation. Scale bars are 3 $\mu\text{m}$ . . . . .	111
9.1	Melting behavior of sample S1 (50 mg/ml <i>fd</i> and 7.5 mg/ml NIPA). (a) Lamellar phase at low temperature exhibits visible dislocation defects. (b) At 7 °C the dislocation defects act as a site for nucleation of the nematic phase. (c) Nematic domains grow, expelling NIPA polymer into lamellar phase, which leads to swelling of lamellar layers. (d) Swollen lamellar phase. (e) Coexistence between nematic phase and highly swollen lamellar phase. (f-g) Isolated monolayer-deformed isotropic tactoid. (h) Isotropic-nematic coexistence observed at high temperature. (i-l) Illustration of the proposed melting processes of the lamellar rod/polymer mixture. Scale bars are 5 $\mu\text{m}$ . . . . .	117
9.2	Melting of the lamellar sample S1 studied by small angle light scattering. The real space images of the melting behavior are shown in Fig. 9.1.(a) Small angle light scattering pattern of an orientationally disordered lamellar phase at 5°C (b) Angularly averaged intensity profile at 5 °C and 13 °C. (c) Lamellar periodicity for a sample during heating (filled circles) and cooling (open circles). There is a large hysteresis of layer spacing between heating and cooling cycles. . . . .	119



9.3	Melting behavior of sample S2 (7.5 mg/ml <i>fd</i> and 37 mg/ml NIPA). (a) At 24 °C lamellar droplets form in a background isotropic phase. Simultaneously, the formation of isolated layers (shown in image c) is observed. (b) At higher temperature, lamellar droplets melt into a nematic phase by the mechanism described in Fig. 9.1. (c) An isolated membrane is stable for a temperatures from 22-27 °C. (d-f) Sequence of images showing nucleation and growth of a 3D nematic tactoid from an isolated superheated 2D membrane. (g-j) Illustration showing the above described melting processes. At temperatures below 10 °C, the sample forms a miscible isotropic phase. The reason for this is not understood. Scale bars are 5 $\mu\text{m}$ . . . . .	121
9.4	Layer reducing transition of a colloidal membrane observed in sample S3 (12 mg/ml <i>fd</i> , 31 mg/ml NIPA). The sample temperature is 28 °C, below the melting of the bulk lamellar phase (29 °C). (a) A membrane is repeatedly punctured by a 2.1 $\mu\text{m}$ silica sphere trapped with laser tweezers. (b) A metastable nematic droplet forms due to shear melting. (c) Upon removal of the laser beam the nematic droplet freezes into a multi-layer smectic structure. (d-f) The structure undergoes a sequence of layer reducing transitions. (g-h) In a separate experiment a formation of a dislocation in the main membranes is visible. The dislocation subsequently disappears as layers slide over each other which reducing the number of layers by one. . . . .	123

# Chapter 1

## Introduction

This thesis is concerned with one of the most ubiquitous phase transitions in nature: melting. Although melting is one of the phase transitions most frequently seen in daily life, it presents a challenge to scientists. It is very difficult to construct a complete picture of melting of three-dimensional (3D) systems. One reason for this difficulty is that melting occurs in concentrated systems, involving the collective behavior of many-particle systems. Another reason is that melting is an abrupt transition, accompanied by a density jump. The densities of the solid and liquid phases are not universal, rather they depend on the kind of the material considered [135]. It is also very difficult to construct a microscopic theory for melting in 3D. Computer simulations are limited to small system sizes.

In our lab we use colloidal systems to experimentally study melting of one-dimensional (lamellar) liquid crystals and three-dimensional bulk crystals. There are minimal size limit in the colloidal systems and therefore collective behavior of colloidal crystals can be followed using simple optical microscopy techniques.

Colloidal science is a subfield of a rapidly expanding field of research called soft condensed matter [32]. Soft materials encompass a broad class of systems including rubber, plastic, paper, blood, polymers, membranes, biopolymers, emulsions, foams, soaps and detergents, suspensions, surfactants, liquid crystals, magnetic ferrofluids, colloidal

crystals, and many others.

These materials cannot always be simply classified as solids or liquids [48]. Although they have structures, they deform easily under the influence of external fields such as electric fields, shear, gravity, and even thermal forces. The relevant length scales that characterize these materials are typically much larger than the molecular scale, and the dynamics are much slower. Structure and dynamics at the mesoscopic i.e. nanometer to micrometer scales, thus determine the macroscopic physical properties.

A wide variety of day-to-day life and industrial applications for soft materials have been found, studied, and developed. Some examples of such materials are plastics, milk, paints, shaving creams, cosmetic creams, blood, disk drives, lubricants, display devices, medicines, and many others. As a result, soft matter has been studied by chemists, chemical engineers, and biologists. However, these systems exhibit generic characteristics that fascinate physicists, effects that can often be studied and understood independent of chemical details. For example polymer molecules in solution can be considered as a long string of balls continually wriggling (Brownian motion) [223]. Study of the generic properties of soft matter gives insight into fundamental questions that range broadly over many subjects in physics. Some examples include the nature of glasses and the melting and freezing transitions [180, 6, 5].

Colloidal particles come in various sizes, ranging from a few nanometers up to several microns, i.e. the mesoscopic scale. They can also have different shapes, for example spheres, rods, and discs. Their characteristic energies are often of the order of the thermal energy  $kT$ . Thus, their structures and dynamics are often rather strongly affected by thermal fluctuations. Colloids have a fascinating property as a result: they can “self assemble” into complex structures [223]. A suspension of micron-size spheres at high densities can self assemble into “colloidal crystals”. Suspensions of micron-size rods have even richer phase behaviors. They can align into what is called the “nematic phase”, or they can layer into what is called the “smectic phase”. Mixtures of different sized and

shaped colloids have even more complex phase behaviors. These suspensions are multi-component systems, consisting of mesoscopic particles, solvent molecules, salt ions, and possibly additional materials such as polymers.

Because of the possibilities to easily tune parameters such as temperature, ionic strength, pH value, and refractive index, the strength and the range of interaction between colloidal particles can be tuned. These effects offer unique ways to study the interparticle interactions and their role in effecting phase behavior, structure, and dynamics. The study of these systems thus stimulates theories of modern statistical mechanics, condensed matter, and non-equilibrium thermodynamics. Under certain conditions the effective colloid-colloid interactions can be made “hard”, i.e. the interaction is zero except at very short distances of approach, and then the interaction becomes very large: colloid-colloid overlap is not allowed. Colloidal hard-sphere, hard-rod, or hard-disc systems are athermal, i.e. the thermodynamic properties (e.g. phase behavior) are only determined by entropy. Despite this purely entropic nature, there are a rich variety of phase transitions that can arise from disordered to ordered phases.

The research tools in our lab consist mainly of conventional optical microscopy, confocal microscopy, light scattering, colloid synthesis, and image analysis. In this thesis we use these tools to study melting of nearly hard-sphere and hard-rod colloidal systems. These systems are athermal, the phase behaviors depend only on colloidal volume fraction. But it is difficult to change the volume fraction of rigid colloidal particles continuously in a single sample since the number of particles and their size are usually fixed. We overcome this difficulty by using temperature-sensitive microgel colloidal particles and polymers. The particles are mostly water, containing only a few percent polymer. On heating, the polymer becomes less soluble, expels water and then shrinks. A small increase in temperature in the range of room temperature causes the volume fraction of the suspension to decrease significantly. We then monitored the positions of the particles by video microscopy and measured the fluctuation of each particle at different volume fractions nearby and far from interfaces and crystal defects. Our measurements suggest

that interfaces and defects are playing a major role in determining the regions of initial melting.

In Chapter 2, we briefly review the equilibrium phase behavior of hard sphere suspensions. We also briefly review the main types of defects in three-dimensional crystal lattices. We show that due to stacking faults in an fcc colloidal crystal, the common defect is a Shockley partial dislocation. In Chapter 3, we review phase transitions in general and then we discuss different theories that describe the solid-liquid phase transition of crystal lattices. We review experimental, computer simulations, and theoretical evidence that suggest melting is a heterogeneous process starting at interfaces. In Chapters 4 & 5, we discuss the phase behavior of the semiflexible *fd*-virus and the temperature-sensitive NIPA polymer. In Chapter 6, we explain the free radical emulsion polymerization technique in general and show how NIPA particles were synthesized in our lab. We also explain the protocol for growing *fd*-virus in our lab. Chapter 7 explains the main techniques used in our study, they are the video microscopy and image analysis techniques.

In Chapter 8, we discuss our observations of melting at grain boundaries and dislocations within bulk colloidal crystals. The crystals are equilibrium close-packed, three-dimensional colloidal structures made from thermally responsive microgel spheres. We show the advantage of using video-microscopy and particle tracking routines in colloidal systems. Our particle tracking reveals increased disorder in crystalline regions bordering defects, the amount of which depends on the type of defect, distance from the defect, and particle volume fraction.

In Chapter 9, we discuss the phase behavior of a novel suspension composed of rod-like *fd* virus and thermosensitive polymer poly(N-isopropylacrylamide). The suspension phase behavior is temperature and concentration dependent. The system exhibits a rich variety of stable and metastable phases, and provides a unique opportunity to directly observe melting of lamellar phases and single lamellae. We found that lamellar phases swell with increasing temperature before melting into the nematic phase. The highly swollen lamellae can be superheated as a result of topological nucleation barriers that

slow the formation of the nematic phase.

Finally, Chapter 10 summarizes our results using thermal sensitive polymer to study melting of one-dimensional liquid crystals and three-dimensional colloidal crystals. We also briefly describe future work. Our system has potential to give insights into other fundamental questions in physics, such as two-dimensional melting, freezing, and the glass transition.

## Chapter 2

# Colloidal Crystal and Crystal Defects

### 2.1 Equilibrium Phase Behavior of Hard Sphere Suspensions

Colloidal suspensions of monodisperse spheres in the micron size range are important model systems for investigation of a variety of problems of interest in condensed matter physics and physical chemistry. The suspensions hold potential to provide answers to fundamental questions about phase transitions such as the glass transition, melting and crystallization and the role of entropy in these processes. A key experimental feature associated with these thermodynamic systems is our ability to track trajectories of all particles in space and time.

Hard-sphere systems are arguably the simplest thermodynamic systems. They can be considered as first approximation to many “less” ideal systems. The hard-sphere interaction is purely repulsive. The inter-particle interaction potential is zero except when particles are in contact; then the potential goes to infinity. Experimentally, many systems display hard sphere like behavior, for example particles made from polymethylmethacrylate (PMMA) and sterically stabilized with grafted poly-12-hydroxystearic acid in decalin. Charge stabilized polystyrene, PMMA, and silica particles are also examples of

systems that display hard sphere like behavior. In these systems, counter-ions in solution screen the long range Coulomb repulsion between particles, and the inter-particle interaction potential become large when particles closely approach one another. Experiments, statistical mechanical theories, and computer simulations have all been used to investigate the equilibrium phase behavior of the hard-sphere system [224, 4, 3, 181, 88]. As shown in Fig. 2.1, below a volume fraction of 0.49 the system is in a liquid state. Between the volume fractions 0.49 and 0.545 there is liquid-solid coexistence. Between the volume fractions 0.545 and 0.74 the system is in a solid (crystalline) phase. Because the next nearest neighbor interaction is almost zero, the energy difference between face centered cubic (fcc) and hexagonal close packed (hcp) lattices is very small. Thus the solid phase is often a mixture of (fcc) and (hcp). The system can also be trapped in a local minima glassy phases for volume fractions between 0.58 and 0.63. In that range of volume fraction the viscosity of the suspension is high, and particles cannot arrange themselves to find their minimum energy configuration on a realistic timescale.

The phase behavior of hard sphere suspensions is driven entirely by the entropy. The behavior is temperature independent. Above a volume fraction of 0.49, particles prefer to crystallize into a lattice in order to have more space per particle to fluctuate; disordered arrangements of particles that arise in glasses and random close-packed structures have less volume per particle on average. Excluded volume is the volume inaccessible to the center of one particle due to the presence of others. When the particle concentration is sufficiently high, the particles organize themselves in a way to increase the excluded volume and thus maximize their entropy. Entropy in hard sphere systems depends explicitly on the free volume per particle.

Colloids are the only experimental systems that approximate the behavior of hard particles closely enough so that all of the ordering transitions described above occur. This is due to the fact that at the colloidal length scale it is possible to engineer the interaction potential between particles using various chemical or physical modification schemes, while on the molecular scale it is impossible to avoid the long range attractions, e.g. of van



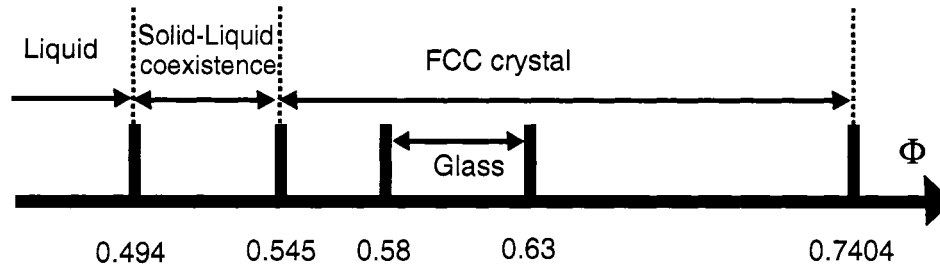


Figure 2.1: Phase behavior of monodisperse hard colloidal spheres.

der Waals origin. Today the synthesis of highly monodisperse spherical colloids made of insoluble polymers whose interaction closely approximates hard sphere potential is fairly routine. Experiments on these systems have provided the first experimental confirmation that the assembly of hard spheres undergoes a liquid to crystal transition [181].

## 2.2 Crystal Defects

Crystal defects are the imperfections of the ideal arrangement of atoms in a crystal. A perfect crystal with regular arrangement of atoms cannot exist at finite temperature. There are always defects in crystal lattices due to impurities and thermally activated defects. Defects determine many properties of materials and play important roles in material science. The presence of a relatively small number of defects can have a profound impact on some macroscopic properties of materials, and the intentional introduction of defects is important in many kinds of material processing. For example, the resistivity in semiconductors, conductivity in ionic crystals (or transport in general), and the mechanical strength of materials are heavily affected by defects. In the electronics industry, production of advanced semiconductor devices require involved introduction of specific defects into the sample. Also manipulation and introduction of crystal defects are used to increase the strength of forging metal tools. Other properties like elasticity, density, and heat capacity, on the other hand, are not affected so obviously by defects in reasonably good crystals.

Although many material behaviors, like plastic deformation, can be explained by crystal defects, the subject is rather complicated. A point defect, for example, is the simplest type of defect, but it can be pretty complex in a real crystal. For example, what are the natures of vacancies and interstitials in real crystals? Is it just removing or adding one atom or does it involve the neighboring atoms? If it involves the neighboring atoms, what are their configurations? In the cases of vacancy and interstitial in an ionic crystal, is there a charge imbalance? The three basic classes of defects in crystals are point, linear, and planar defects.

## 2.3 Point Defects

Among the most common defects in crystals are point defects. In the case of pure materials, the common types of point defects are lattice vacancies and self-interstitials. When the material has impurities, substitutional and interstitial impurities are the common types of point defects, see Fig. 2.2. Vacancies occur when atoms are missing from the lattice. Their number densities are larger at high temperatures, when atoms frequently and randomly change their positions sometimes leaving behind empty lattice sites. In most cases atomic diffusion occurs largely because of vacancies. The higher the temperature, the more often atoms jump from one equilibrium position to another and the larger the number of vacancies in the crystal. In fact the number of vacancies increases exponentially with the absolute temperature, and can be estimated using Boltzmann distribution.

Self-interstitials occur when atoms of the same species as the lattice are in irregular places. In this case the interstitial atoms are squeezed in between regular lattice sites. Creation of a self-interstitial causes a substantial distortion in the surrounding lattice and costs more energy compared to the energy cost for the creation of a vacancy. Under equilibrium conditions, self-interstitials are present in lower concentrations than vacancies. Foreign atoms (usually smaller ones like carbon, nitrogen, hydrogen, oxygen) are called

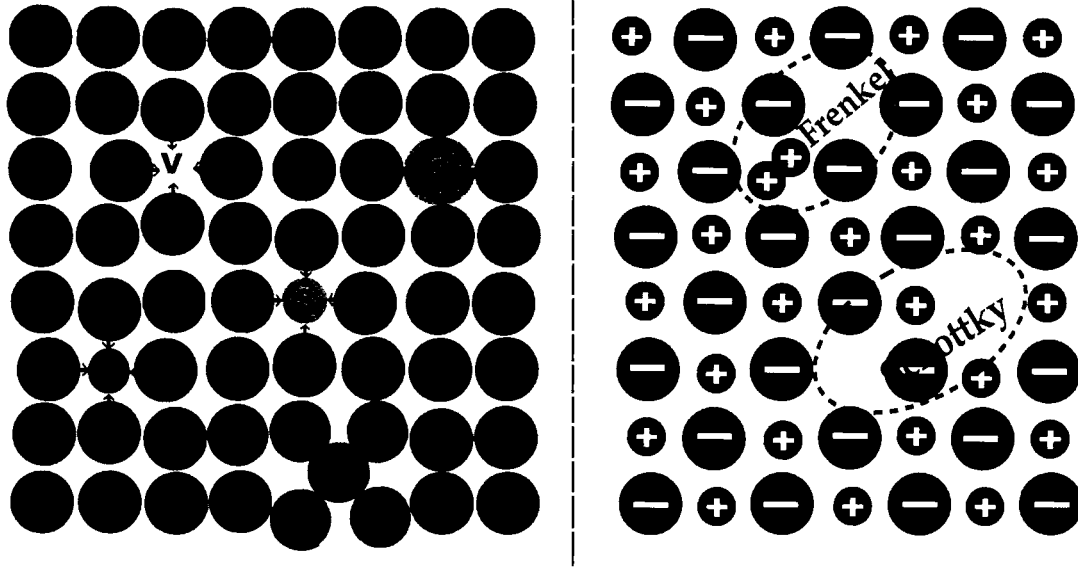


Figure 2.2: Some common point defects in crystal lattice.  $V$  is a vacancy.  $II$  is a interstitial impurity.  $SI$  is a self-interstitial.  $S$  is a substitutional. If the substitutional atom is bigger (smaller) than the original lattice atom, the created stress goes outward (inward). Frenkel and Schottky defects occur in ionic crystals.

interstitial impurities. They introduce less distortion into the lattice and are more common in real materials and are more mobile. If a foreign atom replaces or substitutes for one in the crystal, it is called a substitutional impurity.

In ionic crystals, like sodium chloride crystal, the bonding is provided by Coulomb forces between positively and negatively charged ions. Point defects in ionic crystals are also charged. The Coulomb forces are very large and any charge imbalance has a very strong tendency to balance itself. To maintain charge neutrality several point defects can be created. A Frenkel defect consists of a cation vacancy and anion interstitial. Or it may also be an anion vacancy and cation interstitial. A Schottky defect consists of anion and cation vacancies, see Fig. 2.2. In both Frenkel and Schottky defects, the pair of point defects stay near each other because of the strong Coulomb attraction of their opposite charges.

All point defects introduce local distortions into the lattice, and as a result of these distortions they interact with each other and feel external stresses. The external stresses

or stresses from larger defects can induce a directionality to the “random” jumps of atoms. For example, a pressure gradient results in a flux of vacancies in the direction towards a compressed region of the sample.

### 2.3.1 Linear Defects

Common linear defects are screw (Fig. 2.4) and edge dislocations (Fig. 2.3). Dislocations can be explained as extra lattice planes inserted in between two existing crystal layers. The extra planes are not extended through all of the crystal, rather they end in the dislocation line. Interatomic bonds in the vicinity of the dislocation line are significantly distorted; this area is called the dislocation core. There are small elastic deformations of the lattice at large distances from the dislocation core. Before the discovery of dislocations it was estimated that metals undergo plastic deformation at forces much smaller than the theoretical strength of the forces that hold the metal atoms together. Dislocations explain the plastic deformation of crystals. Motion or propagation of dislocations allows crystal layers to slip. During the propagation of dislocations, a few interatomic bonds break and reform. This requires a small force compared to that which causes the bonds break and reform.

One application of this phenomenon is that metals can be strengthened by making it more difficult to move dislocations. Obstacles can be introduced to stop dislocation motion, e.g. interstitial impurities (carbon atoms added to steel for example). Trial and error has lead to an astonishing degree of steel elasticity and strength, as a result of these ideas. The key is the manipulation of defects.

The size and the direction of a dislocation can be measured using Burgers vector  $\vec{b}$  see Fig. 2.4 and Fig. 2.3. To find the Burgers vector, a circuit is drawn from atom to atom counting the same number of atomic distances in all directions. If the circuit encloses a dislocation it will not close. The vector that closes the loop is the Burgers vector  $\vec{b}$ . If Burgers vector is directed perpendicular (parallel) to the dislocation line, then the line

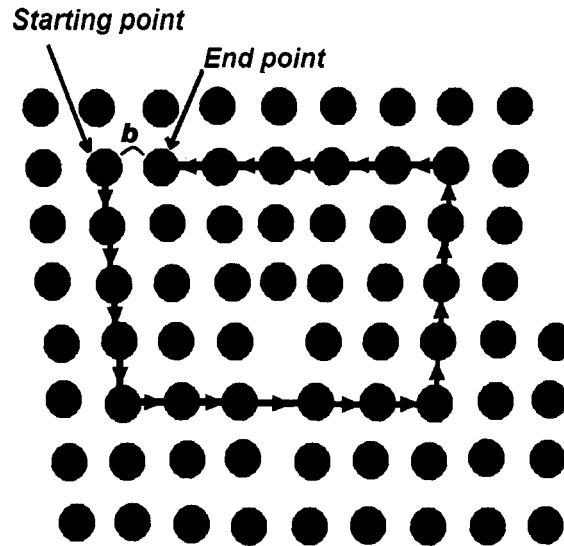


Figure 2.3: An edge dislocation. Burger vector  $b$  is parallel to Burger circuit.

defect is called an edge dislocation (screw dislocation).

## 2.3.2 Planar Defects

Common planar defects are grain boundaries, partial dislocations and free surfaces. Free surfaces are defects that cannot be eliminated from most of the crystals. The number of nearest neighbors is different from the bulk and the atomic bonds are distorted. In general, the physical properties of crystal surfaces are different from the bulk.

### 2.3.2.1 Grain Boundaries

Single crystals can rarely be found among real materials. Instead, solids generally consist of a number of small crystallites or grains where the orientations of atomic planes are rotated with respect to the neighboring grains. The individual grains are separated by grain boundaries. These regions are less densely and less regularly packed compared to the bulk material inside the grains. There are small-angle and large-angle grain boundaries. Small angle grain boundaries can be described as an array of dislocations, Fig. 2.5.

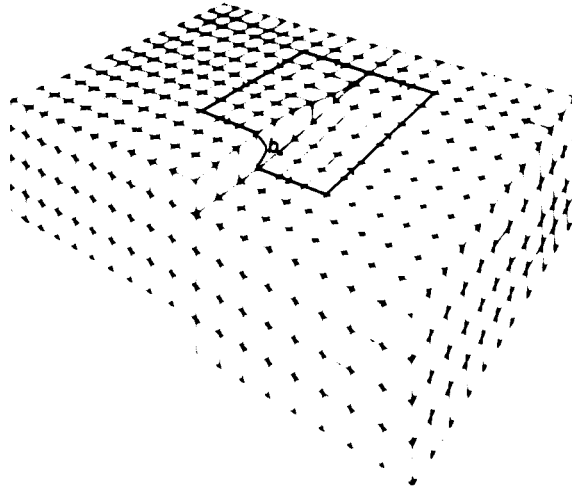


Figure 2.4: A screw dislocation. Burger vector  $b$  is normal to Burger circuit.

In general, the increase in the misfit angle produces an increase in the interfacial energy. Real grain boundaries are even more complicated, e.g. they might not be flat, they may contain foreign atoms or they may contain thin amorphous layers.

### 2.3.2.2 Shockley Partial Dislocation in fcc Crystals

First let's briefly review stacking order in the close-packed structures. To pack spheres in layers, there are three positions for sphere centers, as seen in Fig. 2.6, A, B, and C. In order to achieve a close-packed structure, each layer has to stack in a position such that the spheres of two successive layers cannot be in the same lateral position. For example stacking in a sequence ABACABC is a close-packed structure, while AABB is not. The normal sequence of face-centered-cubic (fcc) is ABCABCABC. The normal sequence of hexagonal-close-packed (hcp) is ABABABAB.

A deviation from the normal stacking sequence of fcc crystal is called a stacking fault. For example ABCACABC has a stacking fault in the fifth layer. If a fault ends inside the crystal, its boundary is a partial dislocation. In other words if, for example, part of a layer is in B position (normal sequence) and another part is in C position (stacking fault) then the boundary between them is a partial dislocation, see Fig. 2.7. If the two regions stack

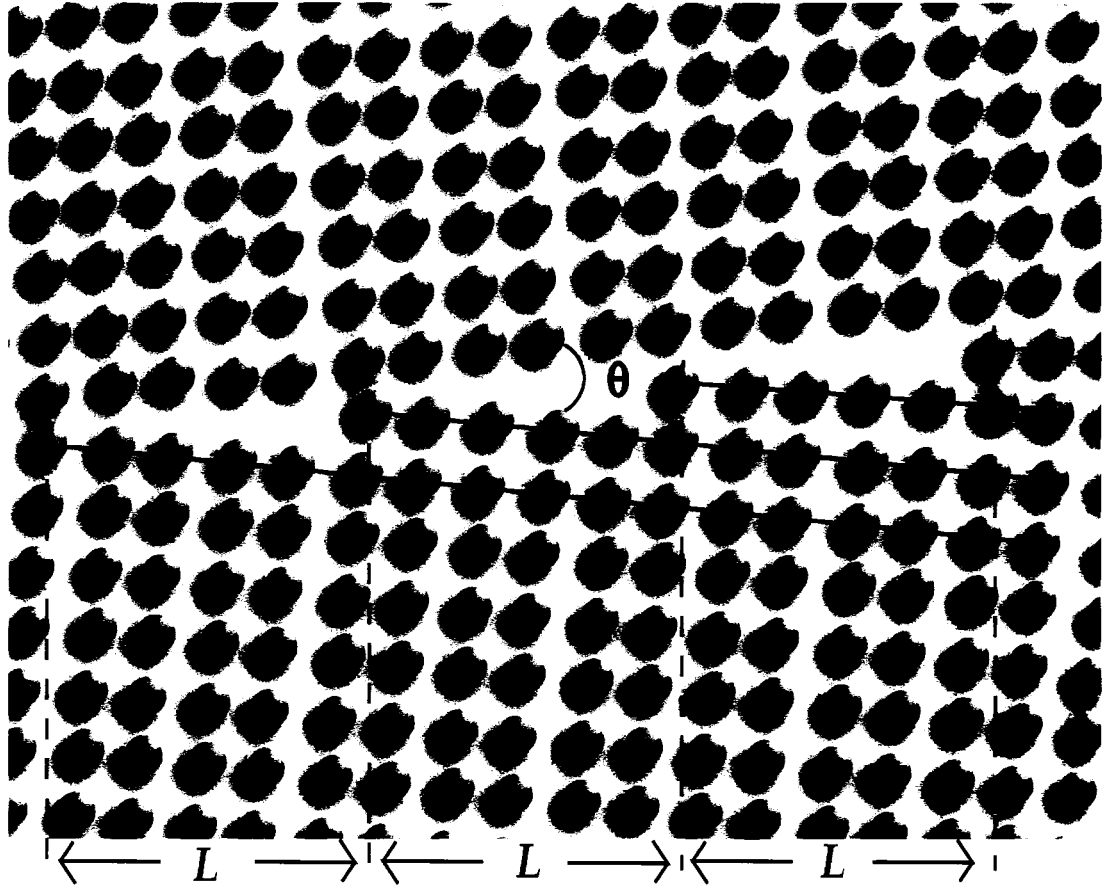


Figure 2.5: Small angle grain boundary illustrated as an array of dislocations. Simple geometry can show that the angle between the two grains can be calculated from;  $\theta \simeq \frac{d}{L}$ , where  $d$  is the lattice constant and  $L$  is the dislocation separation.

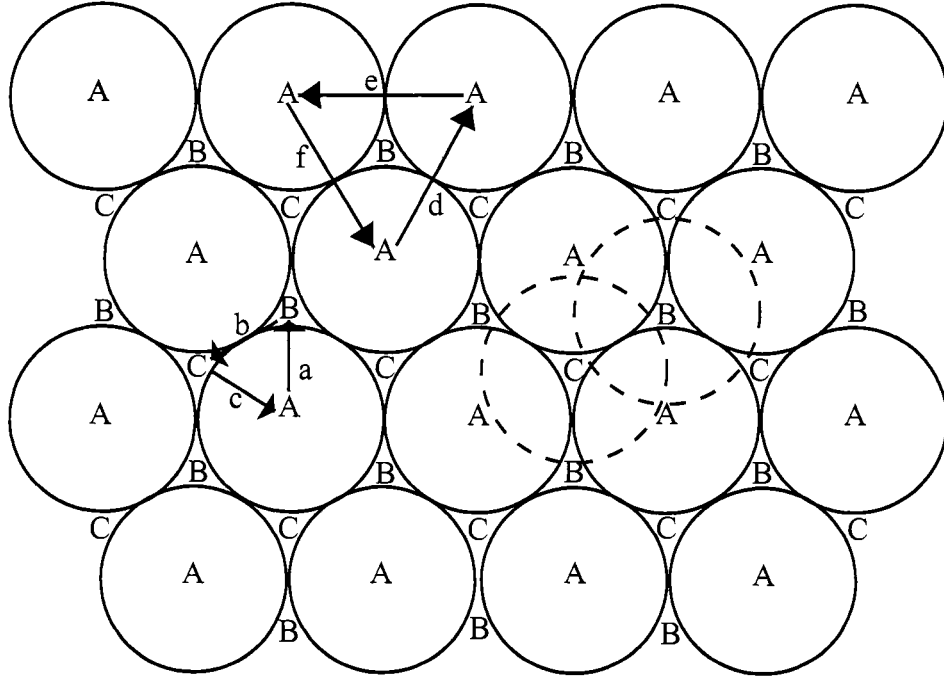


Figure 2.6: Stacking spheres in close-packed structure. The first layer is in position A, the second layer either take position B or C, both positions cannot be occupied in the same time. The vectors a, b, and c connect positions A, B, and C as shown in the figure. The vectors a, b, and c are  $\frac{1}{6}[\bar{2}11]$ ,  $\frac{1}{6}[1\bar{2}1]$ , and  $\frac{1}{6}[11\bar{2}]$  respectively. The vectors d, e, and f connect the nearest A positions. The vectors d, e, and f are  $\frac{1}{2}[\bar{1}10]$ ,  $\frac{1}{2}[10\bar{1}]$ , and  $\frac{1}{2}[0\bar{1}1]$  respectively.



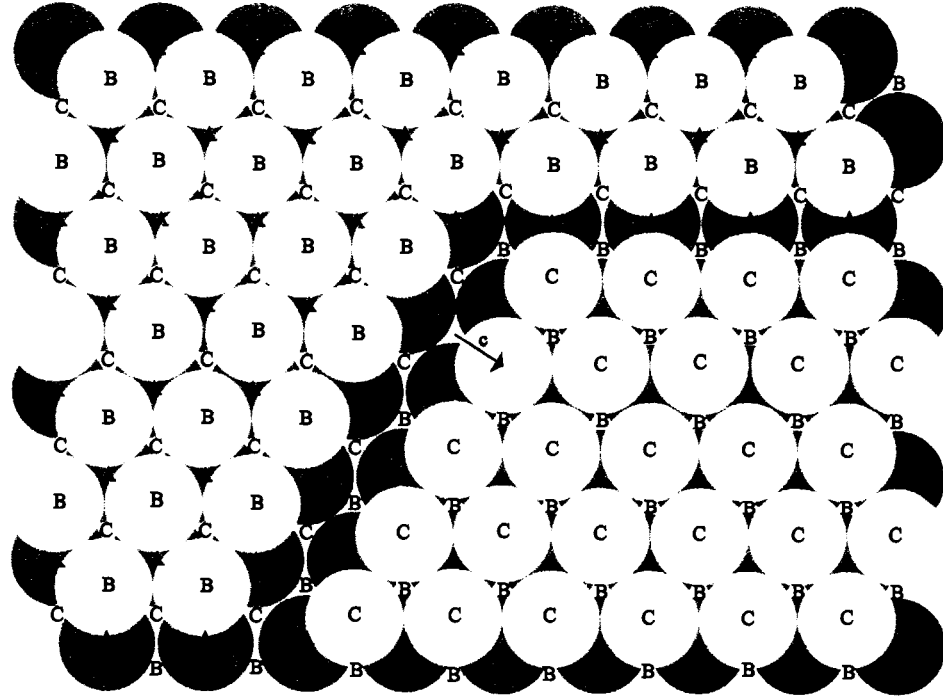


Figure 2.7: Stacking fault in a face-centered-cubic structure. The second layer in the right-lower part stacked in the C position instead of the B position. The fault ended inside the crystal and the faulted region (lower-right) displaced by  $\frac{1}{6}[11\bar{2}]$ . The boundary between the faulted region and the normal region (left) is a Shockley partial dislocation. If the two region stack normally after the second layer, the partial dislocation will be two gaps cut the crystal along (100) plane and have  $120^\circ$  with respect one to the other.

normally after the faulted layer, the partial dislocation will be gaps cut the crystal along (100) plane. The difference between a partial dislocation and edge or screw dislocations is that in edge or screw dislocations the Burger vector is one of the lattice vectors, while in a partial dislocation it is not. The definition of the lattice vector is that the vector connects two atoms in the perfect crystal.

# Chapter 3

## Melting & Phase transitions (Solid-Liquid)

### 3.1 Phase Transitions

Phase transitions are considered by many to be amongst the richest and most interesting of physical phenomena. Although many phase transitions are seen frequently in daily life, they present a challenge to statistical mechanics. At the transition point the system exhibits a singular behavior in its thermodynamic parameters such as pressure, volume or magnetization (in the case of ferromagnet). For any equilibrium system, the fundamental quantity in statistical mechanics is the partition function, which is the sum of Boltzmann factors over all possible states of a canonical system of  $N$  atoms occupying volume  $V$  at temperature  $T$ . All thermodynamic properties are embodied in the partition function which is an analytical function. Since all details of any phase transition are in the partition function, this means the partition function must have singularity. Lee and Yang proposed a definite scenario where, in the thermodynamic limit of  $V$  and  $N$ , the density  $\phi = N/V$  is finite, and the partition function can have a singularity [124, 230]. In principle the partition function can be calculated from the system Hamiltonian, so that in principle,

phase transitions should be predictable if the Hamiltonian is known. In general however, this approach is difficult. However, it has been found that in the vicinity of the phase transition many of the system properties are universal regardless of the microscopic details. For example, quantities such as heat capacity can exhibit universal singular behavior at the critical point. Close to the critical temperature,  $T_c$ , the relation between heat capacity and the reduced temperature,  $t = (T - T_c)/T_c$ , shows a power law dependence with a universal exponent  $-a$ , called the critical exponent. Similarly, the order parameter, susceptibility, equation of state, and the spatial correlation functions of the order parameter, all exhibit universal critical exponent behavior with exponents  $b, g, d, n$ , and  $h$  respectively. Not only that, it turns out that there exist relations between the critical exponents. Of the six exponents only two are independent.

Lets discuss the order of the phase transition first. Fig 3.1 shows the Gibbs free energy as a function of  $1/T$  for two phases  $A$  and  $B$ , say liquid and solid phases. At each temperature the free energy is minimum if one of the two phases exists, which means, one phase is stable at the particular temperature. The free energy however is equal for both phases at one temperature, this is the transition temperature. Both phases coexist at that point. The system then will change from phase  $A$  to phase  $B$  as the temperature decreases. The free energy has a kink at the transition point, or in other words the slope of the curve is discontinuous at that point. If the the first derivative of the free energy with respect to temperature,  $\partial G/\partial T$ , is discontinuous, the transition is called first order transition. In general if the discontinuity is in the  $n^{th}$  order, the transition is called a  $n^{th}$  order transition. Historically, the order of the phase transition was first characterized by Paul Ehrenfest. The illustrated free energy in Fig. 3.1 is a first order transition, since  $\partial G/\partial T$  is discontinuous at the transition point. If the free energy curve has a hump instead of a kink, the second derivative would be discontinuous instead and the transition is second order. The discontinuity of  $\partial G/\partial T$  is just the change in the entropy between the two phases. Thus at a first order transition the entropy changes discontinuously, while at second order transition the entropy changes continuously. The latent heat is given

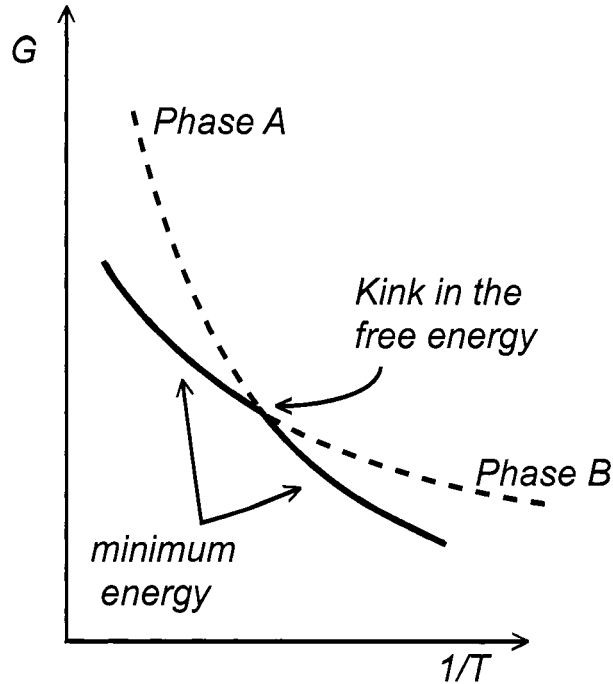


Figure 3.1: Gibbs free energy as a function of  $1/T$  for two phases  $A$  and  $B$

by  $T\Delta S$ . Latent heat is associated with a first order transition, but not with higher order transitions. Also since the entropy is a measure of disorder, we expect the order parameter, see Fig. 3.3 and Fig. 3.4, will be discontinuous at the transition point for the first order transition and continuous for higher order transitions.

Landau was the first to formulate the modern theory of phase transitions. He found that some quantity goes to zero at the critical point, which he named the “order parameter”. Upon heating a fluid, the density goes to zero. Upon heating a ferromagnet, the magnetization goes to zero. In many cases the system becomes more or less ordered at the transition point. In other words, as the temperature is lowered to the transition point, some symmetry gets broken. For example, the liquid-crystal phase transition involves translational symmetry breaking, and paramagnetic-ferromagnetic phase change involves rotational symmetry breaking.

A special example of a phase transition is a critical point. Close to the critical point, there are large fluctuations in the order parameter of the system that become macroscopic

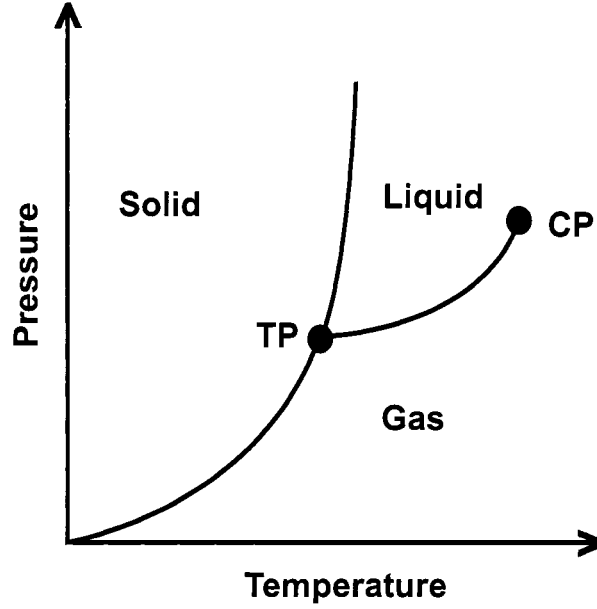


Figure 3.2: P-T phase diagram of gas-liquid-solid phases of a pure material.

regardless of the microscopic interactions. Consider, for example, the liquid-gas transition. On heating the liquid along the liquid-gas line, as shown in Fig. 3.2, the system reaches a critical point (CP). At the critical point the distinction between liquid and gas disappears, gas turns into liquid and visa/versa. Thus, there is no surface tension associated with the coexistence of gas and liquid, and liquid and gas densities become very close. The opalescence observed in fluids close to the critical point is a consequence of density fluctuations that become large enough to be observed macroscopically. Here, another important parameter is the correlation length, which is a characteristic length of regions with approximately the same order parameter [32]. The correlation length varies with reduced temperature as a power law whose critical exponent is  $-n$ . The fundamental assumption of Landau theory is that the free energy may be expanded in powers of the order parameter close to the transition point. The spatial fluctuations of the order parameter are neglected in Landau theory.

As mentioned before, if the order parameter decreases “gradually” as the temperature approaches the transition point, then the transition is called a second order transition (see

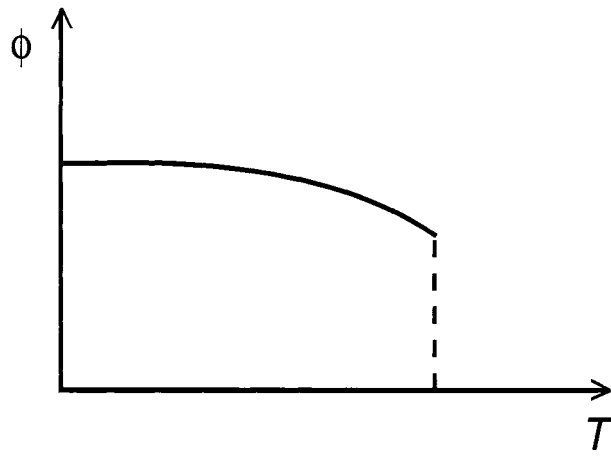


Figure 3.3: Order parameter as a function of temperature in a first-order phase transition.

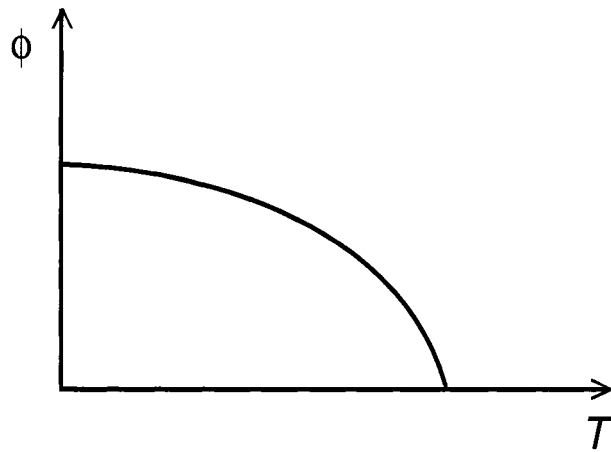


Figure 3.4: Order parameter as a function of temperature in a second-order phase transition.

Fig. 3.4). But if the order parameter changes abruptly in the vicinity of the critical point, it is called first order transition, see Fig. 3.3. In Landau theory, the free energy is expanded at least to the fourth power of the order parameter in the second order phase transition. Higher terms are neglected since the order parameter is very small in the vicinity of the transition point. On the other hand, the free energy for the first order phase transition has to be expanded at least to the sixth power of the order parameter. In the absence of an external potential, the system has a center of symmetry that requires the odd terms vanish. The free energy can then be written as

$$F = F_2\phi^2 + F_4\phi^4 + F_6\phi^6 + \dots, \quad (3.1)$$

where  $\phi$  is the order parameter. The sign of  $F_4$  determines if the transition is first or second order. If  $F_4$  is positive, the transition is second order, while if it is negative, the transition is first order. The free energy plotted as a function of order parameter for first and second order phase transitions is illustrated in figures 3.6 and 3.5 for temperatures below, equal, and above the transition temperature.

For the first order phase transition, the order parameter changes abruptly (see Fig. 3.3). The series expansion requires the jump in the order parameter be small in order to neglect terms higher than sixth power. This means the Landau theory is valid only in “weak” first order transitions. Landau theory is a phenomenological approach that deals only with macroscopic quantities and avoids dealing with microscopic structure. It is also only valid close to the transition point. In the Landau approach critical exponents can be calculated. Although they are not precisely consistent with the experiments, they are not too far off.

A significant improvement over the Landau approach is the “renormalization group” approach. As mentioned before, the spatial fluctuations of the order parameter are neglected in Landau theory. But at critical point, for example, spatial fluctuations cannot be ignored. The strategy of renormalization group is to tackle the problem in steps, one step for each length scale. The idea is to carry out statistical average over thermal fluctuations

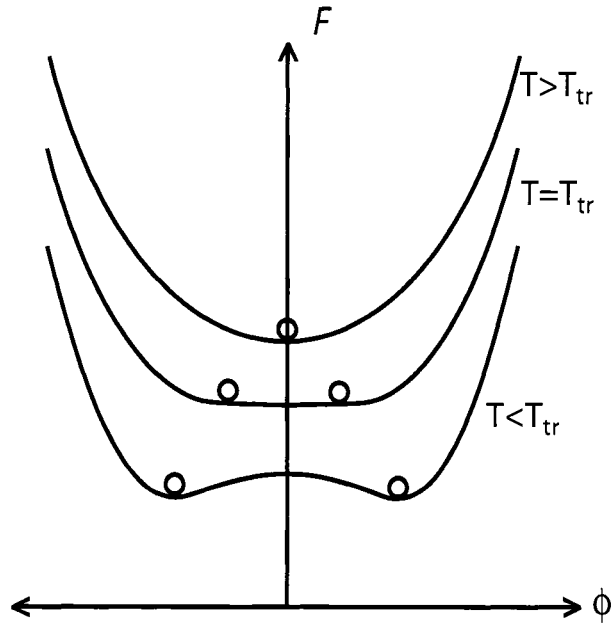


Figure 3.5: The free energy as a function of order parameter for a second-order phase transition for temperatures less than, equal to, and greater than the phase transition temperature.

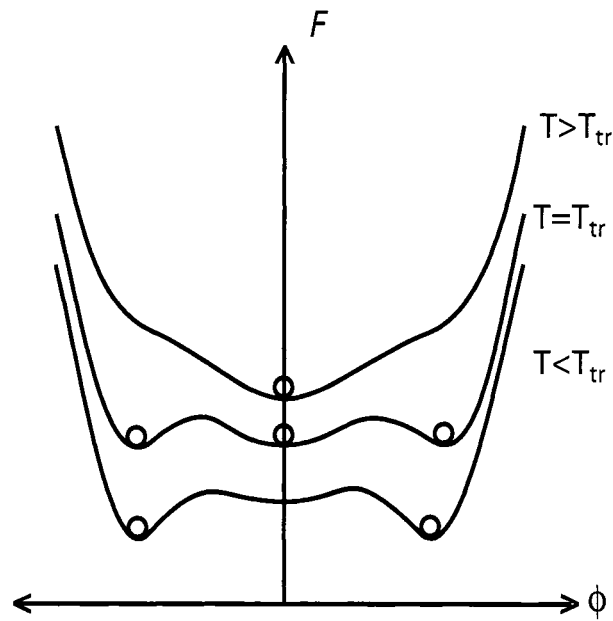


Figure 3.6: The free energy as a function of order parameter for a first-order phase transition for temperatures less than, equal to, and greater than the phase transition temperature.



on all size scales. The renormalization group approach integrates out the fluctuations in sequence starting with fluctuations on an atomic scale and then moving to successively larger scales until fluctuations on all scales have been averaged out. It has been a remarkably successful theory for understanding phase transitions [220].

## **3.2 Melting and Premelting of Crystal**

Melting is one of the phase transitions most frequently encountered in daily life and it is one of the most fundamental phenomena in physics. Although melting and freezing occur at the same temperature, their kinetic pathways are not the same. In general, a solid can hardly be superheated, while a liquid can be undercooled by many degrees. Both phenomena (melting & freezing) are first order phase transitions (abrupt transitions), which makes it difficult to understand these phenomena at the macroscopic level starting from microscopic models. Nevertheless, detailed knowledge about melting and freezing has accumulated for more than 100 years and many microscopic details are now known. A universal concrete and accurate model for melting, however, does not exist. In this section I will review some important theories and criterions associated with melting.

### **3.2.1 Lindemann Criterion of Melting**

There are gaps between theories and experimental results in the exploration of first-order phase transitions. These gaps are partially filled by phenomenological theories or models. One of the first phenomenological theories providing a melting model was proposed by Frederick Lindemann in 1910 [49, 50]. His theory doesn't consider the mechanisms that lead to melting. It is also a one phase theory, i.e. it only treats the solid and says nothing about the liquid. The basic idea of Lindemann theory is that a crystal lattice melts when the oscillations of the atoms become so large that the atoms start to invade

the spaces of the nearest neighbor. It states that solids start to melt when the root-mean-square amplitude  $\sqrt{\langle \Delta r \rangle^2}$  of the thermal vibration reaches a critical fraction,  $\delta$  of the nearest-neighbor separation,  $a$ , i.e.  $\sqrt{\langle \Delta r \rangle^2} = \delta a$ . Although it is difficult to verify this formula because of a lack of knowledge about the anharmonic factors affecting the vibrational amplitudes at high temperature, calculations based on it might be valid for crystals with similar structure. In 1907 Einstein, in his explanation of the specific heat capacity at low temperature, proposed that the atoms vibrate as quantized harmonic oscillators. Lindemann made use of Einstein's proposal. In a harmonic approximation, one can directly write the probability distribution of the atomic displacement vector,  $\Delta r$ , relative to its lattice site as:

$$f(\Delta r) = (M\omega^2/2\pi k_B T)^{3/2} \exp[-(M\omega^2/2k_B T)(\Delta r)^2], \quad (3.2)$$

where  $f$  is the probability density of finding the atom at a distance  $\Delta r$  from its equilibrium position,  $M$  is the mass of the atom,  $\omega$  is the frequency of the oscillation,  $T$  is the absolute temperature, and  $k_B$  is the Boltzmann constant. The dispersion relation of  $\Delta r$ ,  $\langle (\Delta r(\omega))^2 \rangle$ , can be calculated using the above relation. To average over all frequencies one can use Debye frequency distribution function  $D(\omega) = 3\omega^2/\omega_D^3$ , where  $\omega_D$  is the Debye frequency, and the Debye temperature  $\Theta$  is defined by the relation  $\hbar\omega_D = k_B\Theta$ . The final form of the mean-square deviation of the atoms from their equilibrium position due to thermal vibration is:

$$\langle (\Delta r)^2 \rangle = 9\hbar^2 T / M k_B \Theta^2, \quad (3.3)$$

using Eq.3.3 the Lindemann parameter (squared) will be

$$\delta^2 = 9\hbar^2 T_m / M k_B \Theta^2 a^2, \quad (3.4)$$

where  $T_m$  is the melting temperature.

Despite the success of Lindemann theory (for many simple solids, melting starts when  $\delta$  reaches 1/8), the calculation above has serious problems. It is based on the harmonic

force between atoms, while melting must necessarily involve bond breaking. The model also treats melting from the solid phase only, while the transition must involve solid and liquid phases. Finally the theory describes melting from the point of view of individual atom behavior, while melting develops in a cooperative way.

### 3.2.2 Dislocation mediated Melting

In this theory, melting occurs when dislocations accumulate and unbind close to the melting temperature. At the transition temperature a dislocation catastrophe arises wherein the solid becomes saturated with a large number of defects. The melting point is the point at which the free energy of the dislocation cores becomes negative. At that temperature the solid becomes unstable against a state wherein large numbers of faults are generated in the crystal. During this process, the solid absorbs a significant amount of latent heat and the crystal loses its resistance to shear forces. In this scheme the liquid is described as essentially a highly faulted solid.

Dislocation-mediated-melting theory was first suggested by Mott [141] and Shockley [26], who described melting by the numerical increase of and the entanglement of dislocation loops inside the solid. The region close to the dislocation core is severely strained and because of this strain, the core can become a center of dilation. The strain contributes to the elastic energy and the dilation contributes to the entropy of the dislocation. The core energy and the entropy can be related to the dislocation's Burger vector. The energy per unit length of the dislocation core can be written as [119],

$$U_c = \frac{Gb^3\alpha}{4\pi}, \quad (3.5)$$

where  $G$  is the elastic modulus (which can be anisotropic in a crystal),  $b$  is the Burger vector, and  $\alpha$  is a constant that depends on the type of crystal. The entropy per unit length of the dislocation core can be written in the form [119],

$$S_c = \frac{3gkX}{b}, \quad (3.6)$$

where  $g$  is a constant named the Grüneisen constant,  $k$  is the Boltzmann constant,  $X$  is the ratio of the available volume per unit length of an atom in the dislocation core to the available volume in the perfect crystal.

Dislocations are easily thermally activated when its free energy  $F_c = U_c - T_m S_c$  vanishes. According to the theory, the dislocation free energy vanishes at the melting temperature  $T_m$ . One can then write the melting temperature as:

$$T_m = \frac{U_c}{S_c} = \frac{Gb^3\alpha}{12\pi gkX}. \quad (3.7)$$

The result is that solids absorb a substantial amount of latent heat which generates bound pairs of dislocations (dislocation dipoles). Dislocation dipoles screen each other's strain field, then lose their resistance against shear stress, and then unbind. Melting in this theory is considered to be a first order transition. The assumption that the core energy is accounted for by equation 3.5 is only true when the number of dislocations is large enough so that they screen one another's strain. Kuhlmann-Wilsdorf, [119], related this picture of melting to the Lindemann criterion of melting since both depend on the elastic modulus of the solid. Mizushima [139] and Oakawa [151] also accounted for the decrease of the dislocation core energy with increase in dislocation density. In their theory, melting is also a first order phase transition. Many dislocation theories followed subsequently [66, 26, 86].

There are many critiques of melting-mediated-dislocation theories. The calculations are not easy, and substantial approximations have to be made. The energy cost of the elastic deformation due to a dislocations depends on dislocation orientation since the elastic modulus is anisotropic. The available space for an atom in the dislocation core depends also on dislocation orientation. But dislocations are activated randomly which makes the values of  $G$  and  $X$  in equation 3.7 accurate only to within 30% [119]. That wouldn't distinguish between melting, premelting or superheating. The theory also does not explain the fact that liquid can be undercooled while solids cannot, in general, be superheated. The dislocation-mediated melting theory also is not supported by experimental evidence.

Many experiments suggest that melting starts on surfaces [47, 77]. Despite these critiques, the theory might be applicable to the case of superheating of crystals, where surfaces play no role. It has been established experimentally that superheating of crystals is possible if the effects of surfaces are minimized, for example if the crystal surfaces were coated with other crystalline material that has the same lattice constant and higher melting point, e.g. silver coated with gold [46].

### 3.2.3 Melting of 2D systems

A famous theory describing melting in 2D is KTHNY predicted by Kosterlitz, Thouless, Halperin, Nelson, and Young [116, 146, 232]. They used the same concept of dislocation-mediated melting presented before in three-dimensional crystals. Dislocation topology is much easier in two-dimensional than three-dimensional crystals and thus the theory is easier to construct. In three-dimensional crystals, a dislocation is an extra lattice plane squeezed in between two existing crystal layers. This plane is terminated inside the crystal in a line which is highly strained (dislocation core). In two-dimensional crystals, dislocation is an extra line of atoms squeezed inside the lattice. The line is terminated inside the crystal in a point (dislocation core in 2D). In a triangular lattice where the perfect crystal has a sixfold symmetry, a dislocation core is composed of bound five-fold and seven-fold disclinations. A bound pair of dislocations has relatively a little effect on the translational and orientational order, see Fig. 3.7.

In KTHNY theory, a two-dimensional system can be in one of three phases: solid, hexatic, or liquid. Melting in the theory occurs in two continuous steps, which means it is a second order phase transition. In the solid phase, increasing the temperature disturbs the crystalline order; a proliferation of thermally activated dislocation pairs occurs. In this phase the translational order and the long range rotational order decay algebraically. As the temperature continues to increase, the number of dislocations pairs increases until they screen the interaction of each other. The system then reaches the second phase,

the hexatic phase, this is the first step of melting. In the hexatic phase, dislocation pairs unbind and move freely, which produces a vanishing shear modulus. In this phase, the rotational order decays algebraically while the translational order decays exponentially. This is because the translational order is determined by the average distance between free dislocations while rotational order is not effected substantially by the existence of dislocations. The hexatic is a unique phase, it is a liquid with a broken orientational symmetry. At a certain point while the temperature continues to increase, the five-fold and the sevenfold disclination pairs start to unbind. This is the second step of melting. The system then reaches the isotropic liquid state, where it loses translational and rotational order. In the liquid phase the translational and rotational order decays exponentially. The two steps of melting, the unbinding of dislocations and the unbinding of disclinations are each expected to be second order transitions.

KTHNY has inspired a large number of experiments [204, 135, 9, 142, 143, 84, 144, 184] and computer simulations [204, 33, 183] in various 2D systems. Melting of liquid crystals, electrons on liquid helium surface, gases absorbed on graphite surfaces, colloidal suspensions, dusty plasma, and diblock copolymers were all studied to examine KTHNY theory. Many of these studies give direct or indirect evidence that support the KTHNY picture. On the other hand, some studies, for example computer simulations, favor a first order transition [204] and leave open questions in the field.

### 3.3 Surface Melting

Melting and freezing phase transitions are puzzling in the sense that the liquid can be undercooled while the solid is difficult or often impossible to superheat. In general, due to the interfacial energy between the new phase and its parent, a temporary deviation from the equilibrium values of some thermodynamic variables such as temperature or pressure would be expected. But this is not true for freezing and melting transitions. Ice for example does not stay solid above 0 °C, while water can stay as a liquid under 0 °C

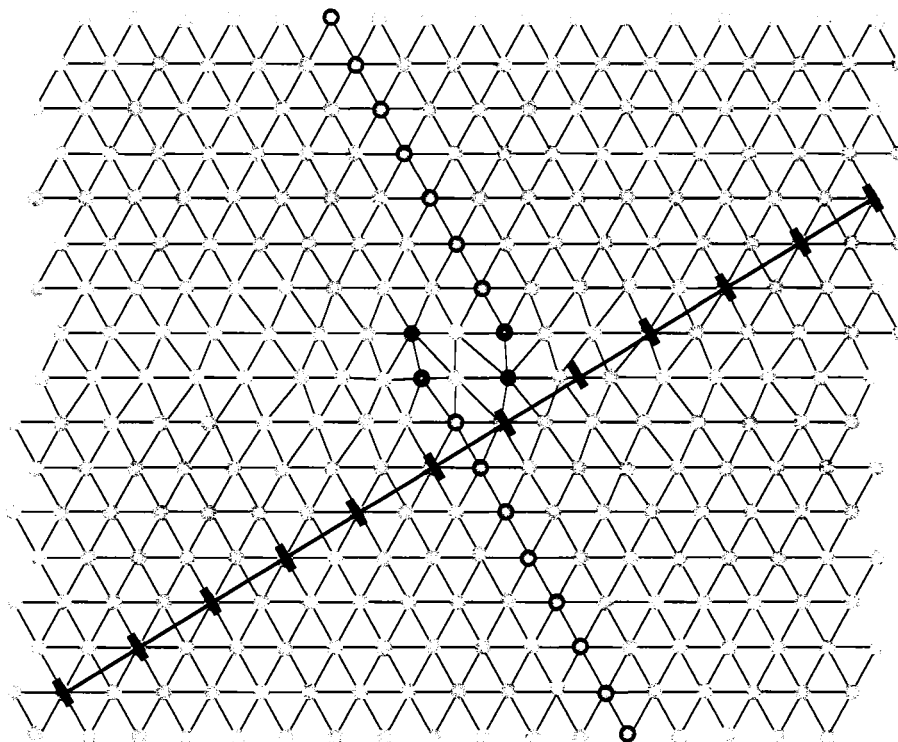


Figure 3.7: A bound pair of dislocations. This configuration has a little effect on the translational and orientational order. Blue spheres represent the extra layer due to dislocation, pink sphere has seven nearest neighbors, and red sphere has five nearest neighbors.

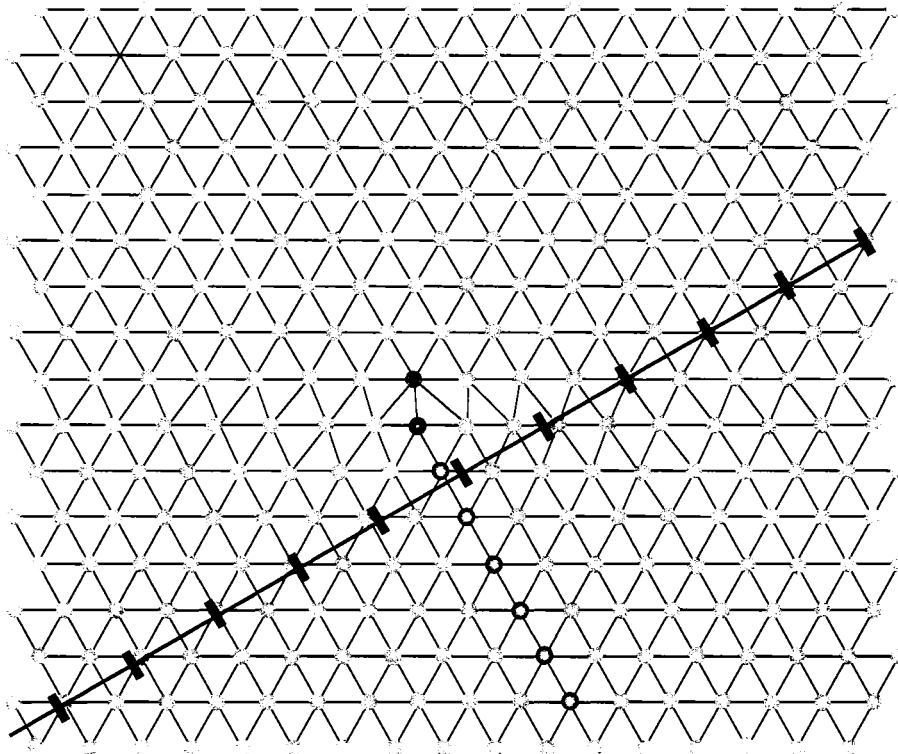


Figure 3.8: A single dislocation has a large effect on the translational order while the rotational order is not effected substantially. Blue spheres represent the extra layer due to dislocation, pink sphere has seven nearest neighbors, and red sphere has five nearest neighbors.



until it gets disrupted, and then freezes. This means that liquids have kinetic barriers in the freezing pathway, while solids apparently have no barriers in the melting pathway. The hysteresis is then working only in a half cycle of the melting-freezing transitions. Apparently the solid has surfaces that act as seeds for melting from which liquid grows as the melting temperature is approached. On the other hand, in liquids the solid seeds need not exist and supercooling can occur.

Historically, the first to notice surface melting (of ice) was Faraday (1842) [50]. He was studying melting and freezing of pieces of ice and noticed that two pieces of ice adhere if their surfaces touch one another. He concluded that both surfaces have melted layers that freeze when the surfaces are contacted. However, his experiment was not ideal, since he had temperature gradients. Tammann [50] (1910) suggested that the surface plays a decisive role in the initiation of surface melting. Stranski [49] (1942) deduced surface melting from the absence of superheating. Frenkel (1946) suggested that surfaces melt at lower temperatures than bulk melting temperature [74].

To describe surface melting, consider a semi-infinite crystal such as crystal with free surfaces in thermal equilibrium with its gas (Fig. 3.2). Along the sublimation line, solid coexists with gas, and the surface is dry. If such a solid is heated along the sublimation line it eventually reaches the triple point whereas solid, gas and liquid coexist. At that temperature ( $T_m$ ), the solid-gas interface generally wets itself with a liquid film. When the thickness of the liquid film ( $l(T)$ ) continuously grows as the temperature comes closer and closer to the triple point, we refer to this case as complete wetting or surface premelting. The thickness of the liquid film of a premelted interface diverges at the triple point. On the other hand, it is also possible that no liquid layer appears at the solid-gas interface, or that the thickness of the liquid layer saturates and remains finite as the triple point is approached. This is the case on incomplete wetting.

Surface melting (SM) and non-melting (NM) can be viewed as complete wetting and partial wetting of the surface with its own melt [209, 212, 213], see Fig. 3.9. Close to the triple point, if the surface is completely wetted by a drop of its own melt, then we have

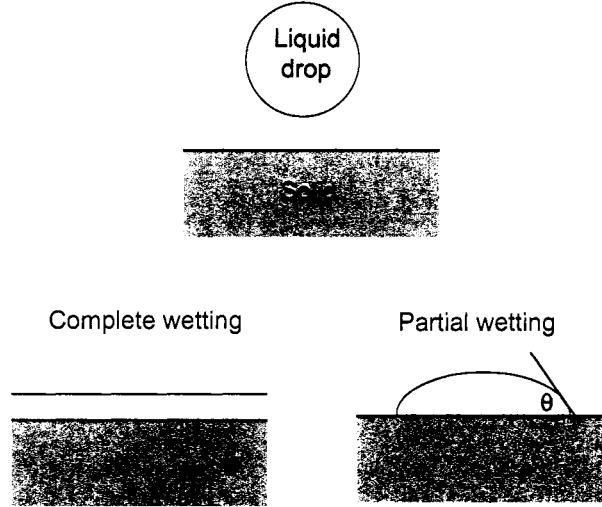


Figure 3.9: Complete wetting and partial wetting of a solid by its own melt.

complete wetting. On the other hand, if the drop partially wets the surface, then we have incomplete wetting. Surface melting and non-melting can occur in the same material, but with different crystallographic faces.

One can also express surface melting in terms of surface tensions. At the triple point, if the sum of the surface energies of the solid-liquid ( $\sigma_{sl}$ ) and liquid-gas ( $\sigma_{lg}$ ) interfaces is larger than or equal to the surface energy of the solid-gas ( $\sigma_{sg}$ ) interface, i.e.

$$\sigma_{sg} \geq \sigma_{sl} + \sigma_{lg}, \quad (3.8)$$

then complete surface wetting will occur. If the sum of the surface energies of solid-liquid and liquid-gas interface energy is less than the surface energy of solid-gas interface, then the surface will remain dry. We define the difference of the surface energies as follow:

$$\Delta\sigma = \sigma_{sg} - \sigma_{sl} - \sigma_{lg}. \quad (3.9)$$

If  $\Delta\sigma$  is positive, surface melting occurs. If it is negative, the surface will remain dry. The sign of  $\Delta\sigma$  depends on the material, and on the crystallographic face. One can

imagine that denser faces such as the (111) plane in the fcc lattice would be harder to melt than loosely packed planes such as the (110) plane.

Surface melting can also occur at temperatures below the melting temperature. This is called “*premelting*”. This happens when  $\Delta\sigma$  is large enough to compensate for the free energy associated with the existence of supercooled layers on the surface. Then the energy difference per unit area,  $\Delta G/A$ , caused by melting a solid film of thickness  $l$  on the surface of the material can be written as,

$$\Delta G/A = -\Delta\sigma + lL\rho\tau + V(l), \quad (3.10)$$

where

$$\tau = \frac{T_m - T}{T}, \quad (3.11)$$

is the reduced temperature,  $T_m$  is the bulk melting temperature,  $L$  is the latent heat of melting per unit weight,  $\rho$  is the density of the melt,  $V(l)$  is the interaction energy between solid-liquid and liquid-gas surfaces; note that  $V(l) \rightarrow 0$  as  $l \rightarrow \infty$ . At certain temperature below the bulk melting temperature, some surfaces can start to melt. At this critical temperature  $l \sim 0$ , then from equation 3.10,  $V(l) = \Delta\sigma$ . The two limits of  $V(l)$  ( $0, \Delta\sigma$ ) show that the interface interaction is repulsive if  $\Delta\sigma$  is positive (surface melting) and attractive if  $\Delta\sigma$  is negative (non-melting).

### 3.4 Experiments on Surface Melting

Surface melting has now been confirmed with large number of experiments and computer simulations. In this section I briefly describe some of the experiments. A critical factor for the clear observations of surface melting is to use ultra-pure materials with ultra-clean surfaces, since it is known that impurity elements lower the common melting temperature of substances.

Frenken and van der Veen reported the first observation of surface premelting [77,

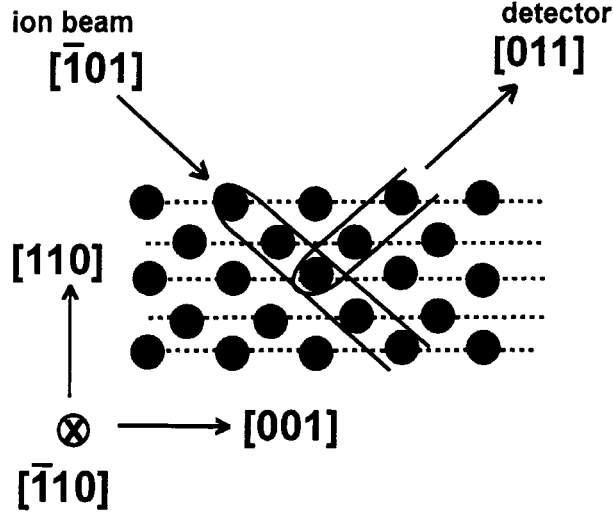


Figure 3.10: Schematic representation of shadowing and blocking effects of ion beam scattering of  $[110]$  surface. Ion beam and detector are aligned with the  $[\bar{1}01]$  and  $[011]$  directions.

76]. They investigated the Pb  $[110]$  surface in their experiment. They used a medium-energy ion scattering (MEIS) technique where the detector and the ion-beam alignments lead to shadowing and blocking of the backscattered ions as illustrated in Fig. 3.10. A parallel proton beam is aligned with  $[\bar{1}01]$  crystal axis while the detector is aligned with the  $[011]$  crystal axis. While the surface contributes most to the proton backscattered intensity, deeper atoms might also contribute due to thermal vibrations. The fact that the detector is aligned with  $[011]$  crystal axis results in blocking the backscattered protons by rows of atoms as illustrated in Fig. 3.10.

Proton scattering intensity increases as some surface layers melt, since the shadowing effect is eliminated, Fig. 3.11 shows the intensity of backscattered ions at different temperatures. Fig. 3.12 shows the number of melted layers as a function of temperature below the melting temperature,  $T_m = 600.7K$ .

Not only van der Veen and coworkers report surface premelting, they also found that surface premelting is crystal face dependent [174]. They used the same method (ion-shadowing and blocking experiment) to study melting of a cylindrical single crystal of

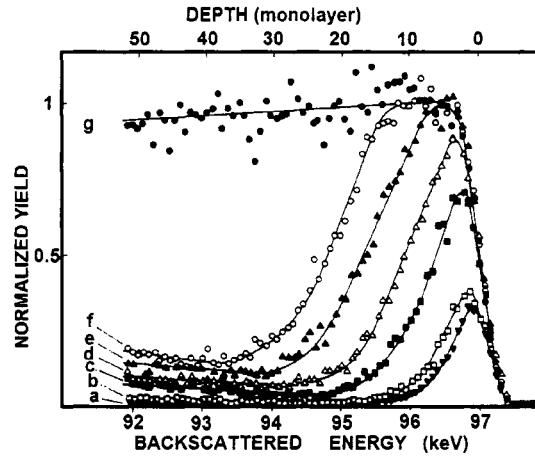


Figure 3.11: Experimental energy spectra obtained from ion backscattering in the temperature range 295-600.8 K, (a) to (g).  $T_m = 600.7K$  [77, 76].

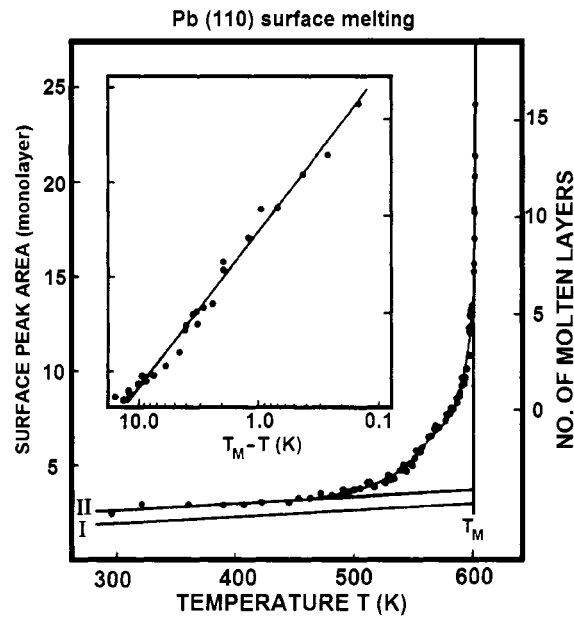


Figure 3.12: No. of molten layers as a function of temperature of [110] lead surface. [77, 76].

Pb. Their results reveal a strongly orientation-dependent disordering of the surface with increasing temperature. This indicates that melting is a heterogenous process.

Before the report of Frenken and van der Veen, there were a few experiments suggesting that the surface might premelt below the bulk melting temperature. For example Williams et al. and Kevan et al. [219, 109] predicted from the high-resolution angle-resolved-photoemission studies on Cu(110) surface that the outmost layer becomes a fluid at temperature well below bulk melting. Other reports however, such as Goodman and Somorjai [83] reported non-melting behavior of Pb (110) surface below bulk melting temperature. They used low-energy electron diffraction (LEED) and from the extracted Debye-Waller factor they concluded that mean-square displacement of surface atoms perpendicular to the surface plane is much larger than the bulk value at melting temperature as predicted by Lindemann melting model. They also reported that although the fluctuation of surface atoms is larger than the bulk, the surface atoms remained ordered until the bulk melting temperature.

More papers followed after the Frenken and van der Veen report, confirming surface premelting in other materials. Most of the materials that have been studied have face-centered-cubic structures, e.g. Al [82], Au [96], Cu [85], In [81] and Pb [174]. Amongst them Pb is the most studied. Comparisons between melting of open fcc surfaces such as (110) and more close packed faces such as (111) and (100) are carried out in this systems.

Busch et al. [27] used Medium-energy ion scattering (MEIS) to investigate the premelting of the silver (110) surface. The scattering profile is also Ion Shadowing Backscattering, see Fig. 3.10. They scanned the temperature from 300 K to 1000 K, and they found that the surface begins to disorder just above a temperature of 680 K. A complete disordered layer arises by 1000 K. Note that bulk silver melts at a temperature of 1234 K. Hoss et al. [96] used the same technique to study the premelting of the gold (110) surface in the temperature range of 60-1250 K. The backscattered intensity plateaus from 450 K

to 650 K, and then there is a kink in its intensity at 680 K where the backscattering intensity decreases. They attributed this effect to a surface roughening transition that occurs at 680 K. Above 770 K, the backscattered intensity increased much faster with increasing temperature, indicating surface premelting.

Pedemonte et al. [166] used the Low-energy ion scattering technique to study melting of aluminum (110) surface. Unlike Ion Shadowing Backscattering, they looked for the forward scattered intensity to conclude anything about surface melting. While the aluminum bulk-melting temperature is 933 K, they found the (110) surface starts to melt at 800 K, and below 800 K the surface continues to disorder as a function of temperature; the disorder is mainly due to thermally activated vacancies. From the intensity profile above 800 K, they concluded that there is correlation between nearest neighbor position within the molten layer. Speller et al. also used Low-energy ion scattering to study melting of Pb (110) surface. They found that surface disorder is a continuous process that starts at 160 K until the premelting temperature.

Pavlovska et al. [164] used low energy electron diffraction (LEED) to study melting of Pb(110) surface between room temperature and the melting point. From the results they concluded that there exist three excited state structural regimes as a function of temperature: rough, quasi-crystalline and quasi-liquid. Yang et al. [231] also used the LEED technique to study Pb (100) surface. From the non-Bragg type of electron scattering they concluded that surface undergoes a weak disordering at about 570 K, which is 30 K below the bulk melting temperature. This disordering is preceded by a generation of a very high density of surface vacancies at 510 K.

Dosch et al. [65] used grazing-angle X-ray scattering to study surface melting at the Al(110) surface. Using the vanishing perpendicular momentum transfer of the (002) Bragg peak, they obtained information about the near-surface crystallinity and disorder. They concluded that the Al(110) surface starts to melt at about 770 K. Below 770 K they concluded that there are strong near-surface anharmonic lattice vibrations and surface roughening effects that occur as precursors to the onset of surface melting. Breuer et al.

[17] used X-ray photoelectron diffraction to study surface melting of the Pb(110) surface. They confirmed the results of Frenken and van der Veen [76].

Krim et al. [117] and Larese et al. [122] used neutron diffraction to study melting of layers of oxygen and argon gases adsorbed on graphite substrate. They found that the layers disorder sequentially from the outermost layer of the film toward the graphite surface with the melting of individual layers occurring gradually over certain temperature ranges. They also found that the quantity of liquid varies logarithmically as a function of temperature close to the bulk melting temperature.

Polcik et al [175]. used polarization-dependent surface-extended x-ray-absorption fine-structure measurements to study Al(110) and Al(111) surfaces at temperatures from 100 K up to the melting point ( $T_m = 933.5$  K). They concluded that the surface melting temperature of Al(110) is above about 800 K. They found the diffusion of the atoms on the surface is anisotropic. The quasi-liquid layers were shown to have residual order during surface melting consisting of intact (110) rows or segments of atoms which have liquid-like mobilities.

Other techniques such as Core-level photoemission spectroscopy [210], ellipsometry [214], electron microscopy [126, 1, 103], and Electron energy loss spectroscopy [140, 165], were also used to study melting of different materials such as gallium, germanium, aluminum, and lead. Collectively the above techniques concluded the following:

1. For metals, a melted layer of quasi-liquid occurs on crystal faces with open atom packing such as the (110) faces of an fcc crystal.
2. The quasi-liquid layer's structural, dynamical, and transport properties are intermediate between those of the solid and the pure liquid. The interaction between the melted layer and the crystal underneath induces some sort of order in the melted layer. There is anisotropy of the diffusion constant of the surface atoms. The mobility of surface atoms exceeds the bulk-liquid value with the diffusion constant along [110] being larger than that in the [100] direction. The diffusion along [100] is described in terms of jumps over single lattice spacing while diffusion along [110] seems to be continuously distributed



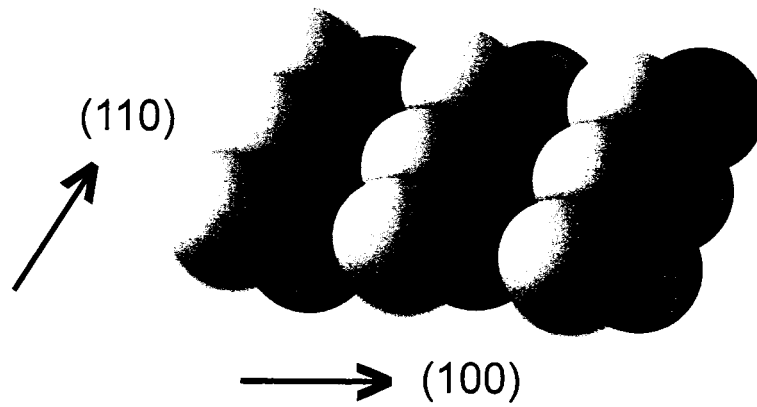


Figure 3.13: Fcc  $(110)$  surface

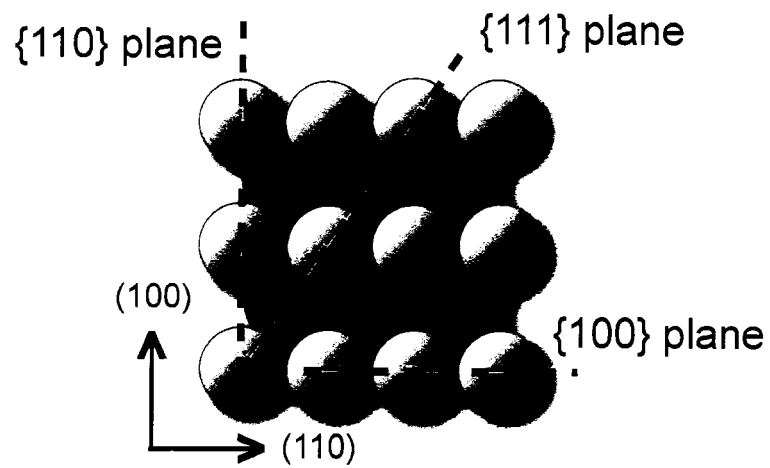


Figure 3.14: Fcc  $(110)$  surface

between zero and a maximum value [75].

3. Densely packed crystal faces such as fcc(111) are generally non-melting, i.e. remain completely dry. Metallic surfaces with intermediate atom packing densities such as the (100) faces of fcc crystals tend to exhibit incomplete melting (i.e. wetting by a melt of microscopic thickness that does not diverge as  $T_m$  is approached).

4. Noble-gas crystals and weakly bonded crystals show complete melting for densely packed crystal faces.

5. Covalently bonded crystal surfaces are more likely to exhibit incomplete surface melting than surfaces of metallic crystals.

6. Surface melting occurs, apparently, on all the high-symmetry crystal faces of ice [78].

### 3.5 Phenomenological Theory on Surface Melting

The first model of surface melting in the framework of Landau-Ginsburg phenomenological theory was worked out by Lipowsky [129, 130, 131, 133]. As mentioned before, the Landau free energy is just a power series of the order parameter. In the case of the semi-infinite system with surfaces, the order parameter will be function of position.

Consider a crystal which is infinite in the  $x$  and  $y$  directions and with a plane surface at  $z = 0$ . The order parameter,  $M$ , is then a function of  $z$ :  $M = M(z)$ . The order parameter can be the density, or it can be in more complicated form that contains information about the periodicity of the crystal. The Landau expansion for the free energy per unit area, assuming the surface is at  $z = 0$ , has the form,

$$F\{M\} = \int_0^\infty dz \left[ \frac{1}{2} \left( \frac{dM}{dz} \right)^2 + f(M) + \delta(z) f_1(M) \right], \quad (3.12)$$

where

$$f(M) = -HM + \frac{1}{2}a(T)M^2 + \frac{1}{4}uM^4 + \frac{1}{6}vM^6 \quad (3.13)$$

is the bulk free energy. If  $u < 0$ , this leads to first order transition. Minimizing the bulk free energy with respect to the order parameter, one obtains  $a = a^* = 3u^2/16v$  at the transition temperature  $T^*$ , for  $H = 0$ . At the transition the order parameter jumps by an amount  $(3|u|/4v)^{\frac{1}{2}}$ .

The last term in equation 3.12 is an additional term accordingly for the microscopic changes of the interaction parameters near the free surface, which can be expanded in powers of  $M$  up to second order, i.e.,

$$f_1(M) = -H_1 M + \frac{1}{2} a_1 M^2. \quad (3.14)$$

Minimizing the free energy in equation 3.12, one obtains the order parameter of the surface layer as a function of temperature,

$$M_1 \propto \begin{cases} \text{constant}, & a_1 < (a^*)^{1/2}, \\ |T - T^*|^{1/4}, & a_1 = (a^*)^{1/2}, \\ |T - T^*|^{1/2}, & a_1 > (a^*)^{1/2}. \end{cases} \quad (3.15)$$

Thus two different types of surface transitions are obtained. In the case  $a_1 < (a^*)^{1/2}$ , the surface remains dry (or ordered) until the bulk melting temperature. In the other cases the order parameter decay is a power law as a function of temperature. In this case there is an interface at  $z = l$  which separates a surface layer of the ordered phase from the disordered one. This interface becomes delocalized since,

$$l \propto |\ln M_1| \propto |\ln |T - T^*||. \quad (3.16)$$

Note, wetting or non-wetting of the surface depends on the parameters  $a$  and  $a_1$  which in turn depend on the microscopic details of the solid phase and the interface. Although this model does not include the periodic nature of the solid phase, i.e. the order parameter does not include the periodic structure of the solid, the model shows that wetting of the surface is possible; it also predicts the logarithmic divergence of the thickness of the melted layer, eqn. 3.16.

### 3.6 Molecular-Dynamics Simulations of Surface Melting

Molecular-Dynamics (MD) simulations are very important tools with which to study melting with some microscopic details. One can derive information on atomic dynamics in the solid-liquid-gas interface using MD. Mainly two types of systems were studied by MD simulation, the two-body Lennard-Jones (LJ) potential and metals. The LJ potential is suitable for rare gas and van der Waals molecular crystals, but not for most other solids. Many body potentials, such as the embedded-atom model [97, 37], the effective medium interaction potential [203, 202], and the glue potential [120], are more suitable for metals.

Broughton et al. [18, 23, 22, 20, 21, 19, 24] carried out molecular-dynamics investigations of surface melting of Lennard-Jones systems. They found surface pre-melting occurs at all fcc crystal surfaces. Many molecular-dynamics studies of Lennard-Jones systems followed and obtained surface melting of close-packed surfaces ((111) or (100)) [176, 69, 68].

More realistic potentials are the basic difficulty in such studies. The potential has to include many-body effects. Few many-body model potentials have been used in MD simulations for metals. Stoltze et al. [203, 202] used an effective medium interaction potential to study pre-melting of aluminum surfaces. They found (110) surface premelts whereas the more close-packed surface, (111), had a much weaker disordering. The embedded-atom model was used to study premelting of Ni(110) surface [35]. They found premelting occurs at temperatures as low as 1450 K, while the bulk melting temperature is 1700 K. They also found that surface atoms vibrate more than bulk ones and when the surfaces melt, atoms diffuse in (110) direction more than in the (100) direction. Barnett et al. [11] also used the embedded-atom model to study surface premelting of Cu(110), they found the surface premelts below the bulk melting temperature. The glue potential has been used as a many-body-force potential to study melting of Au(111) surface [30, 31, 100, 99]. Premelting was found not to occur on Au(111) surface; in

addition the nonmolten surface can be overheated for as much as 100 to 150 K above melting temperature.

To summarize, there is strong orientation behavior for surface melting if many-body-force potentials are used. In contrast, when the Lennard-Jones potential is used, premelting occurs at all fcc crystal surfaces. The reason for this difference is the enhancement of the surface stability due to the many-body-force potential.

### 3.7 Density Functional Theory

As we saw before, statistical mechanic techniques that deal with phase transition construct simple free energy functions that are expressed in terms of order parameters. Density, local magnetization, local periodic order in crystal and orientational order in liquid crystals are examples of order parameters. The choice of order parameter plays a key role in constructing the free energy. Sometimes two order parameters can be chosen such as density and the periodic order parameter in liquid-solid transitions. The minimization of the free energy is then used to locate the phase transition. This approach is valid in a homogeneous system, where the order parameter does not change with position in each phase. Practically, the homogeneous system does not exist, there will always be a wall or an interface between two phases that makes the order parameter vary through the space near interfaces. For example, the density can vary by a few orders of magnitude over very short distance at gas-liquid coexistence. The order parameter can also vary with position if there is an external field that also varies spatially. Because of the inhomogeneity of the system we get new physical effects such as surface tension, molecular alignment, adsorption, and surface phase transitions. Since the interface is in equilibrium with the bulk, the equilibrium conditions are that the temperature and chemical potential must be equal throughout the interface, while the number of molecules,  $N$ , can fluctuate. For such systems the grand canonical variables are then convenient  $(T, V, \mu)$ , and the appropriate free energy is the grand potential,  $\Omega$ . Then if we have a system at constant  $T, V, \mu$

and  $S$  (surface area), then at equilibrium  $d\Omega = 0$ , while for the non-equilibrium system,  $d\Omega < 0$ . This means that at equilibrium,  $\Omega$  is at its minimum value.

The goal of density-functional-theory (DFT) is to construct a free energy function for inhomogeneous systems wherein the order parameter can vary spatially. DFT is so far the most successful theory to study, with some microscopic detail, melting and freezing. Also DFT is used to study the effect of different things such as the effect of walls, porous media, and external potentials on phase transitions.

Historically, DFT was first applied by Hohenberg, Kohn, and Shan [94, 112] to quantum systems. They used the DFT method to describe the ground state (zero-temperature) density of a non-uniform electron fluid such as electron fluid near metallic surfaces and interfaces. They solved Schrödinger equation to get the electron density rather than wave function at different points in the space. Ebner and Saam [191, 189, 190, 188, 187] applied the same idea to classical fluids where, instead of dealing with electrons, they dealt with atomic centers. The main focus of DFT is to get the density profile of inhomogeneous fluids. One good paper on this subject is written by Robert Evans [71]

In DFT that the grand potential is a functional of the one body density  $\rho(r)$  and the grandcanonical free energy function reaches its minimum at the equilibrium density. In the beginning, a density profile which is not the equilibrium is assumed, and then the grand free energy is shown to be minimum at the equilibrium density profile. In fact the density profile is what we try to get out of the calculations. At equilibrium, the external potential  $V_{ext}(r)$  will determine the equilibrium density profile. Knowing the density profile and the grand free energy, we can calculate the surface tension and all thermodynamic properties since  $\Omega = -PV + \gamma S$ , where  $\Omega$  is the grand canonical free energy,  $P$  is the pressure,  $V$  is the volume,  $\gamma$  is the surface tension and  $S$  is the surface area. One can then write the grandcanonical free energy function in the form [71],

$$\Omega(T, \mu, [\rho(r)]) = F(T, [\rho(r)]) + \int d^3r \rho(r) [V_{ext}(r) - \mu], \quad (3.17)$$

where  $T$  is the absolute temperature,  $\mu$  is the chemical potential, and  $F(T, [\rho(r)])$  is the

Helmholtz energy functional. At equilibrium density, the grandcanonical free energy function is minimum,

$$\delta\Omega(T, \mu, [\rho(r)])/ \delta\rho|_{\rho=\rho_o(r)} = 0. \quad (3.18)$$

Knowing the equilibrium density profile, one can then get the equilibrium grand canonical free energy,

$$\Omega(T, \mu, [\rho_o(r)]) = \Omega(T, \mu). \quad (3.19)$$

For noninteracting system  $F(T, \rho)$  can be calculated exactly [135],

$$F(T, [\rho]) \equiv F_{id}(T, [\rho]) = k_B T \int d^3r \rho(r) [\ln(\Lambda^3 \rho(r)) - 1], \quad (3.20)$$

where  $F_{id}(T, \rho)$  is the ideal free energy function,  $k_B$  is the Boltzmann constant, and  $\Lambda$  is the de Broglie wavelength,

$$\Lambda = \sqrt{h^2/2\pi m k_B T}, \quad (3.21)$$

where  $h$  is Planck's constant. It is then convenient to separate the free energy function in equation 3.17 to ideal, and excess terms where the ideal term has no interaction (ideal gas) and the excess term contains all the correlations between particles.

$$F(T, [\rho(r)]) = F_{id}(T, [\rho(r)]) + F_{excess}(T, [\rho(r)]). \quad (3.22)$$

As a first order approximation,  $F_{excess}$  can be considered as a perturbation due to the potential  $u(r_{12})$ , where  $u(r_{12})$  is the perturbation potential that deviate from the ideal case, which is mostly the attractive part of the potential.

$$F_{excess}(T, [\rho(r)]) = \frac{1}{2} \int \int d^3r_1 d^3r_2 \rho(r_1) \rho(r_2) g(r_1, r_2) u(r_{12}). \quad (3.23)$$

In the mean field approximation we will consider  $g(r_1, r_2)$  as constant (equal to 1) and we will ignore the oscillations of  $g(r_1, r_2)$  about the unit value. The excess free energy will be then,

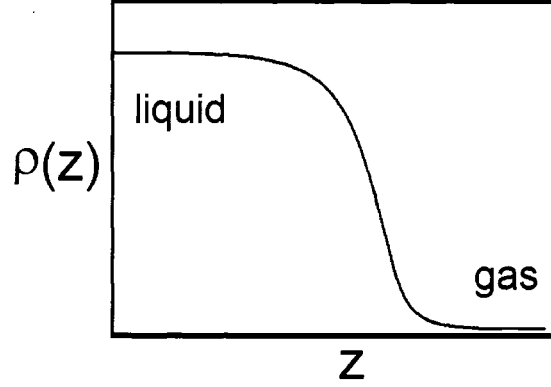


Figure 3.15: Density profile throughout the interface of a liquid-gas system

$$F_{excess}(T, [\rho(r)]) = \frac{1}{2} \int \int dr_1^3 dr_2^3 \rho(r_1) \rho(r_2) u(r_{12}). \quad (3.24)$$

The grandcanonical free energy function is then,

$$\begin{aligned} \Omega(T, \mu, [\rho(r)]) = & F_{id}(T, [\rho(r)]) + \frac{1}{2} \int \int dr_1^3 dr_2^3 \rho(r_1) \rho(r_2) u(r_{12}) \\ & + \int d^3r \rho(r) [V_{ext}(r) - \mu]. \end{aligned} \quad (3.25)$$

In the Local Density Approximation, LDA,  $F_{id}(T, [\rho(r)])$  can be approximated by the ideal free energy of a uniform fluid of density  $\rho = \rho(r)$ , where  $\rho(r)$  is the density of the inhomogeneous fluid at position  $r$ . In this approximation we ignore the effect of the density gradients on the ideal part of the free energy, see Fig. 3.15. The grand canonical free energy is then,

$$\begin{aligned} \Omega(T, \mu, [\rho(r)]) = & \frac{1}{2} \int \int dr_1^3 dr_2^3 \rho(r_1) \rho(r_2) u(r_{12}) \\ & + \int d^3r \rho(r) [V_{ext}(r) - \mu + k_B T [\ln(\Lambda^3 \rho(r)) - 1]]. \end{aligned} \quad (3.26)$$

The above Local Mean Field approximation can be applied to many fluidic systems



such as liquid-liquid density profile in liquid-liquid equilibrium systems, gas liquid interfaces or to micellar systems. While LDA works fine for liquid systems, it doesn't work for solid systems such as solid-liquid or solid-gas coexistence where the atoms in the solid phase are fixed in space, ; in this case the density oscillates, so that near the interface the atom density oscillates and settles down into the fluid phase, see Fig. 3.16. The density then has very large values in peak positions and almost equal zero at dip positions. The local density approximation (LDA) then become impractical since we cannot neglect the effect of the density gradients; also the density at some positions is as much as few times the density of the homogeneous fluid.

Ramakrishnan and Yussouf [185], and Haymet and Oxtoby [87, 161] proposed a functional that describes freezing. They used Taylor expansion to expand  $F_{excess}$  up to second order as a density functional around the density of a fixed homogeneous fluid. In their functional, the first term is just a constant, the second term is linear in density while the third term is the direct correlation function for the homogeneous fluid. Since they used the density of a fixed homogeneous fluid as reference, the expansion needs to go to the third order to be improved.

Tarazona [208, 207], and Curtin and Ashcroft [44, 45] constructed a better approximation named Weighted Density Approximation (WDA). They used more information from the liquid phase to describe the freezing state. Many other theories followed after that such as Modified Weighted Density Approximation (MWDA) [54] and Hybrid Weighted Density Approximation (HWDA) [125]. Note that all these approximations used information from the liquid states to describe the solid states.

### 3.8 Density Functional Theory and melting

The density profile of a solid-gas interface for a given interaction potential can be obtained by direct minimization of a density functional with a good bulk phase diagram. Attention has mostly been given to the Lennard-Jones system which represents a model system for

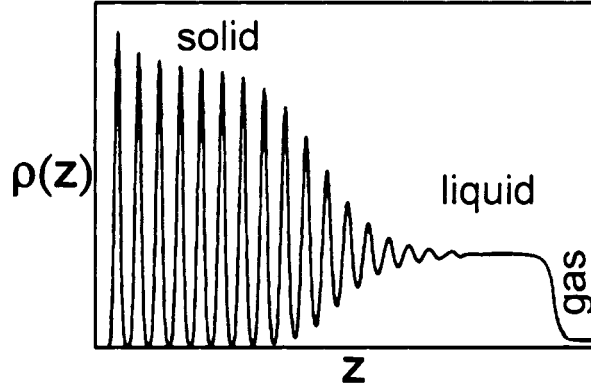


Figure 3.16: Density profile throughout the interfaces of a solid-liquid-gas system

rare gases, [135]. Tarazona [208, 207] constructed and used *WDA* approximation to locate the liquid-solid phase transition of hard spheres. He obtained very good results for the location of solid-liquid phase transition and for the surface tension. Chereponova et al. [38, 39] used a Lennard-Jones potential and obtained surface melting. Ohnesorge et al. [154, 156, 157, 153] used *WDA* functional as discussed before and found surface melting to occur for (110) and (100) surfaces of *FCC* crystals. Their results are supported by the experimental results of Pluis et al. [174].

### 3.9 Grain Boundary Premelting

The roles of surfaces in melting have been discussed. Grain boundaries are another important quasi-two dimensional interface that can potentially lead to heterogeneous melting of a solid material. Many simulations on the structural changes of grain boundaries have been performed in the last three decades. Many-body potentials and system size are the leading difficulties in such studies. Two-body potentials such as Lennard-Jones potential simply don't fit all the parameters of metals. Also grain boundaries are not fixed in space, they are mobile. During the simulation time, grain boundaries move away from the tested region.

Kikuchi and Cahn [110] developed a two-dimensional (2D) lattice gas model that is

capable of producing gas, liquid and two orientations of solid phase. They found that the grain boundary starts to disorder when heated to about  $0.50T_m$ , and that the disordering progresses gradually as the temperature increased. The thickness of the boundary diverged with temperature as  $-\ln(T_m - T)$ , and the boundary was completely wet with liquid at  $T_m$ . In two dimensional crystals, a grain boundary is one dimensional. Its not clear if the gradual disorder is a consequence of the dimensionality or if it is a general property that can be applied to 3D systems.

Ciccotti et al. [40] used the Lennard-Jones potential in molecular dynamics simulations. They obtained results which appeared to be qualitatively similar to those of Kikuchi and Cahn. They found that the structure factor for the core region of the boundary began to decrease significantly at about  $0.45T_m$ ; it then decreased smoothly at an accelerating rate until it apparently reached zero at  $T_m$ . The thickness of the disordered region increased with increasing temperature. They also found that the diffusion coefficient of atoms in the disordered boundary is comparable to, although lower than, atoms in the bulk undercooled liquid at the same temperature.

Broughton and Gilmer [18] also used the Lennard-Jones potential in molecular dynamics simulations and they obtained similar results to Ciccotti et al. They examined three boundaries that have different crystalline orientations. High-energy boundaries showed disorder below melting temperature while low energy boundaries remained solid even at temperatures higher than melting temperature (i.e. superheating). The disordered region was initially localized to the boundary and then at  $T_m$  the region gradually expanded. Their conclusion is that grain boundary melting is not a phase transition that can be identified at a temperature below  $T_m$  and the thermodynamic parameters are continuous functions of temperature. In other words the disorder that appears on the boundary increases gradually (the quasiliquid layer retains some crystalline order) and only reaches liquid state at melting temperature.

Nguyen et al. [148, 150, 149] and Ho et al. [92, 93] used a Morse potential in molecular dynamics simulations and obtained similar results to Broughton and Gilmer. However, their simulation was performed at constant pressure and showed a highly disordered boundary at temperature as low as  $0.5T_m$ . They also found that grain boundary premelting is an abrupt transition with temperature. Below the transition temperature thermal disorder occurs at the boundary, but the interfacial width remains constant, while above the transition temperature the interfacial region behaves like a melt. Deymier et al. [55] used similar methods and obtained similar results. Nguyen et al. then followed with more recent simulations [147], where they used embedded-atom potential instead of just the two-body potential. They also estimated the bulk melting temperature in a more accurate way. They suggested that the difference in the results between the current work and the previous works can be traced to the incorrect identification of  $T_m$ . Their main conclusion was that the premelting that appears on the grain boundary is a meta-stable state; if we wait long enough, the disordered layers would recrystallize. However melting starts at grain boundaries as it starts on surfaces at the melting temperature. They also showed that as the temperature increases, some surface layers start to disorder, but if we wait long enough some of the disordered layers recrystallize.

Alsayed et al. [5] experimentally studied melting of colloidal crystal (this thesis). The crystals were equilibrium close-packed three-dimensional colloidal structures made from thermally responsive microgel spheres. The thermal response of the microgel enabled precision control of particle volume fraction. They found that premelting occurs at grain boundaries and dislocations located within bulk colloidal crystals. They used real time video microscopy to track each particle. They found that the amount of premelting depends on the nature of the interfaces and defects. They used particle tracking techniques to study particle fluctuations nearby and far from defects. They found that particles nearby defects have higher values of the Lindemann parameter.

Finally, a hot-stage transmission electron microscopy (TEM) experiment by Hsieh and Balluffi [98] suggests that GB premelting likely occur but only above  $0.999T_m$  for

pure Al. The situation is different in the case of segregation to the boundary, as for example in Cu-Bi [58] or Ni-W [136], where segregated impurities effectively help premelting on the grain boundary.

From the above investigations one can draw an approximate picture of grain boundary transition at high temperature. All the high-energy grain boundaries exhibit a universal disordered structure at high temperature. These disordered layers are confined between two ordered surfaces and constrained to a constant density (which means that the pressure increases as the disorder increases). These severe confinement and density constraints are expected to reduce diffusion. In fact, diffusion occurs mainly by vacancy migration [18]. On cooling, the confined liquid undergoes a reversible transition to a confined amorphous solid with a common grain boundary's width. By contrast, low-energy boundaries remain crystalline from zero temperature all the way up to  $T_m$ .

## Chapter 4

# Phase Transitions in Liquid Crystals

### 4.1 *fd* Virus and Its Phase Behavior

While spherical particles in the micron size range are routinely synthesized, attempts to chemically synthesize monodisperse rods have not been so successful, and a wide distribution of rod lengths significantly affects the phase behavior of the system. Biological rather than a chemical synthesis however, has proven to be much more successful. TMV and *fd* are rod-like viruses, for example, that are easily engineered to be identical to each other. As a result rods with very high monodispersity are produced. Because of their high monodispersity, rod-like viruses are the only experimental hard rod system presently available whose phase behavior agrees with theoretical predictions [218, 59].

The bacteriophage *fd* is a semiflexible rod-like molecule. Its contour length ( $L_c$ ) is about 880 nm, diameter ( $D$ ) is 6.6 nm, and persistence length ( $L_p$ ) is about 1  $\mu\text{m}$  to 2.2  $\mu\text{m}$  [59]. *fd* virus is a highly charged rod too. The charge density is 1  $e/\text{\AA}$ . The surface charge is effectively screened in solution at a high salt concentration. *fd* virus can be modeled very well as a hard rod at about  $\sim 200$  mM salt concentration in the buffer.

Because of its anisotropic shape ( $L_c/D=135$ ), suspensions of *fd* virus exhibit isotropic, nematic, and smectic phases with increasing *fd* concentration [61]. In the isotropic phase,

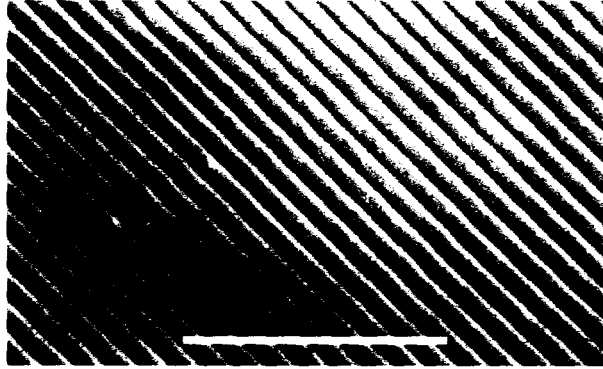


Figure 4.1: Optical microscopy micrograph of smectic phase in *fd* virus suspension.

the orientation of rods is random. In the nematic phase, the rods are oriented along approximately the same direction, but the center-of-mass positions are random (long range orientational order and short range positional order). In the smectic phase, see Fig. 4.1, the rods have both long range orientational order and long range one-dimensional (solid-like) positional order, while liquid-like order in the other two directions.

Onsager in 1949 was the first to show that hard core repulsion between highly anisotropic rods is sufficient to produce a stable liquid crystalline nematic phase [159]. After that, theory and computer simulations showed that hard rods also form stable smectic phases [95, 73, 14]. Historically the isotropic-nematic phase transition predicted by Onsager preceded the prediction of the first-order liquid to crystal phase transition that occurs in hard sphere suspensions [170, 4]. In both cases, hard spheres and hard rods, the phase transitions are entirely entropy driven. An experimental signature of entropy driven transitions is its independence of temperature. Many phases after that were discovered in colloidal systems in which the shape of the particles and the shape of the repulsive part of the interaction between individual particles play the key role.

Fraden and coworkers used experimental, theoretical, and simulation methods to investigate the relationship between *fd* rod interactions and derived phase diagrams [61]. They changed the intermolecular interaction potential by changing the suspension ionic strength or by adding non-adsorbing polymers [64]. They located the isotropic, cholesteric

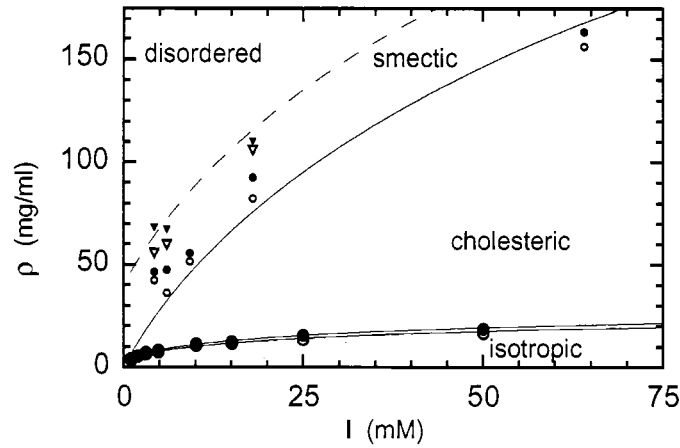


Figure 4.2: Phase behavior of *fd* virus suspensions at different ionic strengths [61].

(nematic) [107], and smectic phases at different ionic strengths and *fd* concentrations, see Fig. 4.2. They used standard molecular cloning techniques to change the aspect ratio of the *fd* particles. They found that in the limit of high ionic strength the phases of *fd* virus quantitatively agrees with Onsager theory for the isotropic-nematic (I-N) phase transition in hard rods. The addition of non-adsorbing polymers introduces attractive interactions between rods. They observed isotropic-smectic (I-S) phase transition as the strength of this attraction is increased [64]. They also investigated the influence of hard spheres on the nematic-lamellar phase transition. The lamellar phase is a microphase separated state in which the entire bulk is spanned by interfaces between two materials. Here the lamellar phase consists of layers of spheres intercalated between layers of rods [2]. They concluded that adding small spheres stabilizes the lamellar phase and destabilizes the nematic phase [61, 60, 62, 59, 206, 205, 2, 63, 179, 64].

Alsayed et al. [6] prepared a suspension composed of rodlike *fd* virus and thermosensitive polymer poly(N-isopropylacrylamide). The mixture phase diagram is temperature and concentration dependent. They found a variety of stable and metastable phases. They also observed directly melting of lamellar phases and single lamellae. They found that lamellar phases swell with increasing temperature before melting into the nematic phase.



isotropic                  nematic                  smectic

Figure 4.3: Phases behavior of a hard rod suspension. The illustration shows stable phases that appear in a system of hard rods. The transitions in hard particle suspensions are temperature independent; concentration is the only parameter that determines the phase diagram. Hard rods form stable isotropic, nematic, and smectic phases with increasing rod concentration.

The highly swollen lamellae can be superheated as a result of topological nucleation barriers that slow the formation of the nematic phase.

## Chapter 5

# Temperature Sensitive Polymers

### 5.1 Thermoresponsive poly(N-isopropylacrylamide) polymers and colloids

Thermoresponsive polymers are polymers that combine hydrophilic and hydrophobic parts into their unit monomers. At low temperature, the solvent quality is either good or poor, and it is the opposite at high temperature. The characteristic feature of many aqueous polymer solutions is that a phase transition can occur upon heating. The transition temperature is known as the lower critical solution temperature (LCST). Some examples of water-soluble polymers displaying inverse solubility upon heating are methylhydroxypropyl cellulose [111], poly(vinylcaprolactam) [70], and poly(N-isopropylacrylamide) (PNIPA), [193].

PNIPA is known to undergo a temperature induced phase transition in water, where it evolves from hydrophilic to be hydrophobic, at the LCST of 31-34 °C. The solvent quality (water) changes from good to poor when the LCST is approached. This phase transition was studied in great detail for different architectures including linear chain PNIPA, chemically cross-linked microgels, and macroscopic gels using various methods like static and dynamic light scattering, differential scanning calorimetry, viscometry, and

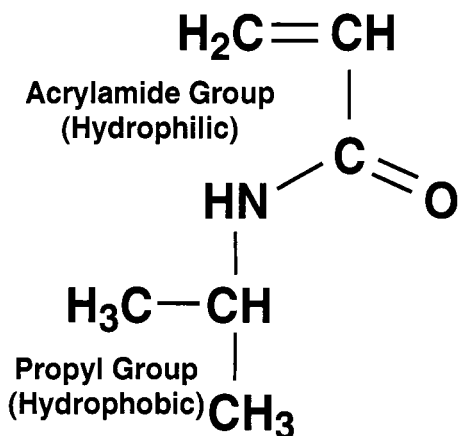


Figure 5.1: NIPA monomer molecule.

rheology [111, 70, 193, 196, 72, 222, 114, 197, 228, 127, 113, 211, 186, 118, 221, 160, 90, 7, 169]. For single linear PNIPA, the flexible polymer chain contracts with increasing temperature and a coil-to-globule transition is observed.

Swollen PNIPA microgels are also known to undergo a continuous temperature-induced volume phase transition when the LCST is approached. At temperatures below the LCST the microgel spheres are highly swollen. Above the LCST water becomes a poor solvent leading to the collapse of the particles. Therefore the particle size decreases with increasing temperature. The advantage of thermoresponsive particles over the rigid hard spheres for some studies is that the volume fraction of the sample can easily be controlled by simple temperature changes while the particle number density is kept constant. Since the transition is induced by hydrophilic and hydrophobic effects, salt surfactants, variations in the solvent compositions or copolymerization with charged monomers can all, in principle, be used to alter the transition (LCST) temperature [108, 233, 101, 195].

Temperature sensitive PNIPA microgel colloids gained interest particular due to their potential use in many technological applications, including controlled drug delivery systems and biotechnology. If a collapsed microgel is placed into an aqueous drug solution at  $T < LCST$ , the PNIPA microgel particle will swell and small drug molecules will freely penetrate the pores of the polymer network. The PNIPA particle will also squeeze out the

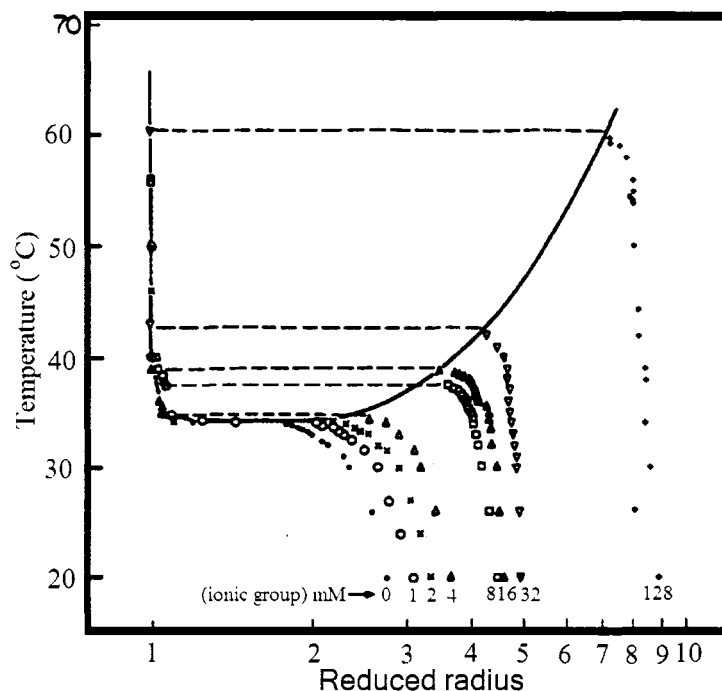


Figure 5.2: Equilibrium radius of N-isopropylacrylamide/sodium acrylate copolymer gels in pure water plotted as a function of temperature. The mM value indicates the concentration of ionizable monomer, sodium acrylate, which is incorporated into the gel network at the preparation. The total monomer concentration is fixed to be 700 mM [138].

encapsulated drug after the solution is heated up to  $T > LCST$ . The LCST of PNIPA based microgels can be adjusted to the human body temperature by copolymerization with other hydrophilic or hydrophobic polymers [193, 168, 56].

Matsuo et al. studied the swelling behavior of N-isopropylacrylamide/sodium acrylate copolymer in pure water. The radius of spherical gels made of this copolymer as a function of temperature is shown in Fig. 5.2 [138].

Wu et al. [226, 227] used static and dynamic light scattering (SLS and DLS), and have shown that the microgel particle-particle interaction potential depends on temperature. Hellweg et al. [89] determined the structure of colloidal PNIPA microgel particle crystals using SANS. A face-centred-cubic lattice was observed. Lyon and coworkers [53, 52, 51] reported on the assembly of colloidal PNIPA crystals. They observed a change in the

lattice constant as a function of concentration by laser scanning confocal microscopy. This behavior occurs because swollen microgel particles are not rigid and shows soft sphere behavior when they are overpacked.

Richtering and coworkers [194] studied the rheology and phase behavior of the concentrated PNIPA microgel particle systems. They reported the formation of colloidal crystals made of the microgel particles. Rheological measurements at volume fractions  $\phi < 0.5$  agreed well with that of hard sphere suspensions. At higher effective volume fractions, a soft sphere interaction potential was concluded. They then used small-angle neutron scattering (SANS) to study the change of the size of individual microgel particles with concentration. They found that the overall particle size and the correlation length of the internal polymer network decreased with concentration, revealing the increasing compression of the spheres. Thus, the particle form factor of the swollen PNIPA microgels particles depends on concentration. A modeling for the scattering intensity in dilute suspensions showed that the radial density profiles in the swollen state are not homogeneous, but gradually decayed at the surface. They also studied particle-particle interactions for microgel suspensions at different temperatures [200]. They found the potential does not change significantly between 25 and 32 °C, even up to approximately one degree below the lower critical solution temperature (LCST). Small-angle neutron scattering (SANS) intensity was described very well by the hard sphere structure factor when an effective hard sphere particle size and volume fraction were used. Combining the modeling for the scattering intensity and the rheological measurements they found deviations from true hard spheres behavior at volume fraction higher than 0.35 [200, 199, 201, 198].

## Chapter 6

# Sample Preparation and Characterization

### 6.1 Emulsion Polymerization

In this section, I will describe emulsion polymerization in a general way. However, it should be noted that the subject is much more complex than my general discussion might indicate. Many side reactions can occur, etc.; thus emulsion polymerization is a major research subject of its own right in polymer chemistry. First let's define an emulsion. An emulsion arises from two liquids that are immiscible. One liquid is dispersed as droplets in the other. The former is called the *dispersed phase* while the latter is called the *continuous phase*. For example on adding oil to water, we form an emulsion. Generally, the droplets are not stable over long times; the mixture sooner or later phase separates into two immiscible layers. In order to avoid this effect, continuous vigorous agitation of the mixture and/or the addition of surfactants are required.

The surfactant is a molecule with a hydrophilic head (usually one that carries charge) and hydrophobic tail (usually a carbon chain). In our lab, we synthesize latex colloidal particles using the emulsion polymerization method. The dispersed phase (monomer)

is immiscible in the continuous phase, and the resultant particles (or polymer) is also immiscible in the continuous phase. They are dispersed and stabilized in water due to the charges on their surfaces. There also exists another method called *dispersion polymerization*, wherein the monomer is miscible in the continuous phase, but the resultant particles (or polymer) are immiscible in the continuous phase. This method is used in the synthesis of polymethylmethacrylate (PMMA) particles which are sterically stabilized with grafted poly-12-hydroxystearic acid. Here the monomer is soluble in an organic solvent, while the polymer is not. The resultant particles do not have charge, the particles are stabilized sterically by the grafted poly-12-hydroxystearic acid.

Emulsion polymerization takes its name because the initial step in the process is the formation of an emulsion of a liquid *monomer* in water. A *monomer* is the building block of a polymer; it usually has a carbon-carbon double bond and usually is in the form  $H_2C=CHXY$ .  $X$  and  $Y$  can be variety of constituents. One end of a monomer is usually  $CH_2$  for steric reasons. The *initiator* (the chemical which initiates the reaction by breaking the double bond) would not be able to reach the double bond, if  $CH_2$  were not at one of the two ends of the monomer. One simple monomer is *Ethylene*,  $H_2C=CH_2$ . It polymerizes to form polyethylene (the process of polymerizing ethylene is not an easy one). Note that, the above kind of molecule polymerizes as a linear chain. Molecules that have two carbon-carbon double bonds are named *crosslinkers*. These molecules can make branches if they are polymerized with monomers. Crosslinkers are usually added to monomers at a small percentage (about 1%). Figure 6.1 shows some common monomers we use in our lab.

### 6.1.1 Free Radical Polymerization

The radical that starts the polymerization is called the *initiator*. Some common water soluble initiators are hydrogen peroxide, potassium persulfate, ammonium persulfate and

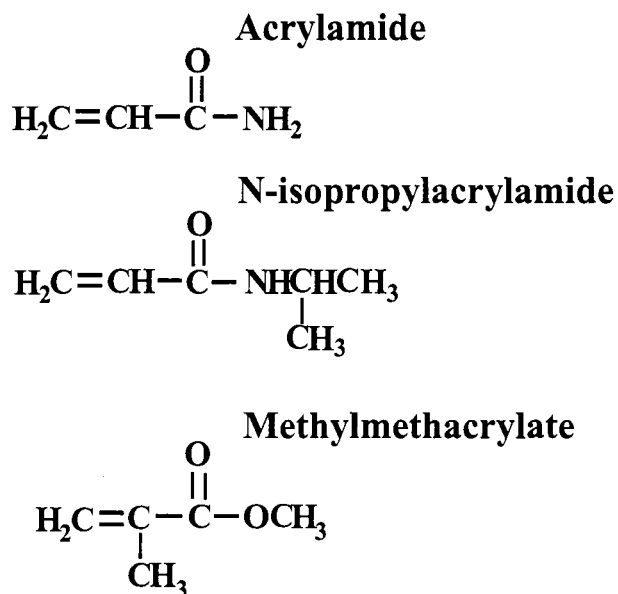


Figure 6.1: Some common monomer molecules.

sodium persulfate (Fig. 6.2). Examples of non-water soluble initiators are 2-2'-azo-bis-isobutylnitrile (AIBN) and benzoyl peroxide (Fig. 6.3). These molecules are split apart in an unusual way when heated. When they split, they split the pair of electrons in the bond that is broken. This is unusual because electrons like to be in pairs whenever possible. This behavior occurs because the molecule is symmetric and the bond in the middle is weak. After the split happens, two fragments are left, called initiator fragments. Each fragment has one unpaired electron. Molecules with unpaired electrons are called free radicals.

### 6.1.2 Polymerization In Emulsion Systems

Three basic steps occur in emulsion polymerization: initiation, propagation, and termination. The initiation step is depicted in Fig. 6.4. After the initiator dissociates, it combines with one of the monomer molecules and breaks the carbon-carbon double bond. Then the resultant molecule acts as a radical that is ready to combine with another monomer.

The propagation step is depicted in Fig. 6.5. Monomer molecules keep reacting with



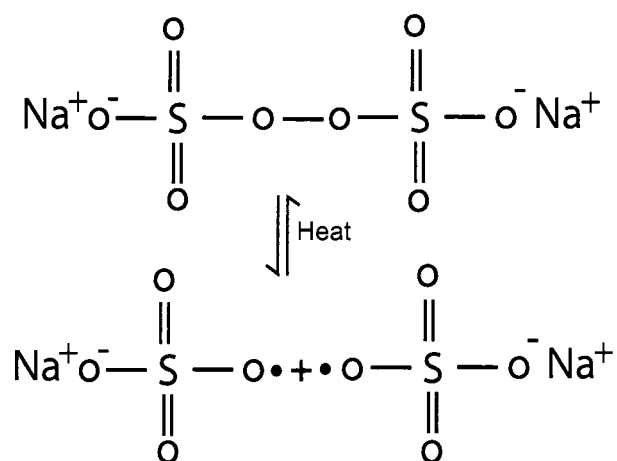


Figure 6.2: Dissociation of sodium persulfate upon heating.

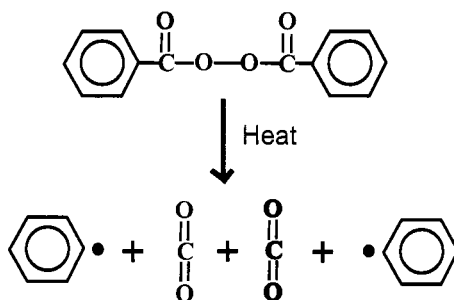


Figure 6.3: Dissociation of benzoyl peroxide upon heating.

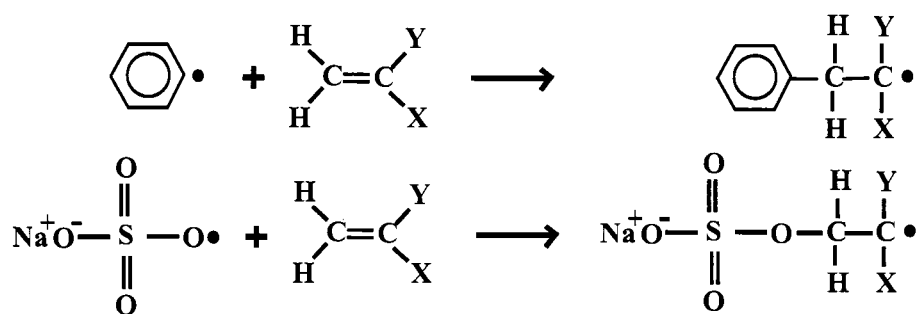


Figure 6.4: Initiation step of polymerization.

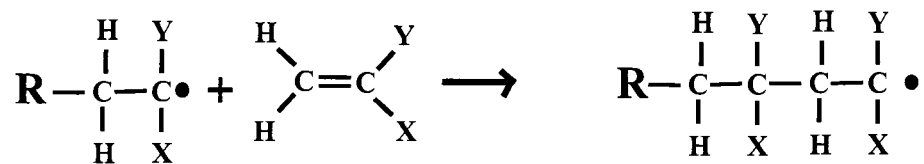


Figure 6.5: Propagation step of polymerization where molecular weight of the polymer increases.

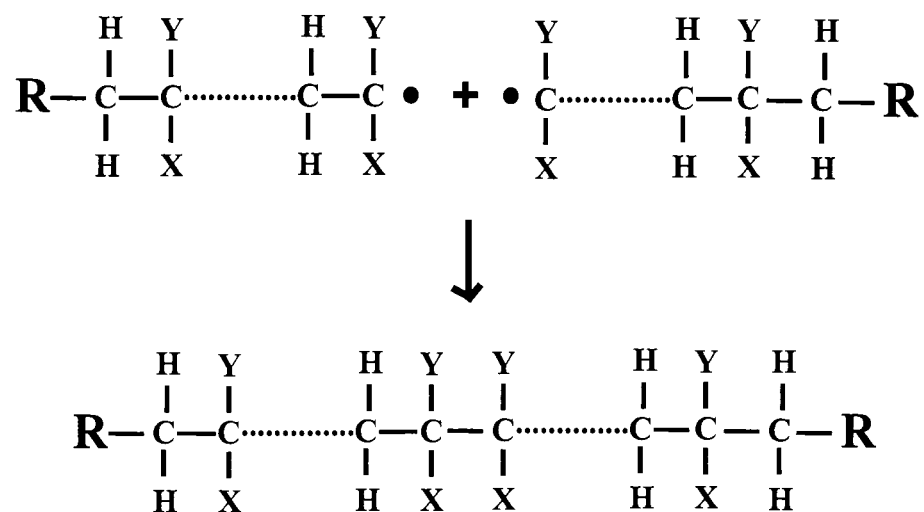


Figure 6.6: Termination step of polymerization where the reaction stops.

the free radical producing an increase in the molecular weight of the polymer. The last step is the termination, wherein two of these active molecules meet and react as shown in Fig. 6.6.

The resultant molecules are capped with “R” on both ends. In the case of using sodium persulfate (Fig. 6.2) as initiator, the resultant molecule will have charges on both ends. Water soluble initiators are used to synthesis aqueous colloidal particles. The surface “flavor” (type and strength of the charges) will depend on the type of the initiator. In the case of using benzoyl peroxide (Fig. 6.3) the resultant molecule will have no charge on either of its two ends.

### 6.1.3 Aqueous Colloidal Synthesis Using Emulsion Polymerization

The basic components for this synthesis are water (*continuous phase*), monomer (*dispersed phase*), surfactant, and initiator. The first three components are loaded into the reaction vessel and then heated up. Afterwards, a water soluble initiator is added. This early stage is depicted in Fig. 6.7. The monomer is in three locations at this step: in large emulsion droplets, in swollen micelles and dissolved in water at a very low concentration. The surfactant also occupies three positions: on the surfaces of large emulsion droplets, dissolved in water and in forming micelles. The initiator is only in water. Since the solution is at high temperature, the initiator will form radicals. Since the initiator is not soluble in the disperse phase (monomer), radicals will react only with the monomers that are dissolved in water. The reaction will then propagate (polymer chain increase in length). When the polymer chains reach a certain length, the polymer solubility in water decreases, and they enter the micelles, where propagation of the chains is continued.

Once the dissolved monomers leave the water, equilibrium is disturbed. More monomer leaves the big emulsion droplets, dissolves in water, polymerizes, and then reenters to micelles. In this way, emulsion droplets keep decreasing in size, while particles keep increasing in size until all of the emulsion droplets disappear. This scheme of controlled reaction produces monodisperse particles. The slower the reaction, the more uniform the particles that are produced. It's easier to synthesize uniform polystyrene particles compared to PMMA particles. The reason is that styrene has aromatic group that makes its solubility in water very low. This makes the polymerization process for styrene very slow (the batch takes about 18 hours). PMMA however has higher solubility in water than styrene, the polymerization process is relatively faster (about 2 hours) and the resultant particles are less uniform. In this method, if the initiator is soluble in the monomer, we will get very non-uniform particles with sizes ranging from a millimeter to few tens of nanometers.

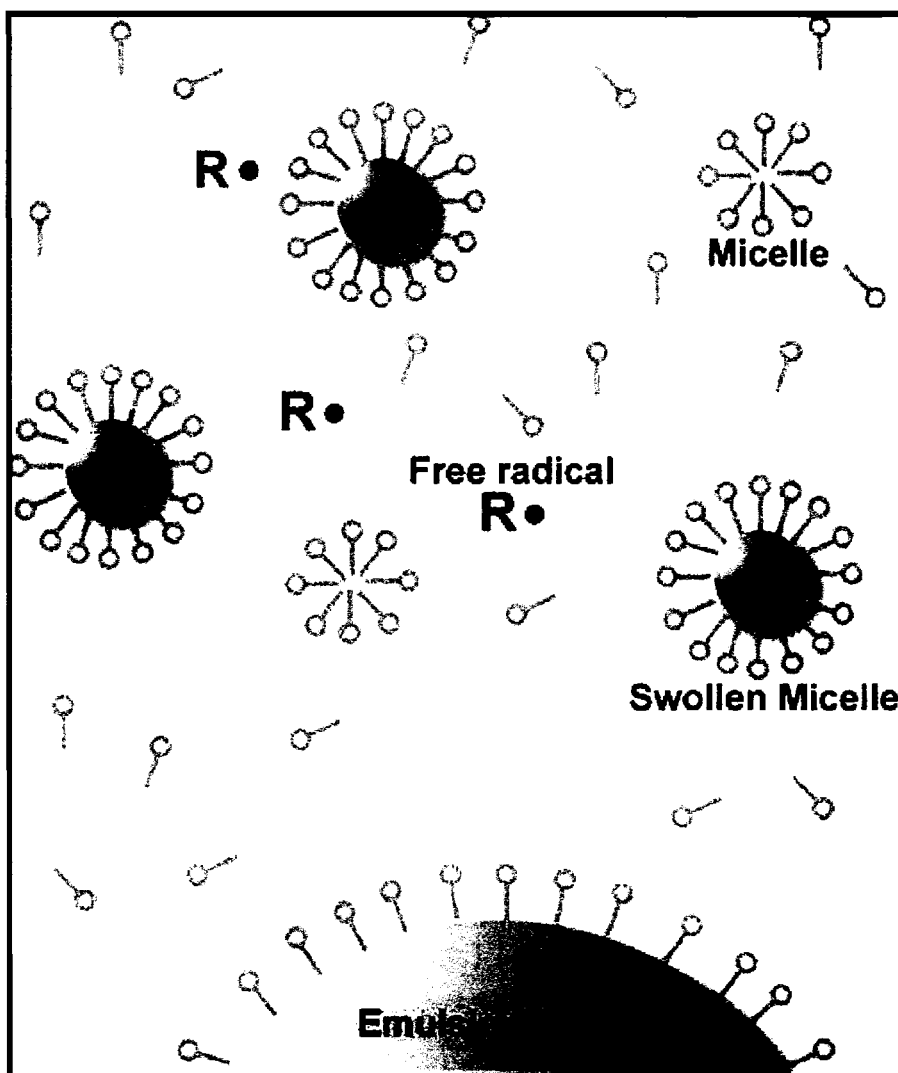


Figure 6.7: Diagram of emulsion polymerization system.

## 6.2 Synthesis of NIPA Particles

Poly(N-isopropylacrylamide) (PNIPAM) is a thermally sensitive polymer known to undergo a phase transition in water, from being hydrophilic to be hydrophobic, at the lower critical solution temperature (LCST) of  $\sim 32^\circ\text{C}$ . The structure of the unit monomer molecule is shown in Fig. 5.1. In our lab we use emulsion polymerization technique to synthesis colloidal particles made out of NIPA polymer. The setup is shown in Fig. 6.8.

In order to stain the particles with fluorophore that reacts with the amine group, we synthesis positively charged particles using 2,2'-azobis(2-methylpropionamidine) (azobis) as initiator, see Fig. 6.9. To have a brighter fluorophore, we increase the number of amine groups in each particles by copolymerizing NIPA with 2-aminoethylmethacrylate hydrochloride (AEMA), Fig. 6.10. An AEMA-NIPA copolymer is expected to have higher LCST temperature than pure NIPA ( $\sim 32^\circ\text{C}$ ) since AEMA is a hydrophilic monomer. We add AEMA in very small percentage in the AEMA-NIPA copolymer so that the LCST temperature is almost the same of that of the pure NIPA. Since we synthesis positively charged particles, we use a cationic surfactant, didodecyldimethylammonium bromide (DTAB), see Fig. 6.11. Finally, we crosslink the particles with methylene-bis-acrylamide (BIS). As was mentioned before the crosslinker must have two carbon-carbon double bonds, see Fig. 6.12.

The particles are then synthesized as follows. First, 25 mM of DTAB, 100 mg BIS (Polysciences, Inc.), 300 mg of (AEMA), 30 gm of NIPA (Polysciences, Inc.), and 100 mg of sodium chloride and 375 ml of 50 mM acetic acid buffer solution, pH=4.0, are loaded in a special four neck flask equipped with a stirrer, a reflux condenser, thermometer, and a gas inlet., see Fig. 6.8. The reason for adding sodium chloride is to screen the particle surface charges; this ends up producing bigger particles. The resultant mixture is stirred, heated to  $70^\circ\text{C}$ , and bubbled with dry nitrogen for 10 minutes to remove dissolved oxygen. Dissolved oxygen would react with the initiator and oxidize it. A solution of 500 mg of 2,2'-azobis(2-methylpropionamidine) dissolved in 10 ml of deionized water is then

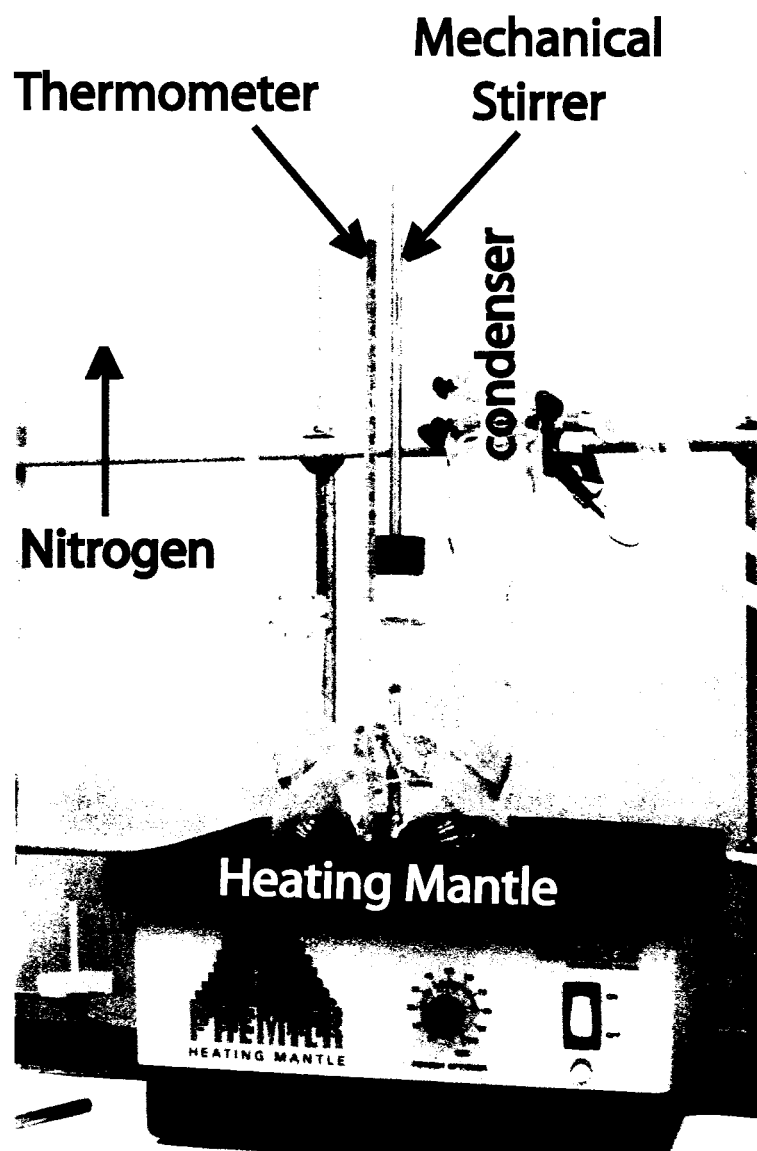


Figure 6.8: NIPA particles synthesizing setup.

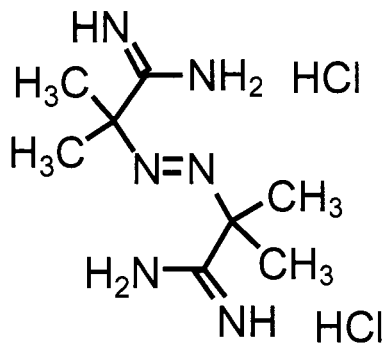


Figure 6.9: 2,2'-azobis(2-methylpropionamidine) (azobis) molecule.

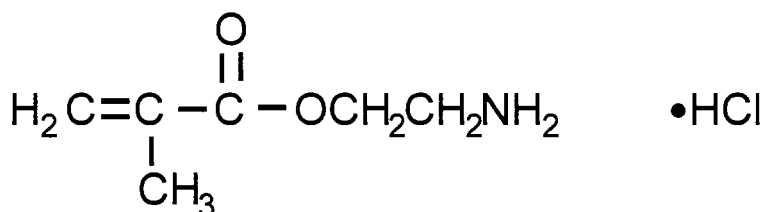


Figure 6.10: 2-aminoethylmethacrylate hydrochloride (AEMA) molecule.

added to the mixture to start the polymerization reaction. The mixture is continuously stirred at 70 °C for four hours, and then allowed to cool down to room temperature.

The resultant particles are centrifuged down and re-suspended in a different buffer solution (pH=8.3, 0.1 M sodium bicarbonate) to allow the amine groups to react with a fluorophore, 5-(6)-carboxytetramethylrhodamine, succinimidyl ester (TAMRA). 10 mg of TAMRA is dissolved in 300  $\mu$ l of dimethylsulfoxide (DMSO) and then added slowly to 40 ml of particle solution. The solution is then stirred gently for 24 hours to allow the reaction of the fluorophore.

Finally the particles are then cleaned cyclically, first concentrating them by centrifugation and then re-suspending them in a buffer solution (pH=4.0, 20 mM acetic acid). In order to minimize particle aggregates, the suspensions are centrifuged for a few minutes, the supernatant is collected and the process is repeated (approximately ten times). For temperatures below 32°C, NIPA solubility increases with decreasing temperature. Consequently the NIPA-AEMA particle diameter varies in our experimental temperature

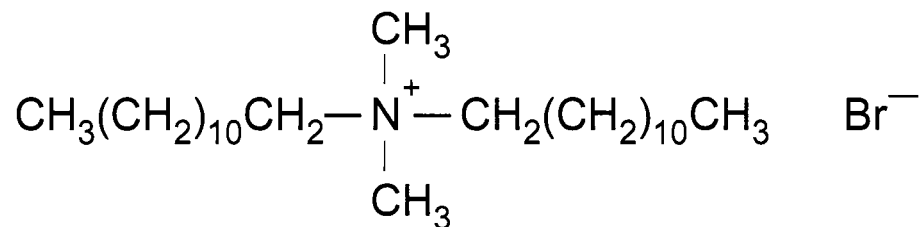


Figure 6.11: Didodecyldimethylammonium bromide (DTAB) molecule.

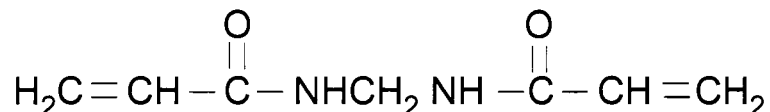


Figure 6.12: Methylene-bis-acrylamide (BIS) molecule.

regime (20-28°C) as a result of water moving into and out of the microgel.

The particles made from NIPA-AEMA copolymer have higher surface charge and are more stable against aggregation in solution during processing than particles made from pure NIPA. Counter ions in the buffer solution ensure the charges on the particles are screened. In addition, the polymerization rate in our acidic solutions (pH 4.0) was slow, resulting in reduced size polydispersity. Dynamic light scattering measurements at 25 °C determine the particle radius to be ~375 nm with a polydispersity of less than 3%. Due to the screening of charges, microgel particles with TAMRA are slightly smaller in size than non-stained particles, but the presence or absence of TAMRA does not change the particle phase behavior.

### 6.3 Synthesis of NIPA Polymer

Poly(N-isopropylacrylamide) polymer was synthesized at 22°C by free radical polymerization of N-isopropylacrylamide (750 mg) dissolved in 10 ml of 20mM (pH=7.0) Tris buffer. Dried nitrogen was bubbled into the monomer/solvent mixtures for 10 min to remove the dissolved oxygen. Ammonium persulfate (6 mg) and tetramethylenediamine



(TEMED) (28 ml) were added as initiator and accelerator. The mixture was left overnight to be polymerized [216].

## 6.4 Dynamic Light Scattering

Dynamic light scattering (DLS) is a powerful technique to measure the size distribution of particles dispersed in solution [13, 28]. An average ensemble can be obtained by just performing one experimental run. Using this technique, a broad range of particle sizes can be measured, from micelles a few nanometers in radius to colloidal particles a few microns in radius. Dynamic light scattering is based on the random Brownian motion of suspended particles in solution. When spatially coherent light scatters off the suspended particles, the far-field intensity will fluctuate. For a very dilute suspension of particles, photons are scattered at most once by the sample. The particles diffuse randomly with diffusion constants that depend on the size of the particles. Smaller particles diffuse faster than bigger ones. The intensity due to scattering from small particles fluctuates in time more rapidly than the scattered intensity of the bigger particles. Since the scatterers move randomly, on a long time scales these fluctuations are uncorrelated. The scattered intensity at two closely spaced times, however, is correlated. From the intensity-intensity temporal auto correlation function one can get a useful information about particle sizes and size distribution.

The dynamic light scattering setup is shown in Fig. 6.13. A laser beam provides the coherent light source. The incident beam has a wave vector  $\vec{K}_{in}$ , the scattered beam has a wave vector  $\vec{K}_{out}$ , and the momentum transfer or scattering vector  $\vec{q} = \vec{K}_{out} - \vec{K}_{in}$  has the magnitude,

$$q = \frac{4\pi n_o \sin(\frac{\theta}{2})}{\lambda_o}. \quad (6.1)$$

The intensity autocorrelation function measured from scattered light is:

$$G^{(2)}(\tau) = \langle I(0)I(\tau) \rangle = \langle |E(0)|^2 |E(\tau)|^2 \rangle = \lim_{T \rightarrow \infty} \left( \frac{1}{2T} \right) \int_{-T}^{+T} I(t)I(t+\tau)dt. \quad (6.2)$$

The capital  $G$  denotes an unnormalized measured quantity from the DLS instrument, sometimes called  $C(\tau)$ . The superscript 2 indicates that it is related to the light intensity  $I$  and not to the electric field  $\vec{E}$ . This second order autocorrelation function is usually related to the normalized electric field correlation function  $g^{(1)}(\tau) = \langle |E|^2 \rangle$  by the Siegert relation as:

$$G^{(2)}(\tau) = B \cdot (1 + f^2 |g^{(1)}(\tau)|^2), \quad (6.3)$$

where  $\tau$  is the delay time,  $B$  is the baseline, we measure it as  $\tau \rightarrow \infty$  and  $f$  is an instrumental parameter related to the coherence properties of the laser beam. For a suspension of monodisperse colloidal particles,

$$|g^{(1)}(\tau)| = \exp(-\Gamma \cdot \tau), \quad (6.4)$$

where  $\Gamma$  is called the decay or relaxation rate. For a dilute particle suspension,  $\Gamma$  depends on the random diffusion of particles,

$$\Gamma = D \cdot q^2, \quad (6.5)$$

where  $q$  is scattering wave vector, eqn. 6.1, and  $D$  is the diffusion coefficient that is given (in this simple case) by Stokes-Einstein relation,

$$D = \frac{k_B T}{6\pi\eta R_h}. \quad (6.6)$$

Here  $k_B$  is the Boltzmann's constant,  $T$  is the absolute temperature,  $\eta$  is the viscosity of the liquid and  $R_h$  is called the "hydrodynamic" radius of the particle. For most rigid particles, the hydrodynamic radius is very close to the physical particle radius. The equation 6.4 is valid strictly speaking for monodisperse particles only. For polydisperse

particle suspensions the instrument detects multiple decays. The best method for analyzing the signal of polydisperse particles is proposed by Koppel, [115]. A continuous distribution of decay constant  $\Gamma$  yields a  $g^1(\tau)$  function that is weighted as,

$$|g^{(1)}(\tau)| = \int_0^\infty P(\Gamma) \exp(-\Gamma \cdot \tau) d\Gamma. \quad (6.7)$$

where  $P(\Gamma)$  is the distribution of the decay constant and,

$$\int_0^\infty P(\Gamma) d\Gamma = 1. \quad (6.8)$$

Expanding eqn. 6.7 about an average value and integrating we get,

$$|g^{(1)}(\tau)| = \exp(-\bar{\Gamma}\tau) \cdot [1 + \frac{\mu_2}{2!} \cdot \tau^2 - \frac{\mu_3}{3!} \cdot \tau^3 + \frac{\mu_4}{4!} \cdot \tau^4 + \dots], \quad (6.9)$$

where  $\bar{\Gamma}$  is the average decay constant,

$$\bar{\Gamma} = \int_0^\infty \Gamma \cdot P(\Gamma) d\Gamma, \quad (6.10)$$

and  $\mu_n$  is its  $n^{th}$  moment,

$$\mu_n = \int_0^\infty (\Gamma - \bar{\Gamma})^n \cdot P(\Gamma) d\Gamma \quad .. \quad (6.11)$$

Taking the logarithm of eqn. 6.9 and expanding in a Taylor series we get,

$$\ln[f|g^{(1)}(\tau)|] = \ln(f) - \bar{\Gamma} \cdot \tau + \frac{\mu_2}{2!} \cdot \tau^2 - \frac{\mu_3}{3!} \cdot \tau^3 + \frac{\mu_4 - 3\mu_2^2}{4!} \cdot \tau^4 + \dots \quad (6.12)$$

Here, the coefficients of  $\tau^n$  are the cumulants where the first three terms are just the simple moments.

We measure  $G^{(2)}(\tau)$ . For monodisperse particle suspensions the decay constant is calculated from:

$$\frac{1}{2} \ln\left(\frac{G^{(2)}(\tau) - B}{B}\right) = \ln(f) - \Gamma \cdot \tau \quad (6.13)$$

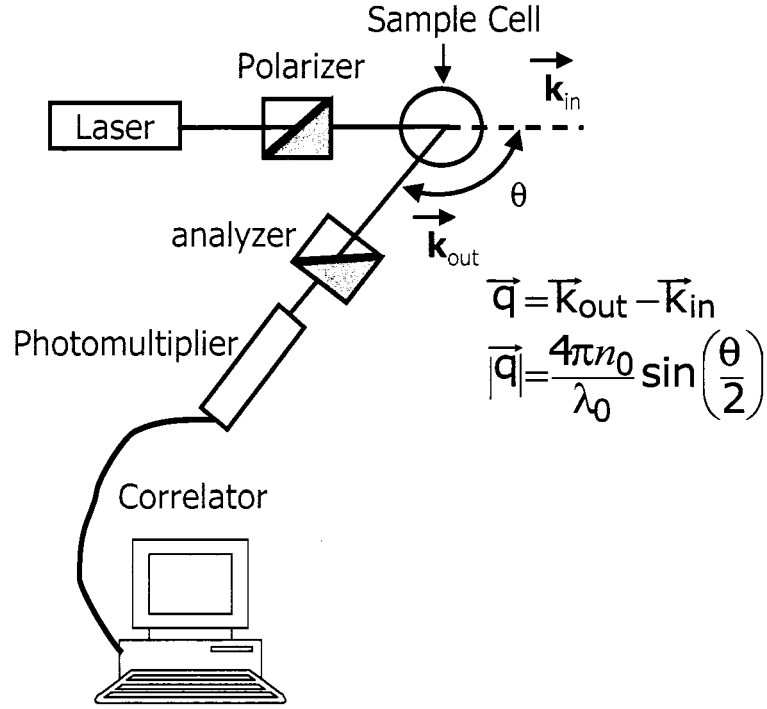


Figure 6.13: Dynamic light scattering setup.

For polydisperse suspension, the average decay constant and the size distribution can be calculated as follows.

$$\frac{1}{2} \ln\left(\frac{G^{(2)}(\tau) - B}{B}\right) = \ln(f) - \bar{\Gamma} \cdot \tau + \frac{\mu_2}{2!} \cdot \tau^2 - \frac{\mu_3}{3!} \cdot \tau^3 + \frac{\mu_4 - 3\mu_2^2}{4!} \cdot \tau^4 + \dots \quad (6.14)$$

The size and the size distribution is obtained by fitting  $0.5 \ln\left(\frac{G^{(2)}(\tau) - B}{B}\right)$  to a polynomial, from which particle radius is obtained from  $\bar{\Gamma}$  and the polydispersity is obtained from  $\mu_2$  (the variance of  $\Gamma$ ). To first approximation, the variance of the radius distribution is equal to the variance of  $\Gamma$ . This is only correct if the radius distribution is narrow, i.e.  $\Delta R/R \leq 0.30$ . By fitting the data obtained from DLS to eqn. 6.14 one gets the polydispersity of the particle radius, i.e.

$$Poly = \frac{\mu_2}{\bar{\Gamma}^2}. \quad (6.15)$$

A typical decay of autocorrelation function for NIPA particles at 20 °C is shown in Fig. 6.14. The baseline is calculated from the last three points at  $\sim 2 \times 10^6 \mu\text{sec}$ . Figure

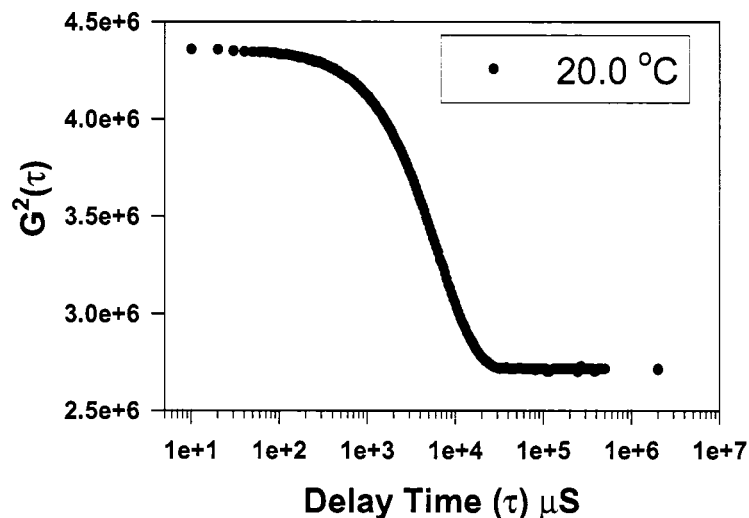


Figure 6.14: The decay of the intensity autocorrelation function with time for NIPA particles at 20 °C.

6.15 shows  $0.5 \ln\left(\frac{G^{(2)}(\tau) - B}{B}\right)$  as a function of time for NIPA particles at two temperatures, 20 °C and 31.4 °C. The data are nearly perfectly fit with a polynomial of first, second, third, and fourth degrees. Values of  $\Gamma$ ,  $\mu_2$ , diameter, polydispersity, and  $f$  are tabulated in Table 6.4. The intersection of the curve in Fig. 6.15 with the  $y$  axis is just  $\ln(f)$  (eqn. 6.14).  $f$  is a number between 0 and 1 that depends on the degree of coherence of the laser beam. Here the value is about 0.78 which is reasonably good. The polydispersity of our particles is less than 3.0 percent.

Figure 6.16 shows high volume fraction of NIPA particles loaded into a tube. The color is due to Bragg diffracted peak from the colloidal crystal. The homogeneity of the color indicates that the particles are crystalized in large domains. To measure the polydispersity using DLS accurately, one needs more and smooth data on long time scales, in the decay region close to the baseline, see Fig. 6.14. To achieve that, a clean sample, a clean oil bath and longer integration is needed. Typical measurements were taken approximately every 0.5 °C in the temperature range 20-50 °C. The hydrodynamic diameter as a function of temperature is shown in Fig. 6.17.

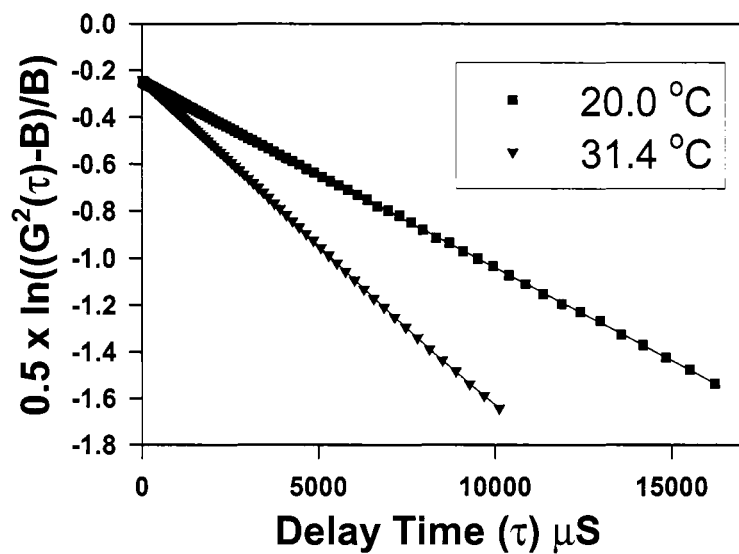


Figure 6.15: Autocorrelation function as a function of time for NIPA particles at 20°C and 31.4°C.

Table 6.1: Diameter ( $D$ ) and polydispersity (Poly.) of NIPA particles at two different temperatures

Temp.	Fit	$\Gamma$ ( $\mu\text{S}^{-1}$ )	$\mu_2$ ( $\mu\text{S}^{-2}$ )	$D$ (nm)	Poly.	f
20.0°C	Linear	7.92E-05		852		0.7799
	Quadratic	7.94E-05	1.70E-11	848	0.0027	0.7801
	Cubic	8.02E-05	2.11E-10	839	0.037	0.7806
	Quartic	8.01E-05	1.16E-10	840	0.018	0.7805
31.4°C	Linear	1.41E-04		646		0.7878
	Quadratic	1.41E-04	2.98E-10	646	0.015	0.7890
	Cubic	1.40E-04	2.35E-10	650	0.012	0.7876
	Quartic	1.41E-04	2.49E-10	646	0.018	0.7882

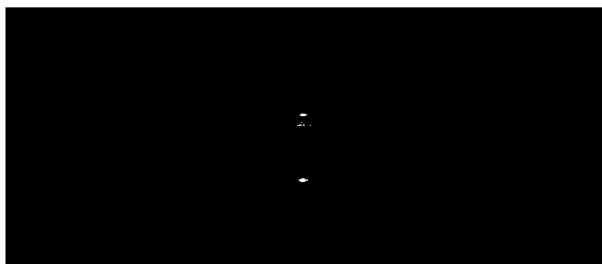


Figure 6.16: Glass chamber containing NIPA particle suspension at high volume fraction. The color indicates that the suspension is in crystalline phase.

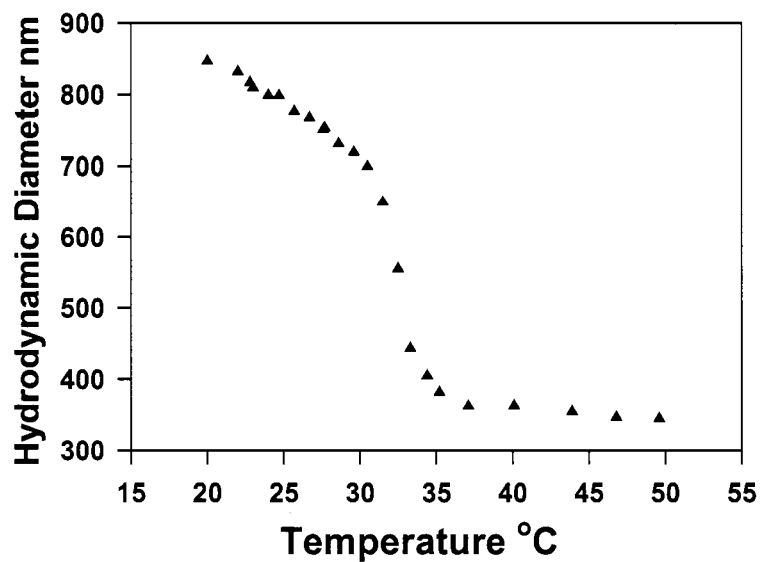


Figure 6.17: Hydrodynamic diameter of NIPA particles as a function of temperature. NIPA particle radius undergoes first order transition at about 32.0°C.

## 6.5 Preparation of the Filamentous Bacteriophage *fd*

Bacteriophage *fd* is a negatively charged monodisperse semi-flexible rod with diameter of 6.6 nm, contour length of 880 nm, and persistence length between 1000 nm and 2200 nm [61, 123]. It forms isotropic, cholesteric(nematic) and smectic phases with increasing concentration [59]. A standard protocol was used to grow *fd* virus [61].

### 6.5.1 Colonize Bacteria in Hard Media

The first step for growing *fd* virus is to grow bacteria that *fd* will infect. We use *Escherichia coli* (E-coli), JM101 strain, as host bacteria. To prevent growth of wild type *fd* virus, we grow the host bacteria in three steps. These steps insure limited generations of bacteria will be grown. The first step is to colonize bacteria on agar plate. We prepare the agar plates as follows. We dissolve 10.0 gm of tryptone, 5.0 gm of yeast extract and 7.5 gm of sodium chloride in 1 liter of distilled water. We call this mixture *liquid media*. We add 15 gm of agar to the *liquid media*, autoclave (sterilizing using heat and pressure) the solution, and pour it onto sterilized plates before it cools to room temperature. When it cools to room temperature the agar will gel. We then make similar preparation but with an added 8 gm agar to the *liquid media* instead. We then pour this mixture on the top of the previous one. The thickness of the bottom layer is about 5 mm, while the thickness of the top layer is about 2 mm. The top layer is soft enough to enable bacteria to grow in it.

We then streak the agar plates with a rod infected with E-coli bacteria. To infect a rod with bacteria we simply dip an autoclaved glass rod in a bacterial solution (the long term stored one at -80 °C). After streaking the agar plates, we incubate them overnight at 37°C. This is the first step for growing the E-coli bacteria.



### 6.5.2 Large Scale Bacterial and *fd* Growth

The second step is to take a single isolated colony and grow it in a small volume of *liquid media*. We take a single isolated colony from the agar plate and disperse it in 5 ml of autoclaved *liquid media* and let the bacteria to grow overnight by shaking the solution at 37 °C. The third step is to infect a large volume of *liquid media* using the small volume already infected. We typically add 1 ml of infected *liquid media* to 1 L of the autoclaved one and shake it overnight at 37 °C. We then infect the E-coli bacteria by *fd* virus. We add 200  $\mu$ L of 1 mg/ml *fd* virus to each 1 L of bacterial solution. We then shake it for 6 hours at 37 °C. All bacterial growth in solutions are done in Erlenmeyer flasks with a foil cap. The flasks are only filled to one third of its volume in order to insure that bacteria will get enough oxygen. In our lab we use New Brunswick shaker/incubator that can shake up to 6 x 4 L Erlenmeyer flasks. This enables us to grow 8 L in each run. Our yield is about 40 mg of *fd* per liter of infected bacterial.

### 6.5.3 Isolating *fd* virus from Bacteria

We spin the infected solution at 10,000 revolutions per minute (rpm) for 10 minutes using Sorvall GS-3 rotor with 6 tubes containing 500 ml each. The cell pellet is then discarded (after properly disinfected) and the supernatant is collected, this is the phage (virus) solution. We add appropriate amount of sodium chloride to adjust the ionic strength to 500 mM. We also add 20 gm of PEG (polyethylene glycol) to each 1000 ml of the phage solution. The purpose of adding sodium chloride is to screen the *fd* surface charge and the purpose of adding PEG is to deplete *fd*. We then spin the phage solution at 10,000 rpm for 20 minutes. The supernatant is discarded and the pellets are resuspended in about 2 ml of 20 mM Tris, pH 8.2.

#### 6.5.4 Purifying *fd* virus

We spin the phage solution at 20,000 rpm for 5 minutes using Beckmann 70Ti rotor to clean the solution from remaining bacteria. The supernatant is collected and the pellets are discarded. We then spin the phage solution at 45 K for 4 hours. The supernatant is discarded and the pellets are resuspended in 20 mM Tris, pH 8.2 buffer solution. The above steps are repeated few times until the pellet become clean. The pellet then resuspended in desired buffer solution and might dialyzed against it.

#### 6.5.5 Determining *fd* concentration

We use UV absorbance to determine the phage concentration. We first dilute the sample about 500 times. we determine *fd* concentration from UV absorbance at 272 nm from the following relation

$$conc. = \frac{Abs \times dilution \times pathlength}{3.84} \quad (6.16)$$

# Chapter 7

## Video Microscopy

### 7.1 Optical Microscopes

The main tool in our study of melting of colloidal systems is the optical microscope. The microscope along with the CCD camera enable us to follow the structure evolution of colloidal systems in real space and time. Other standard methods such as Bragg scattering are reciprocal or Fourier space techniques. Thus a comparatively unique feature of video microscopy is that it enables us to follow individual particle dynamics instead of ensemble average of many of the particles.

I'll explain briefly how modern microscopes work. The simplest microscope is composed of two lenses, see Fig 7.1(A). The first lens is the objective which has a short focal lens and the second one is the eyepiece which has a longer focal lens. The sample (object) is placed in a position further than the focal length from the objective (and less than twice the focal length). An inverted real image (intermediate image) of the sample is formed by objective, see Fig 7.1(A). The eyepiece then forms a virtual inverted image of this "intermediate image". This image cannot be projected unless we put another lens such as the eye lens which projects it onto the retina. A more advanced microscope uses so-called infinity-corrected optics. The object in this case is placed at the focal length of

the objective. The first “intermediate” image is then formed at infinity. A tube lens is then used to form a second “intermediate” image, Fig 7.1(B). This scheme allows extra optical components such as prisms and polarizers to be introduced between the objective and the tube lens without image distortion. This is because rays from the specimen pass through the added components parallel to the optic axis. Nowadays, most modern designs of microscopes have moved to infinity-corrected optics.

Originally microscopes were hampered by optical aberration, blurred images, and poor lens design. In 1886, Ernst Abbe designed the achromatic objective based for the first time on sound optical principles and lens design. These advanced objectives provided images with reduced spherical aberration and free of color distortions (chromatic aberration) at high numerical apertures. Several years later, in 1893, August Köhler reported a method of illumination, which he developed to optimize photomicrography, allowing microscopes to take full advantage of the resolving power of Abbe objectives. Early in the twentieth century the idea of infinity-corrected optics was introduced where the objective forms the intermediate image at infinity [16, 167, 102].

Köhler illumination is shown in Fig. 7.2 [16]. Separate paths are taken by the light rays that illuminate the specimen and the image forming light rays. The right-hand diagram shows the ray paths of illuminating light produce a focused image of the lamp filament at the plane of the substage condenser aperture diaphragm, the rear focal plane of the objective, and the eye lens. These areas in common focus are often referred to as conjugate planes. The left-hand diagram shows conjugate planes in the image-forming light path, they are the field diaphragm, the focused specimen, the intermediate image plane (i.e., the plane of the diaphragm of the eyepiece), and the retina of the eye or the film plane of the camera.

In Köhler design the illumination is designed so that an enlarged and focused image of the lamp filament is projected onto the plane of the condenser diaphragm. Closing or opening the condenser diaphragm controls the angle of the light rays emerging from the condenser and reaching the specimen from all azimuths. Because the light source is not

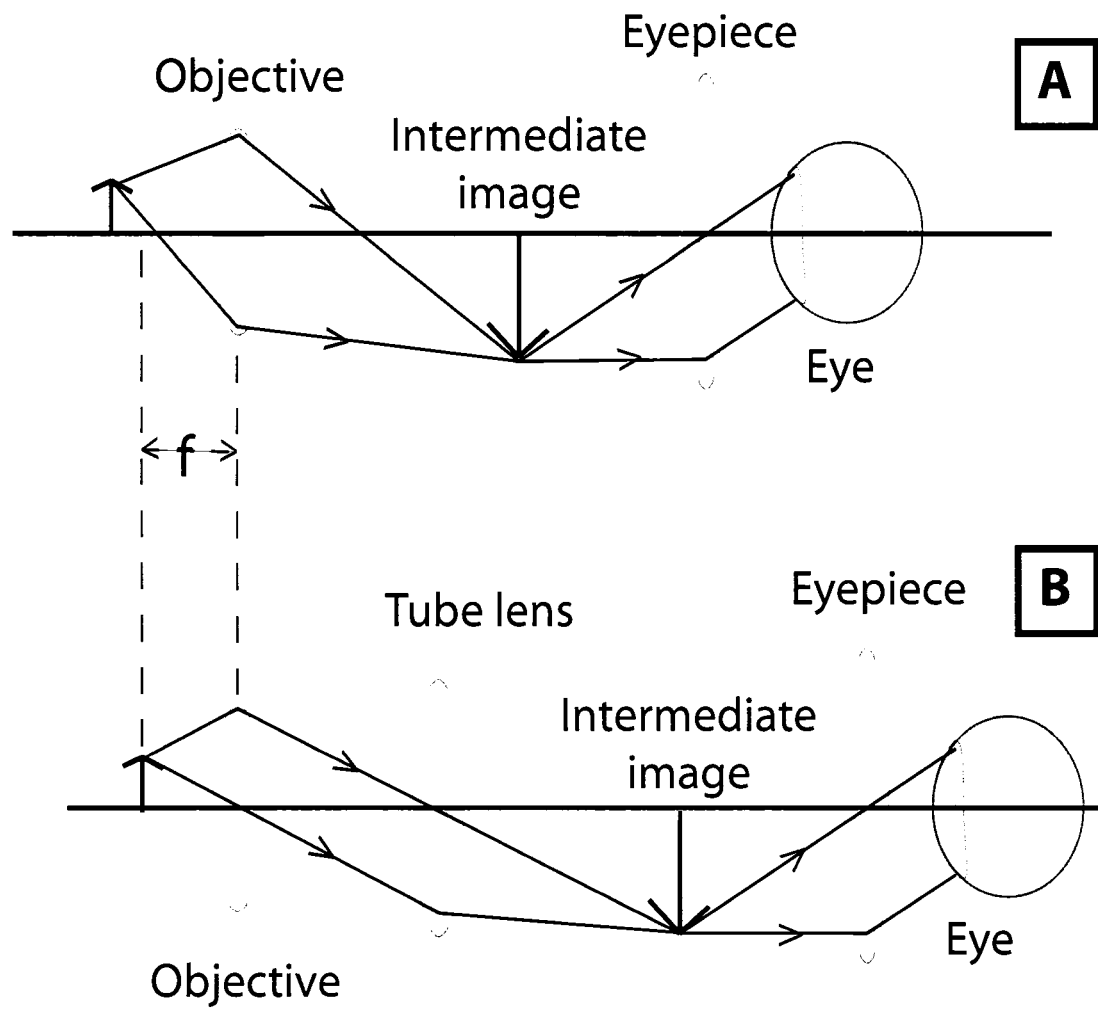


Figure 7.1: (A) Simple microscope composes of two lenses, (B) infinity-corrected microscope where the objective forms the image at infinity.

focused at the level of the specimen, illumination at specimen level is essentially grainless and extended, and does not suffer deterioration from dust and imperfections on the glass surfaces of the condenser. The opening size of the condenser aperture diaphragm, along with the aperture of the objective, determines the realized numerical aperture of the microscope system. As the condenser diaphragm is opened, the working numerical aperture of the microscope increases, resulting in greater light transmittance and resolving power. Parallel light rays that pass through and illuminate the specimen are brought to focus at the rear focal plane of the objective, where the image of the variable condenser aperture diaphragm and the light source are observed in focus simultaneously.

When light from the microscope lamp passes through the condenser and then through the specimen, some of the light passes through the specimen undisturbed in its path. Such light is called direct light. On the other hand some of the light passing through the specimen is refracted, scattered, or diffracted when it encounters parts of the specimen. The direct and diffracted light keep travelling and interfere to form the intermediate image, see Fig. 7.2. The image of a spherical particle for example will be in the shape of what is so-called Airy disk. The shape and the intensity profile of Airy disk is shown in Fig 7.4(A). According to Ernst Abbe, the details of a specimen will be resolved better if the objective captures as much orders of the Airy profile as possible. This means higher numerical aperture objective will give sharper images. As the object gets smaller, the angle of the second order peak gets larger. This means smaller objects need higher numerical aperture objective. The minimum distance ( $d$ ) in the specimen that can be resolved is given by,

$$d = \frac{1.22\lambda_o}{NA_{obj} + NA_{cond}}, \quad (7.1)$$

where  $\lambda_o$  is the used light wavelength and  $NA_{obj}$  and  $NA_{cond}$  are the objective and condenser numerical apertures respectively. Numerical aperture of a lens is given by,

$$NA = n \sin \theta, \quad (7.2)$$

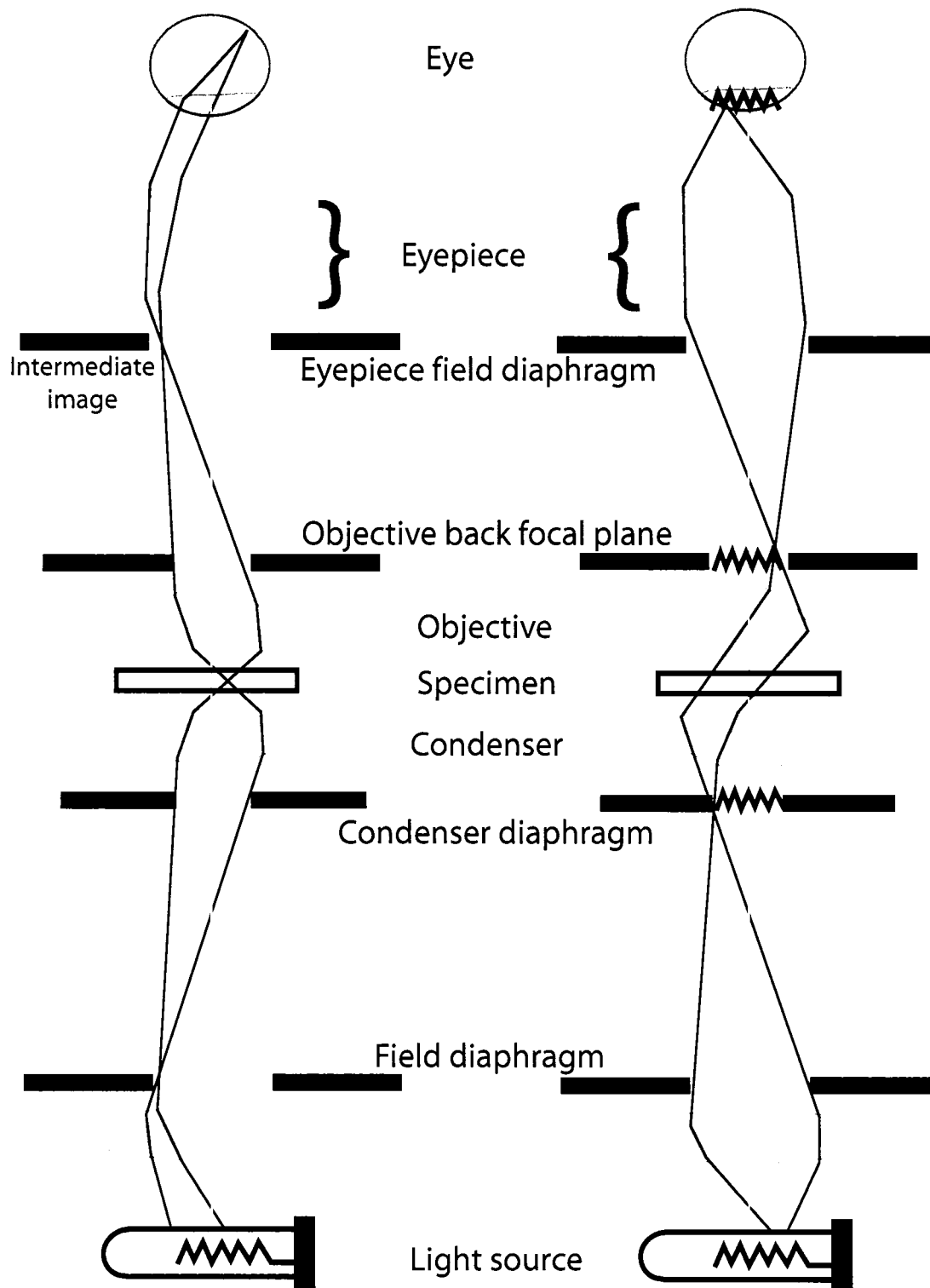


Figure 7.2: Image beam path (left) and illumination beam path (right) in Köhler illumination design.

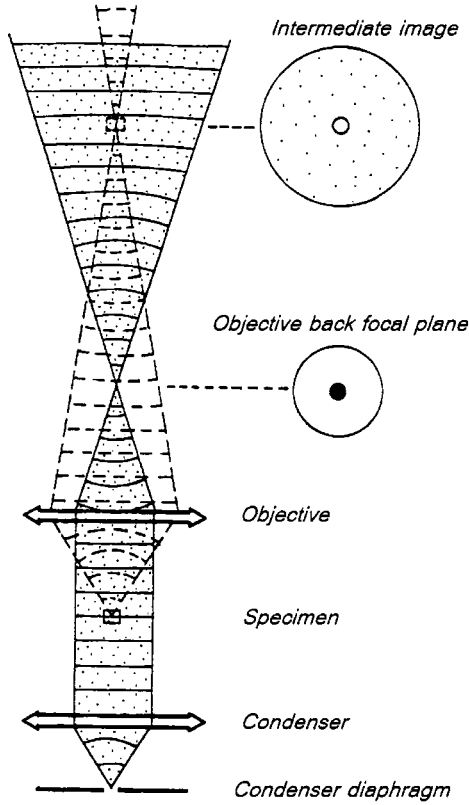


Figure 7.3: The interference of the direct light (from the light source) and the diffracted light (from the specimen) at the objective back focal plane and the intermediate image plane [102].

where  $n$  is refractive index of the medium between the lens and the object, and  $\theta$  is the maximum light angle that can be resolved by the lens.

## 7.2 Video Microscopy and Particle Tracking

Many experiments in our lab rely on accurately tracking the time evolved positions of individual probe particles. We use video microscopy to follow the dynamics of colloidal particles with a spatial resolution of 20 nm and temporal resolution of 30 Hz. The spatial resolution of a particle tracking experiment with video microscopy relies on the alignment of the microscope, the numerical aperture, and the magnification of the used objective, the



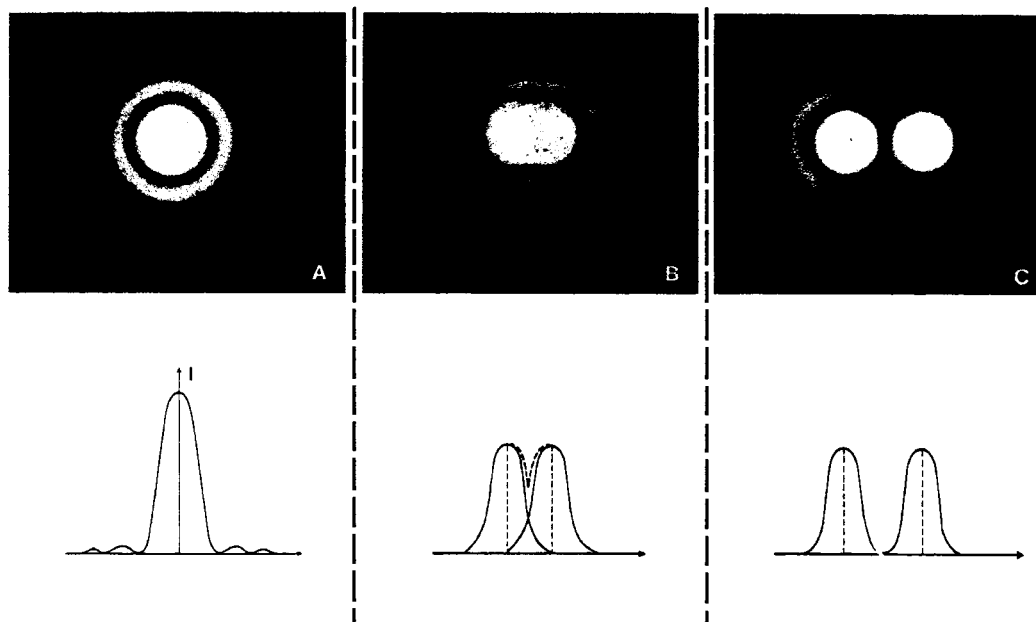


Figure 7.4: Airy disks and associated intensity profiles of one and two particles. Microscope resolving power is not strong enough to differ between the two particles in (B) [102].

resolution of the CCD camera and the software algorithms used to detect particle centers.

In the simplest setup an analog CCD camera (Hitachi) is attached to the optical microscope (Leica) and 480 x 640 pixel images are captured with a SVHS video cassette recorder at a rate of 30 images per second. The videotape of particle dynamics is then digitized by a computer equipped with a frame grabber card. Digital images are analyzed to determine the particle positions in each frame. For the 0.75 micron NIPA spheres, images are typically obtained with bright field microscopy using a 100x oil objective with numerical aperture equal to 1.45. This gives magnification of 128 nm/CCD pixel. Light microscopy resolution limits for the above adjustments is about two hundreds nanometers, based on eq. 7.1. Colloidal spheres larger than this resolution limit can be resolved directly with bright field microscopy.

In order for particle tracking algorithms to accurately determine particle centers, the number of pixels covered by the image of each particle must be four or more CCD pixels.

The colloidal particle position is observed as a circularly symmetric Gaussian image intensity profile centered at its geometrical center. In general, particle tracking routines are able to locate particle positions with sub-pixel accuracy. At a magnification of 100x (9 pixels/micron), sub-pixel accuracy corresponds to a spatial resolution of 20 nm, one order of magnitude better than the diffraction limited resolution [41]. The shutter speed of the CCD camera sets the exposure time,  $\tau$ , of a single image. If the exposure time is long enough to allow significant particle motion, the microscope image of the particle will not be circularly symmetric which results in a decreased ability of finding an accurate center. The shutter speed is set so that a particle of radius  $a$  embedded in a fluid diffuses less than the spatial resolution, 20 nm, in time  $\tau$ . The shutter speed in our experiment was adjusted to 1/500 to 1/2000 sec. Faster shutter speeds are feasible in our camera, however faster shutter speed requires higher light source intensity. In our experiment we tried to lower the light source intensity as much as possible, since it can increase the temperature of the sample cell, and our sample is temperature sensitive.

A spatial “bandpass filter” routine, written by Crocker and Grier [41], was applied to each image to suppress noise and correct for background brightness variations, see Fig. 7.5(B). Finally, the centers of brightness yield particles’ position with about 20 nm resolution. The spatial band pass filter also eliminates any image data in a band within one particle diameter of each border, see Fig. 7.5(B). Consequently, our algorithms do not detect particles within about a particle diameter from the image edges. We then run “feature” routine, written by Crocker and Grier [41], to locate each particle in each frame. The routine then gives output file contains a two dimensional array, the array has the particle number, time and x and y positions. From the output file we can calculate the mean square displacements and the pair correlation function  $g(r)$  in two dimensions (2D).

Because the particle tracking routines depend on variations of brightness over distances larger than the diffraction limited resolution, the numerical aperture of the objective does not affect the accuracy of center detection. However, a lower numerical aperture

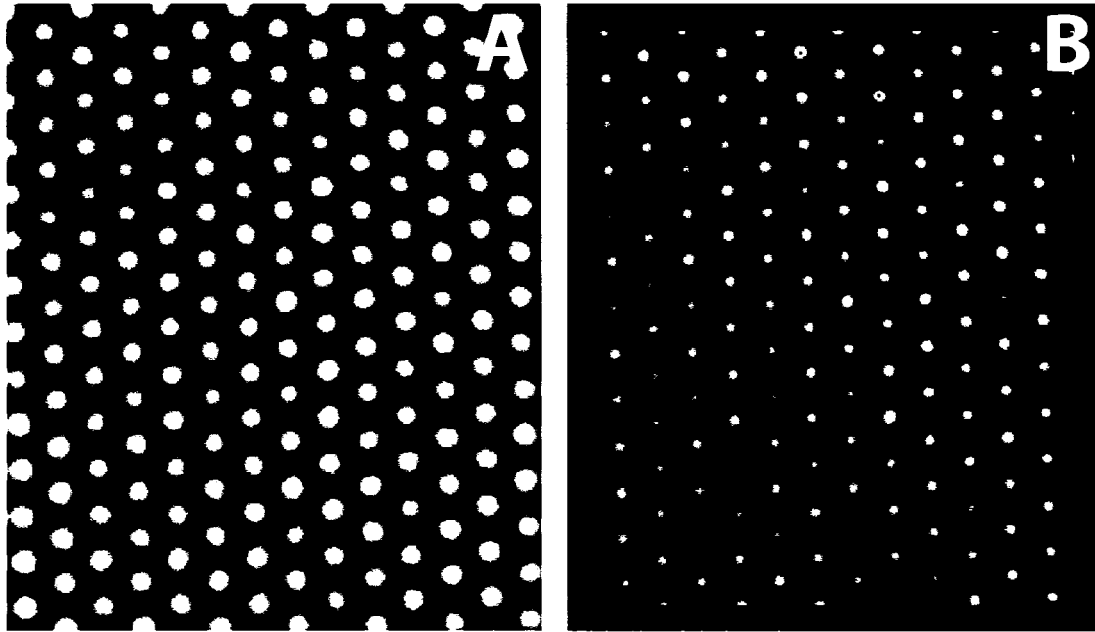


Figure 7.5: (A) Raw bright field image of NIPA crystal. (B) The image after a spatial bandpass filter was applied.

increases the depth of focus and projection error of particle motion perpendicular to the field of view increases.

# Chapter 8

## Premelting at Defects Within Bulk Colloidal Crystals

### 8.1 Introduction

The importance of melting in nature can hardly be overestimated, and yet a detailed understanding of the mechanisms that drive this transformation is still evolving. Scientists have speculated for more than a century about how crystalline solids melt [135, 49, 50], in the process generating microscopic models emphasizing the role of lattice vibrations [29, 128], dislocations [67, 26], grain boundaries [131, 40], surfaces [43, 173, 155, 133, 217], dimensionality [171], and combinations thereof. In contrast to the continuous transitions that arise in ferromagnetism and liquid-vapor systems, a first principle theory of the solid-liquid transition is difficult because of long-range many-body effects, symmetry, and a lack of universality. Furthermore, experimental investigations to test underlying theoretical assumptions are extraordinarily difficult, because they must track motions of individual atoms or defects within crystals.

Recent experiments [47, 77] and theory [215] have shown that atomic crystal surfaces, at equilibrium below the bulk melting point, often form melted layers. This is the

premelting, which is the localized loss of crystalline order at surfaces and defects for temperatures below the bulk melting transition. It can be thought of as the nucleation of the melting process. This premelting lowers the energy barrier for liquid nucleation and effectively prevents superheating of the solid [174, 47].

Many theories have suggested a similar premelting should occur at defects such as grain boundaries, stacking faults, and dislocations located within the bulk crystal, but these effects have not been observed. Simulations of grain boundaries [18, 172], for example, have found the free energy of the solid-solid interface can be larger than two solid-liquid interfaces, thereby favoring premelting near the grain boundary.

We image the motions of particles in three-dimensional crystals during the melting process. The crystals are equilibrium close-packed three-dimensional colloidal structures made from thermally responsive microgel particles. These particles are micron-size nearly-hard-sphere [199]. The thermal response of the microgel enables precision control of particle volume fraction. At high volume fraction these particles are driven entropically to condense into close-packed crystalline solids [234, 181], while at low volume fraction the particles are in liquid state. The diameters of the microgel particles depend on temperature [53, 227]. Thus by changing sample temperature slightly, we precisely vary the volume fraction of particles in the crystal over a significant range, driving the crystal from close-packing towards its melting point at lower volume fraction.

The images reveal premelting near grain boundaries and dislocations. Furthermore, particle tracking enables us to quantify the spatial extent of local particle fluctuations near a variety of defects as well as within the more ordered parts of the crystal. Increased disorder is observed in crystalline regions bordering the defects as a function of defect type (e.g. grain boundaries, dislocations, vacancies), distance from the defect, and particle volume fraction. These observations answer longstanding fundamental questions about melting mechanisms, suggest that grain boundary and dislocation premelting is an important effect in the melting process, and introduce new quantitative measures of local

disorder. Besides their intrinsic importance for colloid science and technology, all indications suggest interfacial free energy is the crucial parameter for premelting. Thus these results are also relevant for atomic scale materials.

## **8.2 Microscopy and temperature control**

Experimental observations were made using an upright microscope (Leica DMRXA2) equipped with a 12-bit monochrome cooled camera (QImaging RETIGA) and a motorized stage. The dimensions of the sample chamber were 18 x 4 x 0.1 mm. The temperature of the sample and objective lens (100 X 1.4 NA) were controlled to within 0.1 °C and were increased in 0.1 °C increments. Samples were left to equilibrate at each temperature for one hour. In order to track premelted regions and defects, we took bright field video images for 0.6 sec in 100 nm intervals throughout the  $\sim 100\ \mu\text{m}$  thick chamber. Because the microgel particles were  $\sim 95\%$  water, their refractive index was very close to that of water, allowing us to obtain high quality images throughout the sample volume. In order to track individual particle movement, we employed a video shutter time of 2 msec. Image fields were chosen to contain  $\sim 400$  particles, and particle positions were determined at resolutions much smaller than the particle radius or crystal lattice constant [41]. Fifteen minutes of video were recorded at each temperature.

## **8.3 Sample preparation**

The particle suspensions were loaded into the chamber using capillary forces at 28 °C, i.e. just below the melting temperature. In this process the suspension was sheared, this gave the crystal a preferential orientation. Initially we found that well oriented FCC crystals grew from the glass coverslip surfaces, and that the middle of the sample was fluid like. After loading we annealed the sample at 28 °C for 24 hours during which the samples

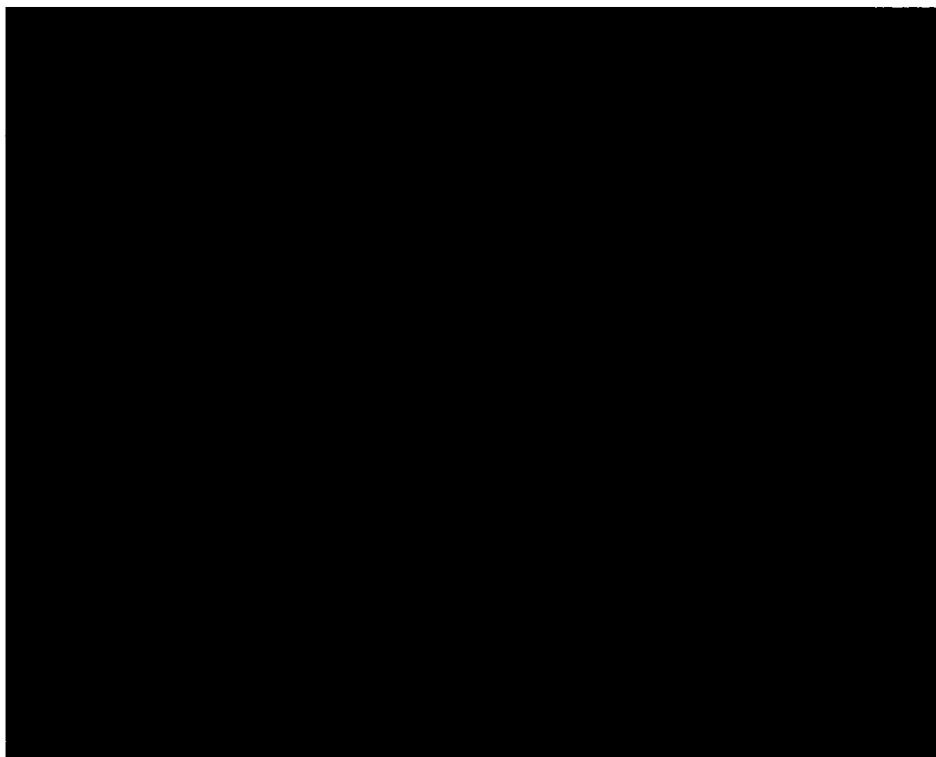


Figure 8.1: Bragg diffraction (wavelength = 405 nm) of 0.75  $\mu\text{m}$  diameter NIPA particle colloidal crystal.

crystallized. Bragg diffraction (Fig. 8.1) from various parts of the annealed sample, measured using the microscope with a Bertran lens, exhibited no detectable change in peak positions. The crystal had very few defects close to the glass walls, see Fig. 8.2. We never observed premelting near the walls; it is possible the walls stabilized the crystal or that the (111) planes near the wall surfaces are intrinsically stable [174]. Interior crystalline regions had many more defects, see Fig. 8.3. A few defects in the sample interior are shown in Figs. 8.10 and 8.14. Most of the defects we observed were stacking faults, which caused the formation of partial dislocations, Fig. 8.14 [91]. Typically the crystals lost their preferential orientation after melting and recrystallization, displaying large crystalline regions with different orientations separated by grain boundaries, Fig. 8.10.

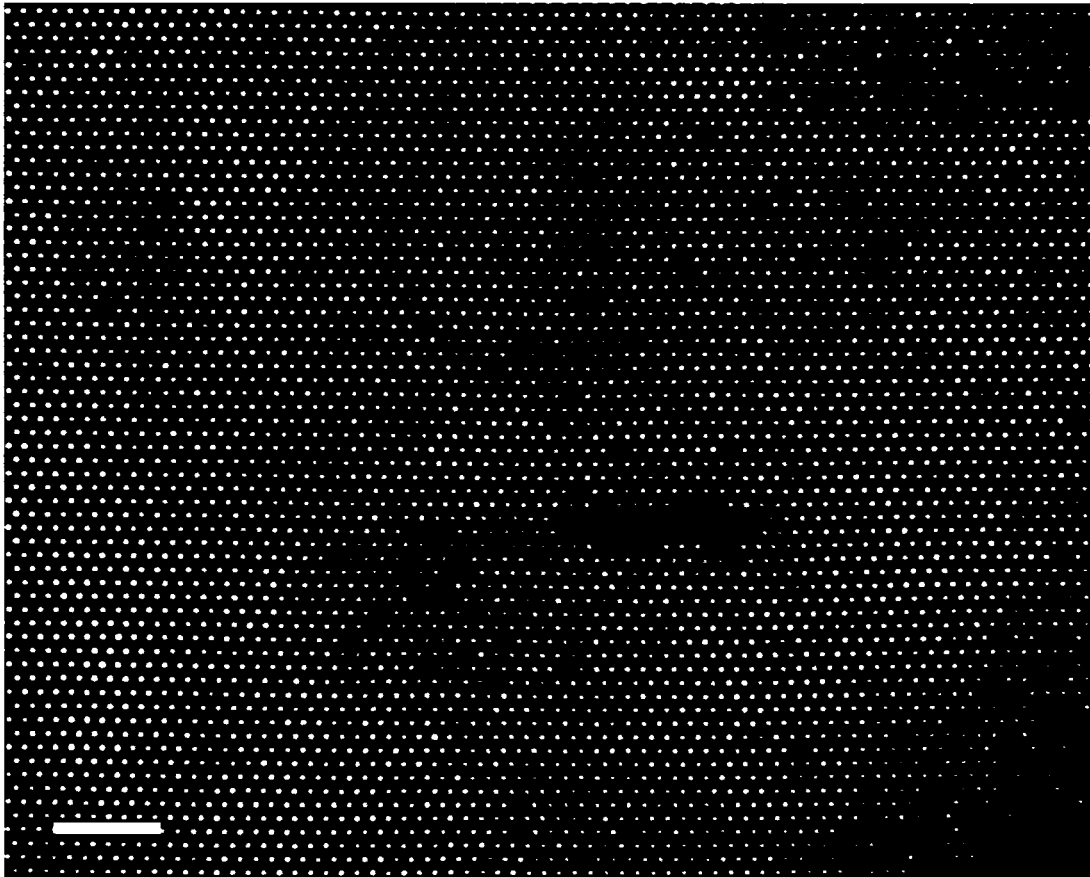


Figure 8.2: Bright field image of a layer in the NIPA particle colloidal crystal showing very few defects; the slice is of the 7th layer from the cover slip. Each bright spot corresponds to the central region of a  $0.75\ \mu\text{m}$  diameter particle.



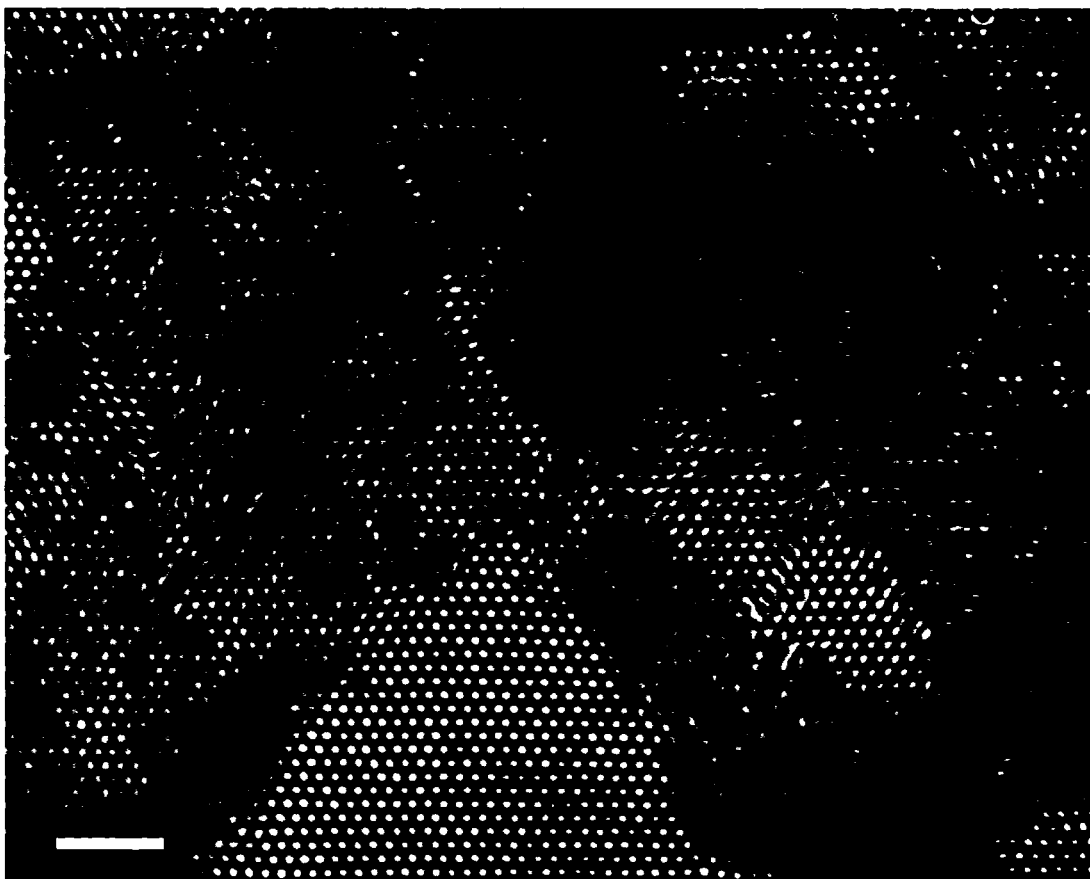


Figure 8.3: Bright field image of the NIPA particle colloidal crystal showing many defects (part of the image is in focus while the other part is out of focus) ; the slice is of the 15th layer from the cover slip. Due to sample preparation and annealing, the primary defects are partial dislocations that exist in the interior of the crystal. Scale bar is 5  $\mu\text{m}$ .

## 8.4 Positional fluctuations

Using the Lindemann parameter( $L$ ), a measure of the particle mean-square fluctuation, we have quantified melting observations as a function of sample temperature and volume fraction. Fig. 8.4 shows the time evolution of mean-square displacement (MSD) for particles in the bulk crystal at three different temperatures. On short time scales, the MSD exhibits free particle diffusion; on long time scales, the particles are caged by nearest neighbors and the MSD asymptotically approaches a constant. This asymptotic constant corresponds to twice the variance of the particle's displacement from its equilibrium position [15, 158]. We can prove this as follows,

$$MSD = \langle (x(t + \Delta t) - x(t))^2 \rangle . \quad (8.1)$$

Since a particle fluctuates about an average value,  $\bar{x}$ , eq. 8.1 can be written as,

$$MSD = \langle ((x(t + \Delta t) - \bar{x}) - (x(t) - \bar{x}))^2 \rangle . \quad (8.2)$$

Squaring we get,

$$MSD = \langle (x(t + \Delta t) - \bar{x})^2 \rangle + \langle (x(t) - \bar{x})^2 \rangle - 2 \langle (x(t + \Delta t) - \bar{x})(x(t) - \bar{x}) \rangle . \quad (8.3)$$

The first two terms are equal, and the third term is the correlation of particle distances from the average position at times  $t$  and  $t + \Delta t$ . This correlation vanishes as  $\Delta t \rightarrow \infty$

$$\lim_{\Delta t \rightarrow \infty} MSD = 2 \langle (x(t) - \bar{x})^2 \rangle , \quad (8.4)$$

this is double the variance.

We compute the 3D Lindemann parameter using the measured 2D mean-square displacement and assuming particle fluctuations are isotropic. We use the relation

$$L = \frac{1}{r_{nn}} \sqrt{\frac{3}{4} \langle r^2(\tau \rightarrow \infty) \rangle} \quad (8.5)$$

where  $r_{nn}$  is the crystal nearest neighbor distance, and  $\langle r^2(\tau \rightarrow \infty) \rangle$  is the asymptotic value of the 2D mean square particle displacement.

Notice in the main plot of Fig. 8.6 that  $L$  experiences a change in slope at 24.7 °C. At this temperature the hydrodynamic diameter of the particles as measured by dynamic light scattering is  $\sim 754$  nm, Fig. 8.5, and the nearest neighbor distance derived from pair correlation functions measured by microscopy is  $\sim 750$  nm (Fig. 8.7). Thus at this temperature it is reasonable to assume the particles are close-packed with a volume fraction of  $\sim 0.74$ . Below this temperature the particle motions are constrained, and  $L$  varies less strongly with temperature. With this assumption we can deduce the particle number density. This number density and the measured hydrodynamic radius (Fig. 8.5) determine the particle volume fraction as a function of temperature (upper scale of Fig. 8.6). Particle volume fraction of  $\sim 0.54$  corresponds to temperature of 28.3 °C. Our *best* samples (in terms of “lowest” disorder) that contain very few grain boundaries start to melt at 28.3 °C. Nucleation of melting in these samples is at their center, where there is the largest concentration of partial dislocations. Upon melting, the sample is essentially composed of liquid regions and very ordered (nearly defect free) crystalline regions. On the other hand, in crystals with grain boundaries, the grain boundary interfaces start to disorder at temperatures measurably below 28.3 °C. Interestingly, at 28.3 °C the particle volume fraction is  $\sim 0.54$ , close to the hard sphere melting prediction of 0.545 [181]. The lattice constant in the solid regions, derived from our measurements of the particle pair correlation functions, also decreases sharply near this volume fraction (Fig. 8.8). While our particles are definitely not perfect hard-spheres [199], the melting point suggests they may be approximated reasonably well as such.

The Lindemann melting criterion, which predicts melting for  $L \sim 1/8$  [29], continues to provide a useful benchmark nearly 100 years after it was originally suggested. The data for  $L$  in Fig. 8.6 are taken from deep within the crystalline regions of the sample, below the melting point. At 28.3 °C the sample begins to melt, and a coexistence of liquid and solid domains is observed. In Fig. 8.9 we show local measurements of  $L$  near

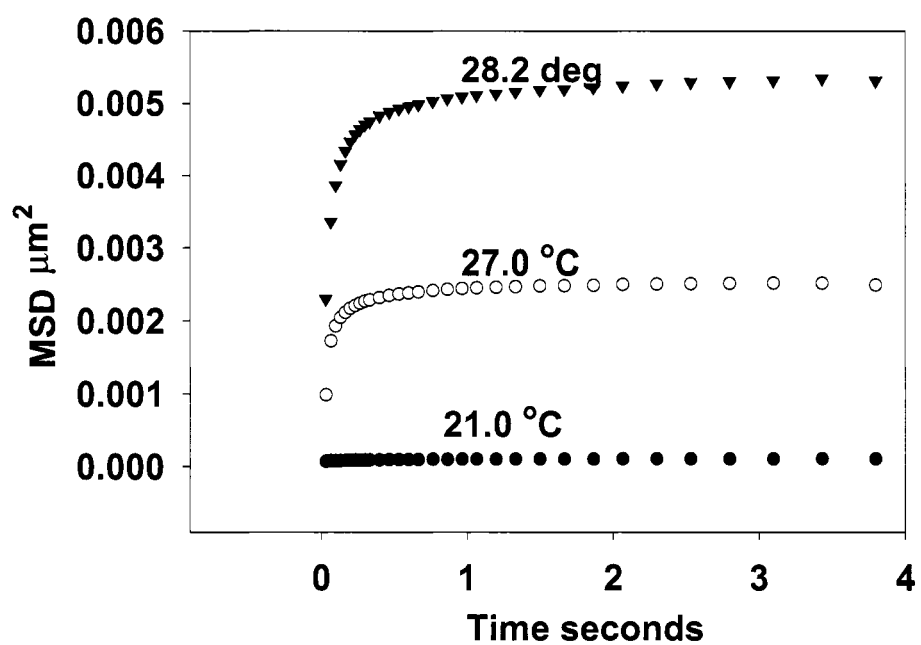


Figure 8.4: Time evolution of 2D particle mean square displacement (MSD);  $L$  is derived from the MSD plateau value.

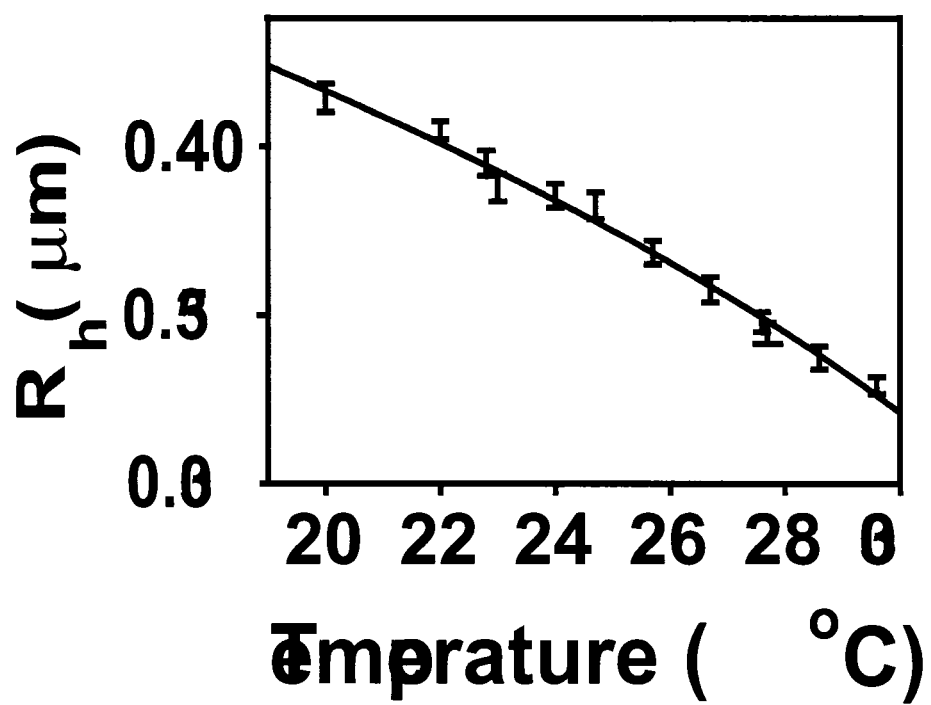


Figure 8.5: Measured microgel particle hydrodynamic radius as a function of temperature.

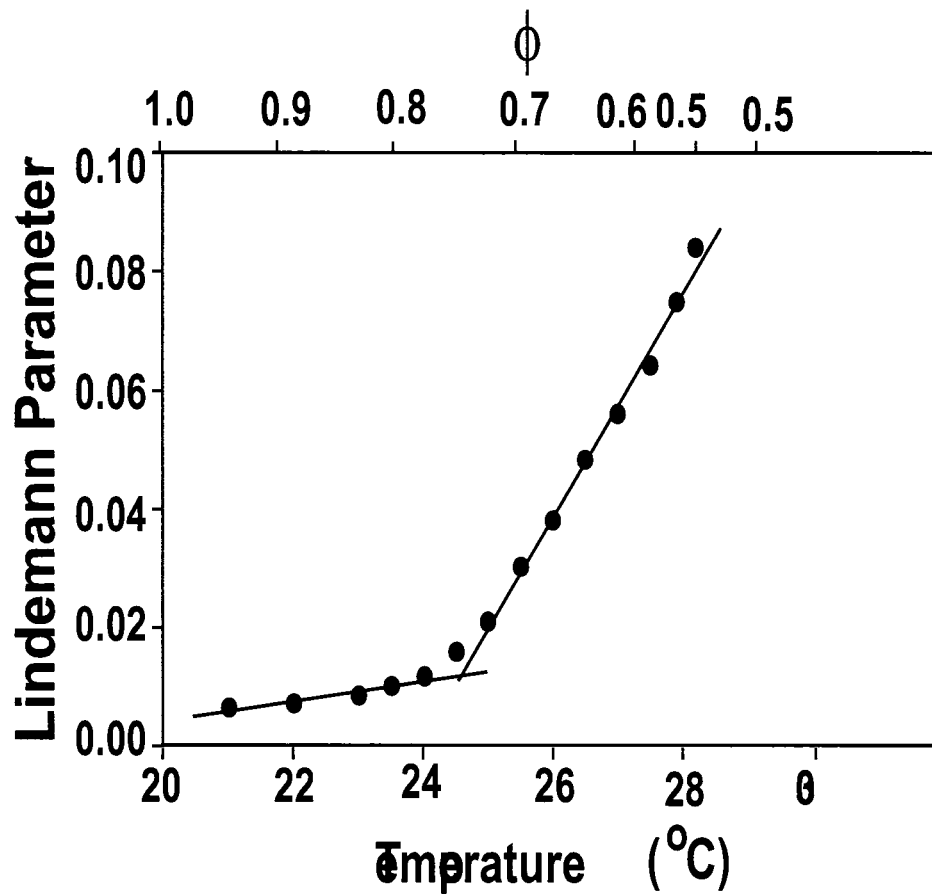


Figure 8.6: Lindemann parameter,  $L$ , as a function of colloidal crystal temperature (and computed particle volume fraction  $\phi$ ). This data are for regions far from defects. The curve exhibits a change in slope at 24.7 °C. The crystal melts at 28.3 °C,  $\phi \sim 0.55$ . The error bars for  $\phi$ ,  $L$ , and temperature are 0.02, .004, and 0.1°C, respectively.

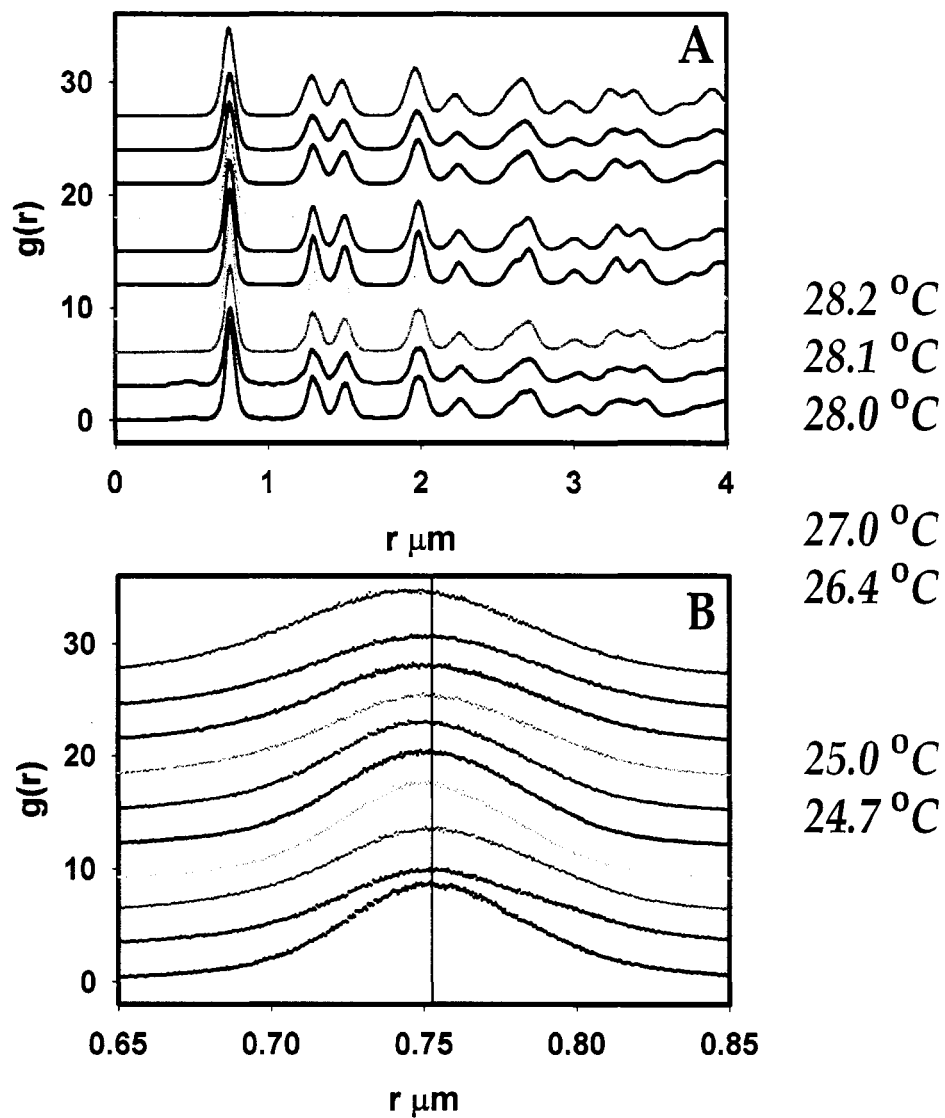


Figure 8.7: Pair correlation function of NIPA crystal at different temperatures. (A) first few peaks and (B) first peak shows that the lattice constant doesn't change as the temperature is increased up to premelting temperature. The base lines are displaced for clarity.

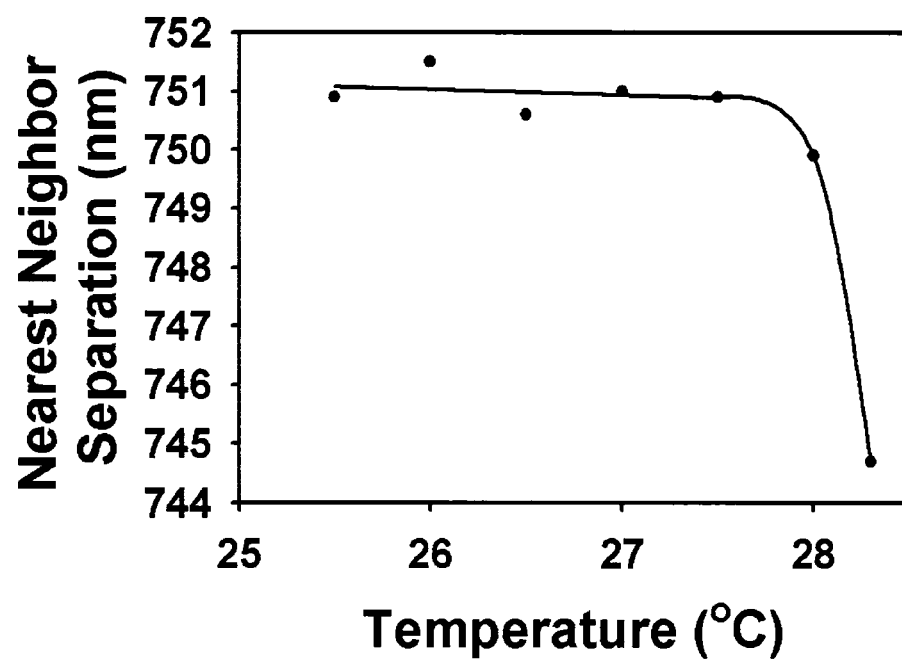


Figure 8.8: The lattice constant (obtained from the pair correlation function) in the solid regions of a NIPA crystal as a function of temperature.



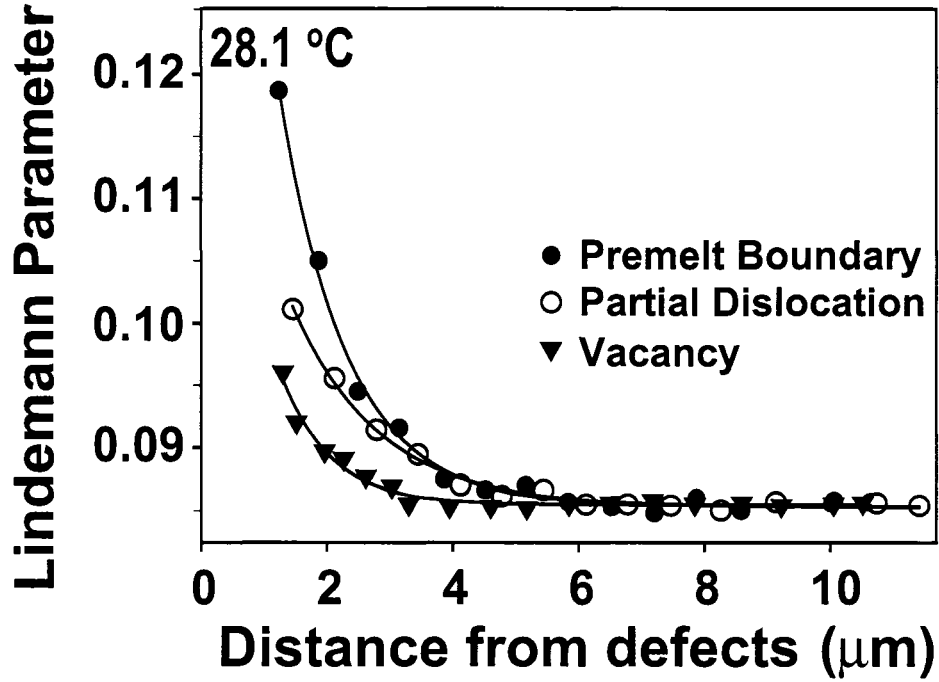


Figure 8.9: The local Lindemann parameter,  $L$ , as a function of distance from a vacancy, a partial dislocation, and a melt front. Within  $1\mu\text{m}$  of the defects, the particle motion was too rapid and calculation of  $L$  was unreliable.

various crystalline defects and near the premelt boundary just before bulk melting ( $28.3^\circ\text{C}$ ). We find that the particle fluctuations in the proximity of these regions are measurably larger than in the bulk crystal. Furthermore, we find the magnitude of these fluctuations decreases approximately exponentially as the measurement position is translated away from the premelt region towards the interior of the bulk crystal. Extrapolation of our exponential fits of  $L$  to zero distance suggest that  $L \sim 0.18$  in the premelt region, twice its interior value of  $\sim 0.085$  at the same temperature. Evidently the greater number of vacancies in the premelted region increases the free volume for particle movement so that the nearby particle fluctuations are large. Even the particles near isolated vacancies have large  $L$ , but the decay of  $L$  to bulk values is fastest from isolated vacancies.

## 8.5 Premelting from grain boundaries

One of the common melting mechanisms exhibited by our colloidal crystals is illustrated in Fig. 8.10. The figure shows a small angle (i.e.  $\sim 13^\circ$ ) grain boundary. The grain boundary is composed of an array of dislocations, one of which is shown in the inset of Fig. 8.10A. Notice that the number of particle nearest neighbors along the grain boundary varies from 5 to 7 (red and blue particles in the inset). These packing mismatches create stress in the crystal near the grain boundary. The dashed line in Fig. 8.10A shows a Shockley partial dislocation that continues into the grain boundary. The region to the right (left) of the dashed line is out-of-focus (in-focus), and the particles in this portion of the image appear darker (whiter) than average. Fig. 8.10B shows the same region at higher temperature (i.e. lower particle volume fraction). In order to minimize the interfacial free energy caused by stress and surface tension, particles near the grain boundary start to premelt. The inset of Fig. 8.10B shows these particles jumping rapidly from one site to another. In contrast, melting is not observed near the partial dislocation (dashed line); its interfacial free energy is apparently less than that of the grain boundary. In Fig. 8.10C the temperature is slightly higher and melting has erupted along the grain boundary. At this stage the sample volume fraction is higher than the bulk melting particle volume fraction, and the melted region has engulfed the partial dislocation. The width of the premelted region continues to increase as the temperature is raised from 28.0 to 28.2 °C, see Fig. 8.10B-D.

It was shown in Sec. 3.4 that surface premelting is a heterogenous process, i.e. not all surfaces premelt at temperatures lower than melting one. In addition the number of premelted layers depends on the crystalline surface. Grain boundary premelting is also a heterogenous process. Figure 8.11 shows a grain boundary that separates two crystallites (right and left). The boundary cuts the two crystallites at two different crystalline surfaces. Each cut has different interfacial energy. Below the melting temperature, melting

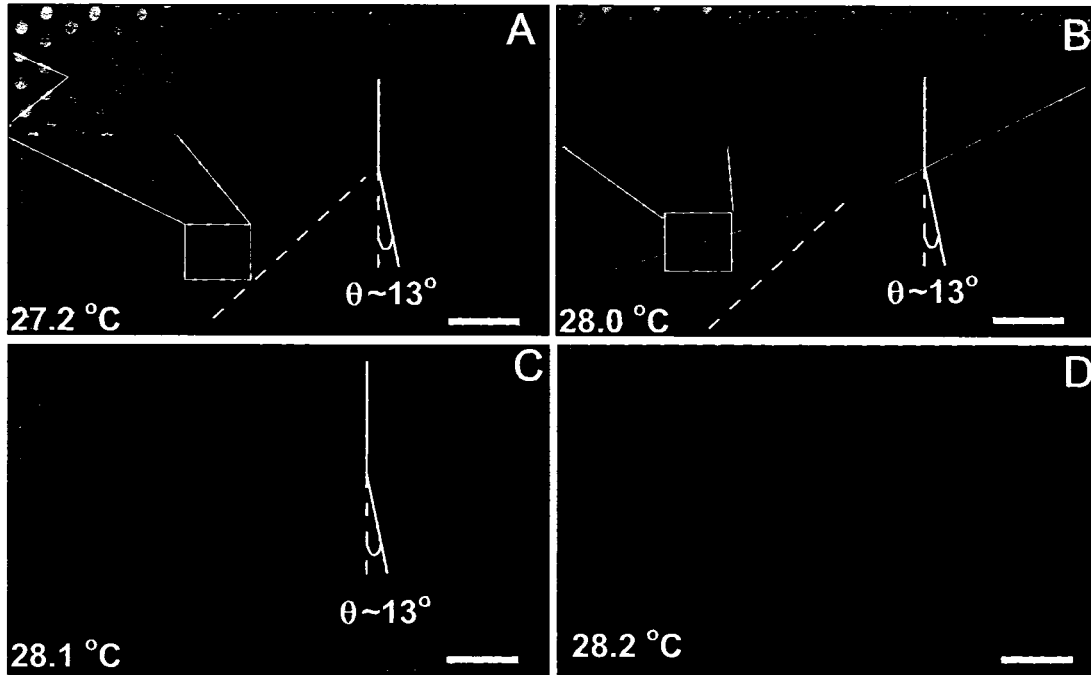


Figure 8.10: Premelting of the colloidal crystal at a grain boundary. The figure shows bright field images at different temperatures (i.e particle volume fractions) of two crystallites separated by a grain boundary ( $\theta \sim 13^\circ$ ). (A) Sample at 27.2 °C. The solid and dashed lines show the grain boundary and a partial dislocation respectively. The grain boundary cuts the two crystals along two different planes (yellow line has two slopes). It is composed of an array of dislocations; the two extra planes are indicated by lines in the inset. (B) Sample at 28.0 °C. The grain boundary starts to premelt; nearby particles undergo liquid like diffusion, inset. The partial dislocation, denoted by the dashed line, is not affected. (C) and (D) The same sample at 28.1 °C and 28.2 °C, respectively. The width of the premelt region near the grain boundary increases. Scale bars are 5  $\mu\text{m}$ .

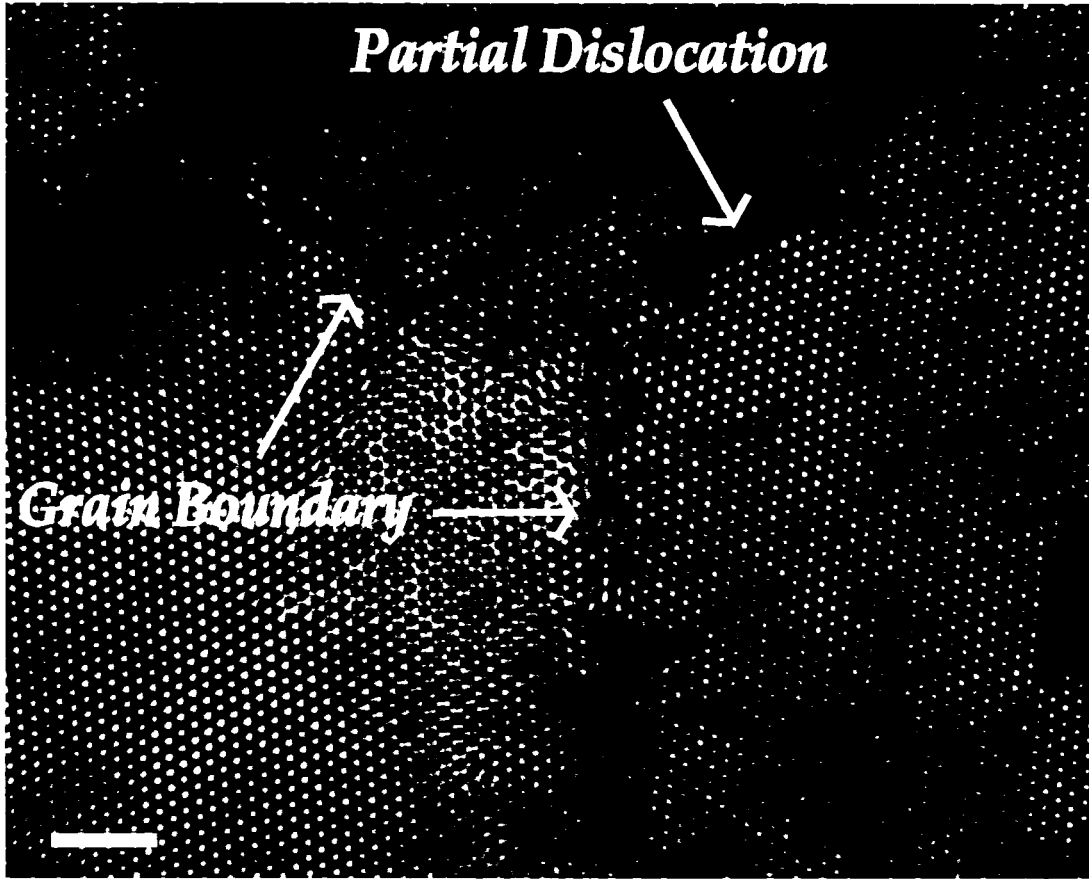


Figure 8.11: Bright field image of a layer in the NIPA particle colloidal crystal showing grain boundaries at 26.4°C. Scale bar is 5  $\mu\text{m}$ .

nucleates at certain positions along the grain boundary, see Fig. 8.12. At higher temperatures (lower volume fraction), the number of melted layers increases at the crystalline surface, while remaining unmelted on the other surfaces, See Fig. 8.13

## 8.6 Premelting from dislocations

In addition to grain boundary premelting, the colloidal crystals display premelting from partial dislocations (Fig. 9.3). This effect is more apparent when the grain boundaries are relatively far from the partial dislocations. Fig. 9.3A and B show images of the 61st layer (green) and the 62nd layer (red and yellow) of the colloidal crystal at 25.0 °C, respectively.

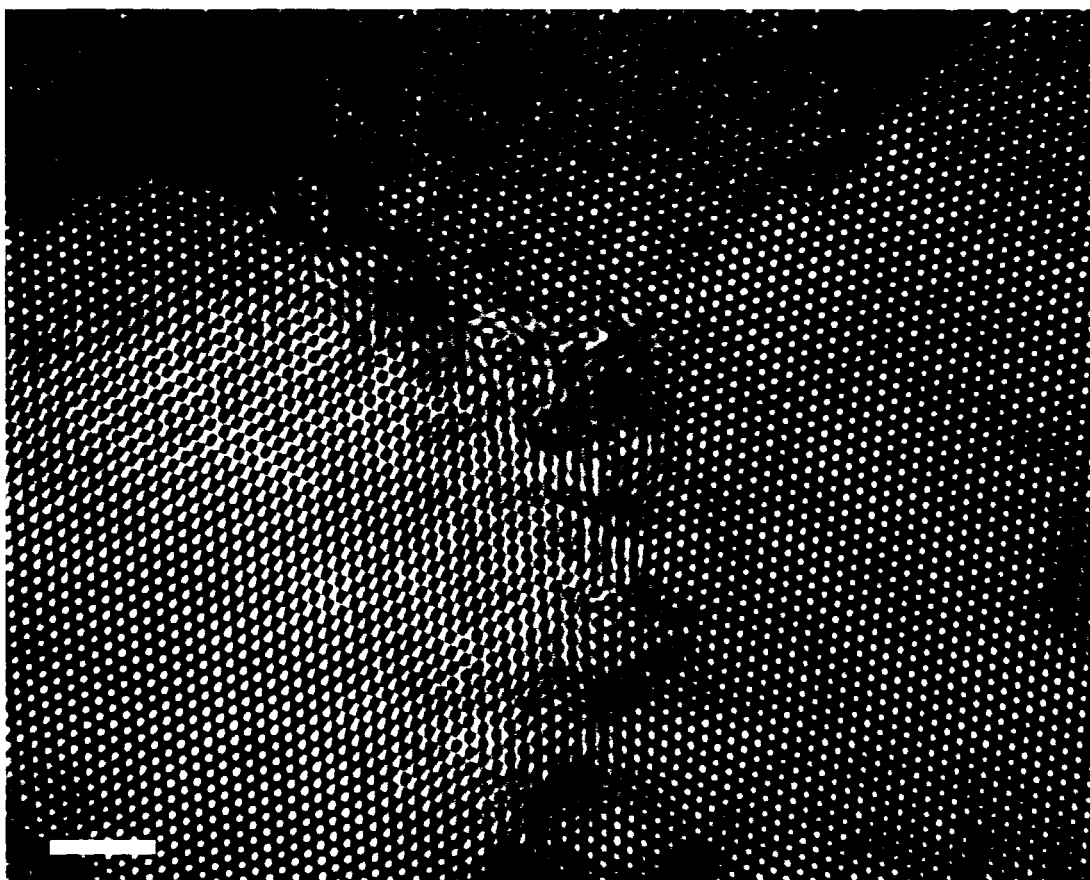


Figure 8.12: Bright field image of the same layer of the NIPA particle colloidal crystal as in Fig. 8.11 showing grain boundaries at 28.2°C. Scale bar is 5  $\mu\text{m}$ .

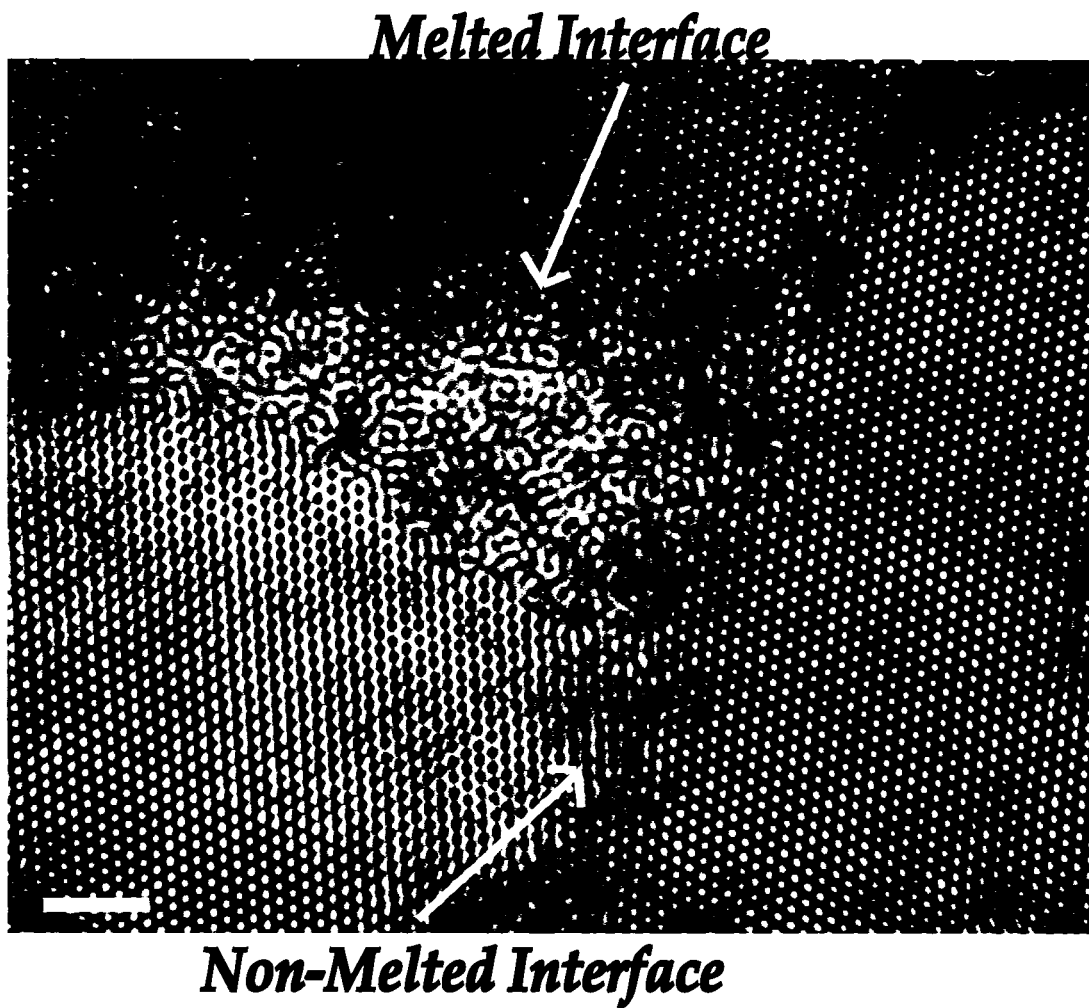


Figure 8.13: Bright field image of the same layer of the the NIPA particle colloidal crystal as in Fig. 8.11 and Fig. 8.12 showing grain boundaries at 28.3°C. Scale bar is 5  $\mu\text{m}$ .

Fig. 9.3C shows a superposition of these layers. Both of these layers represent (111) planes in the crystal. The Burger's circuit in the 61st layer (green) yields a zero Burger's vector, indicating no defect in the layer. Since a dislocation is present in the next layer, some of the particles are slightly out of focus. The Burger's circuit for the 62nd layer (yellow) reveals a Shockley partial dislocation with a Burger's vector of  $\frac{1}{6}(\bar{1}\bar{1}2)$  [91]. The inset contains a three-dimensional illustration of the Shockley dislocation, showing the 61st layer and the undisplaced particles in the 62nd-64th layers in green, and the displaced particles in the 62nd-64th layers in yellow.

In monodisperse nearly-hard sphere colloidal crystals the difference in energy between face-centered cubic (fcc) and hexagonal close-packed (hcp) structures is very small [192, 178], and stacking faults are very common [182]. Shockley partial dislocations arise as a result of these stacking faults. Face centered-cubic crystals stack in the pattern ABCABC along the (111) direction, and hexagonal closed packed crystals stack in the pattern ABAB. The green particles in Fig. 9.3A are in the A positions, while the red and yellow particles are in the B and C positions of the next layer, respectively. This stacking fault opens up gaps between the two close-packed structures within the crystal (two gaps are visible in the image and make an angle of  $120^\circ$  with respect to one another). Nearby particles fluctuate into and out of these gaps. The angle the gaps make with the (111) plane suggest the gaps cut the crystal along (100) planes as shown in the three-dimensional illustration. Finally, Fig. 9.3B shows the 62nd crystal layer at  $28.2^\circ\text{C}$ . At this temperature, which is higher than the grain boundary premelting temperature, the crystal has begun to premelt from the partial dislocation.

## 8.7 Conclusion

We have demonstrated that premelting occurs at grain boundaries and dislocations located within bulk colloidal crystals. The crystals are equilibrium close-packed three-dimensional colloidal structures made from thermally responsive microgel spheres. The

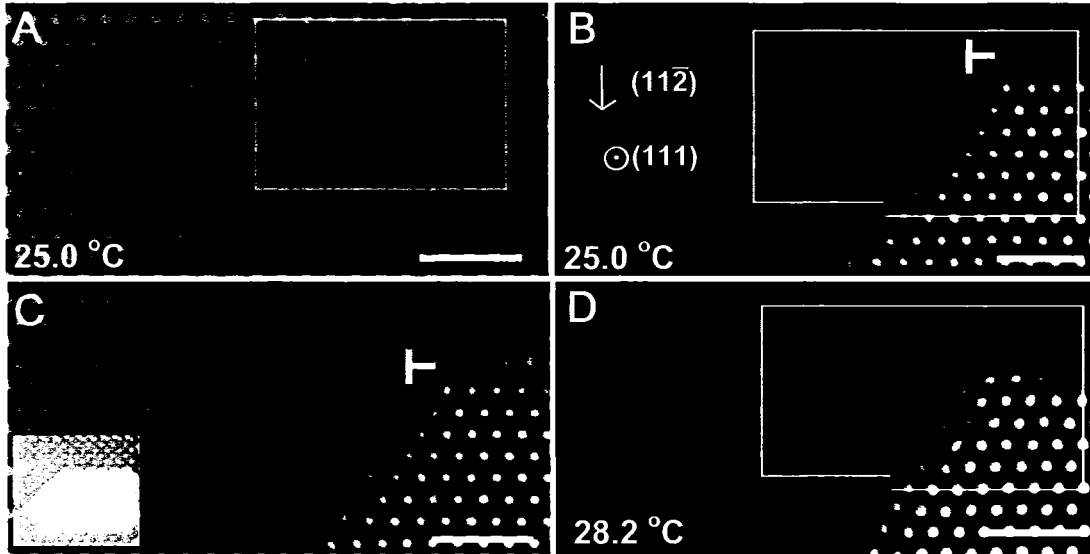


Figure 8.14: Melting of a colloidal crystal initiated at a Shockley partial dislocation in the absence of grain boundaries. (A) and (B) are bright field images of the 61st and 62nd layers at 25.0 °C, respectively. Colloidal particles fluctuate more in the 62nd layer due to the gap created by the dislocation. (C), Superposition of 61st (green) and 62nd (red and yellow) layers. The image shows particles in positions A (green), B (red), and C (yellow). Inset, 3D illustration of the 61st-64th layers (bottom to top) showing the displacement of the yellow spheres in the 62nd-64th layers. (D), 62nd layer at 28.2 °C where the crystal starts to premelt at the dislocation. Scale bars are 3  $\mu\text{m}$ .



thermal response of the microgel enables precision control of particle volume fraction. We used real time video microscopy to track each particle. Our observations confirm an important mechanism for theories of melting. The amount of premelting depends on the nature of the interfaces and defects. Particle tracking has enabled us to study particle fluctuations both nearby and far from these defects in ways that are inaccessible to experimental probes of atomic crystals, revealing the excess free energy in these regions through higher values of the Lindemann parameter. Our observations suggest interfacial free energy is the crucial parameter for premelting, in colloidal and atomic scale crystals.

## **Chapter 9**

# **Melting of lamellar phases in temperature sensitive colloid-polymer suspensions**

### **9.1 Introduction**

Melting of three-dimensional (3D) crystals is among the most ubiquitous phase transitions in nature [135]. In contrast to freezing, melting of 3D crystals has no associated energy barrier. Bulk melting is typically initiated at a pre-melted surface, which then acts as a heterogeneous nucleation site and eliminates the nucleation barrier for the phase transition [49, 217, 215]. In this work we investigate pathways for melting of lamellar phases. In contrast to 3D crystals, lamellar phases have one-dimensional (1D) quasi-long-range order [12, 36, 145]. Additionally while 3D crystals have only one surface between coexisting media, the lamellar phase is a microphase separated state in which the entire bulk is spanned by interfaces between immiscible materials. These phases are frequently built from amphiphilic molecules such as surfactants, lipids, and block copolymers, and

their phase transformations provide insight about membrane biophysics. Although lamellar phases are very common, melting transitions of lamellar into nematic phases are rarely observed. Here we create a novel system that exhibits lamellar-nematic melting, and we show melting of a lamellar phase is fundamentally different from melting of 3D crystalline solids.

We have developed a temperature sensitive aqueous colloidal suspension to carry out these studies. The suspension is composed of lyotropic monodisperse rods of *fd* virus [59, 61], and thermosensitive Poly(N-isopropylacrylamide) (NIPA) polymer. The thermotropic character of the *fd*/NIPA mixture stems from the temperature dependent solubility of NIPA polymer in water [216]. Below its  $\Theta$ -temperature of 31°C, water is a good solvent and NIPA polymer assumes a swollen coil form. Above the  $\Theta$ -temperature water is a poor solvent and NIPA has a collapsed globule form [225]. The resultant mixture forms isotropic, lamellar, and nematic phases depending on temperature and constituent concentration. The lamellar phases resemble those of *fd* with hard spheres, in which layers of spheres are intercalated between layers of rods [2]. Our temperature sensitive aqueous suspension, however, enables us to directly study transitions from one phase to another with optical microscopy.

These *fd*/NIPA solutions are unusual new materials whose lamellar phases differ from those of amphiphilic molecules. The lamellae can swell considerably and melt into a nematic phase, a transition almost never observed in block-copolymer lamellar systems. The different phase behaviors arise primarily because of the rod-like character of the *fd* component, and also because of the absence of covalent cross-links between *fd* and NIPA polymer. The kinetic pathways exhibited by these *fd*/NIPA mixtures are also more complex than those found in temperature-dependent (thermotropic) molecular liquid crystals and concentration-dependent (lyotropic) amphiphilic systems [80, 121]. For example the lamellar phases of *fd*/NIPA mixtures can be swollen to the point where isolated layers (lamellae) of rods are observed. These isolated membrane-like structures

of non-amphiphilic mesogens are stable against mechanical perturbations, melt into nematic droplets, and raise questions about the simplest interacting mesogens capable of assembling into two-dimensional (2D) membranes. Assembly of typical 2D membranes is driven by hydrophobic-hydrophilic interactions [104, 163, 57]: our work indicates that a much simpler system of rods with uniform attractions is capable of assembling into membranes.

Finally, our temperature sensitive *fd*/NIPA solutions offer a powerful new model system for studies of melting. Lyotropic suspensions such as colloids have proven to be ideal for real-time studies of freezing [8, 179, 79]. Melting transitions, however, are much more difficult to investigate with lyotropic colloids. Once a stable ordered phase is obtained, microscopic observation and concurrent concentration variation are required to monitor melting, a challenging experimental task. The advantage of our weakly “thermotropic” *fd*/NIPA polymer based suspension is that simple changes in temperature enable us to prepare the “lyotropic” colloidal system in a metastable ordered state, and then study its melting transition *in situ*. Generally a small increase of temperature increases monomer-monomer attractions and thus decreases the osmotic pressure of the semi-dilute NIPA polymer solution. As a result, water from polymer-rich layers flows into rod-rich layers until osmotic equilibrium is re-established. This phenomena dilutes the rod concentration locally, which in turn can lead to melting of the lamellar phase.

## 9.2 Sample preparation

The *fd*/NIPA mixtures were suspended in a buffer (pH=8.15, 20 mM tris) and were placed between the coverglass and coverslip and then sealed. All observations were made with an inverted microscope (Leica DM IRB) equipped with DIC optics using an oil immersion lens (100X, N.A. 1.4). The temperature of the sample and the objective was controlled with a water circulator. Images were captured by a CCD camera and digitized using NIH-image software. The optical trap for the melting experiments was created with IR light

( $\lambda = 1054$  nm) as described elsewhere [42].

### 9.3 Melting of Bulk Lamellar Phase

The melting behavior of a *fd*/NIPA mixture with high rod concentration is illustrated in Fig. 9.1. Hereafter we refer to this sample as S1. At low temperature (5 °C), the mixture forms a lamellar phase where layers of rods are intercalated with layers of polymers; the polymers are in the semidilute regime (Fig. 9.1a). The measured layer periodicity (1.2  $\mu\text{m}$ ) is much larger than the periodicity of the smectic phase (0.9  $\mu\text{m}$ ) in isolated *fd* suspensions. Dislocations and grain boundaries are observed at low temperature (Fig. 9.1a and i); with increasing temperature they act as nucleation sites for formation of nematic tactoids (Fig. 9.1b). The shape of the nematic tactoid in the smectic background is very similar to the shape of the nematic tactoid in the isotropic background [177].

Although polymer is macroscopically miscible with rods in the lamellar phase, it is highly immiscible with rods in nematic phases [62]. Therefore as the nematic tactoids grow, they expel polymer into coexisting lamellar phase which in turn leads to swelling of the lamellar layers (Fig. 9.1c and j). In a swollen lamellar phase there are regions where individual layers are tightly bound and regions where they are well separated (Fig. 9.1d). Above 15 °C most of the sample is melted into a nematic phase which coexists with a highly swollen lamellar phase. The lamellar phase assumes a form of elongated stripes (Fig. 9.1e and k). Upon increasing the temperature further, the lamellar stripes transform into polymer rich isotropic tactoids which are frequently deformed by a few isolated lamellar layers (Fig. 9.1f-h). Finally, above 17 °C isolated layers melt, and the isotropic tactoids in the nematic background assume their characteristic shape (Fig. 9.1h and l) [177].

Lamellar periodicity is also obtained from the diffraction pattern of lamellar phases (Fig. 9.2a). With increasing temperature the peak simultaneously broadens and shifts to lower angles (Fig. 9.2b and c) indicating swelling of the lamellar phase. Above 15 °C

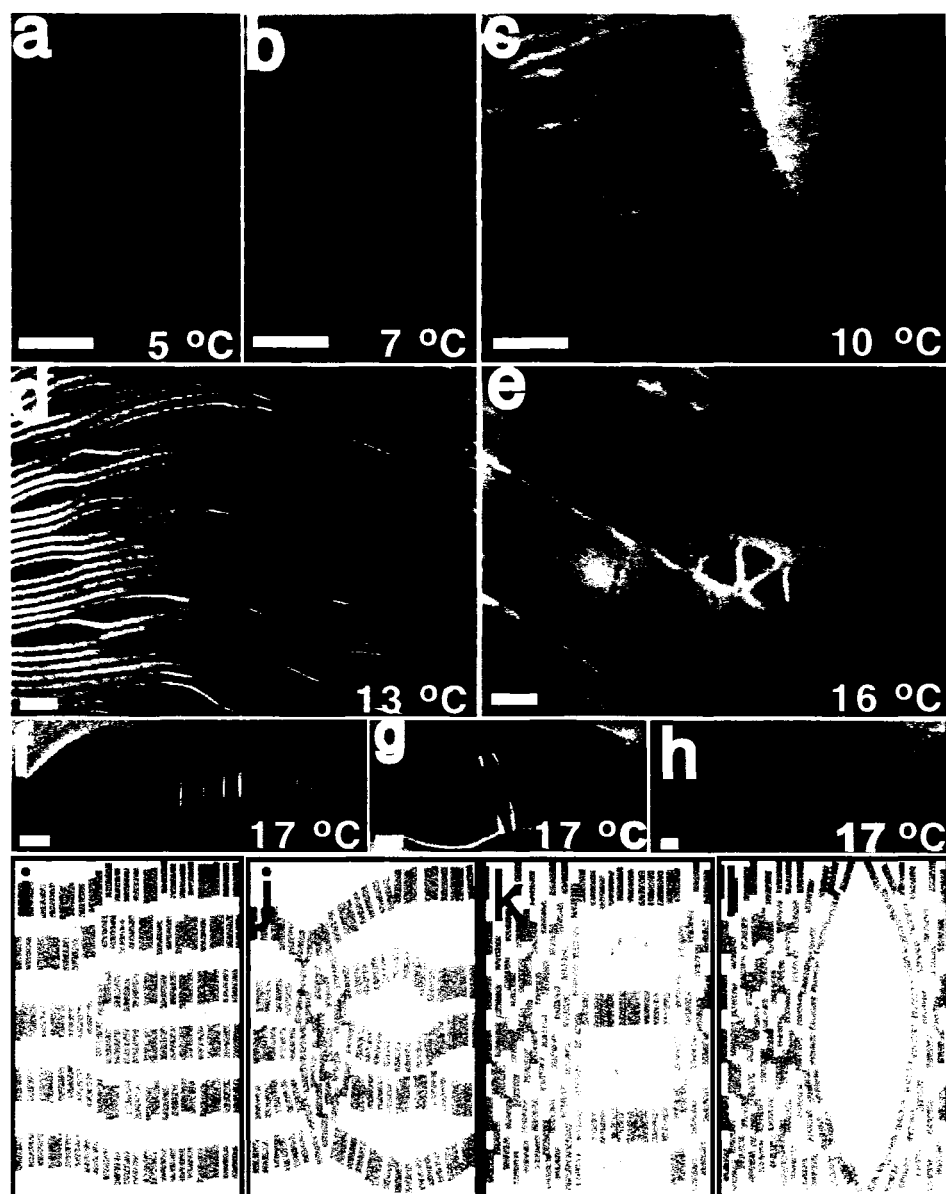


Figure 9.1: Melting behavior of sample S1 (50 mg/ml *fd* and 7.5 mg/ml NIPA). (a) Lamellar phase at low temperature exhibits visible dislocation defects. (b) At 7 °C the dislocation defects act as a site for nucleation of the nematic phase. (c) Nematic domains grow, expelling NIPA polymer into lamellar phase, which leads to swelling of lamellar layers. (d) Swollen lamellar phase. (e) Coexistence between nematic phase and highly swollen lamellar phase. (f-g) Isolated monolayer-deformed isotropic tactoid. (h) Isotropic-nematic coexistence observed at high temperature. (i-l) Illustration of the proposed melting processes of the lamellar rod/polymer mixture. Scale bars are 5  $\mu\text{m}$ .

most of the sample has melted into the nematic: in this case only large forward scattering is observed. At this temperature we still observe highly swollen lamellar stripes with an optical microscope (Fig. 9.1e). When the sample is cooled from the high temperature nematic phase, the lamellar phase forms at 13 °C. Taken together, the observation of coexistence and hysteresis in the heating/cooling cycle suggest lamellar melting into the nematic phase is a first order phase transition with significant nucleation barriers. Moreover the structure of the lamellar phase depends on sample history. The lamellar spacing of samples prepared at high temperature and subsequently cooled is smaller than the lamellar spacing of samples prepared at low temperatures and subsequently heated . In order for the polymer to form an isotropic droplet the lamellar layers must melt. In the next part of the paper we show there is a kinetic barrier for melting of isolated lamellae into a nematic. Therefore with increasing temperature, the sample forms a metastable highly swollen lamellar phase until the individual lamellae overcome a nucleation barrier for melting.

## 9.4 Melting of Lamellar Droplets and Isolated Lamellar Membranes

In the experiments with sample S1, we observed swelling of the lamellar phase. The concentration of lamellar layers in these samples was high, and thus swelling was limited by steric interactions. In order to determine the maximum swelling of the lamellar system, we repeated the melting experiments at much lower *fd* concentration (Fig. 9.3). Hereafter we refer to this sample as S2. At low temperatures most of the sample is an isotropic polymer solution. At temperatures between 21-25 °C we observe coexistence between lamellar droplets (Fig. 9.3a) and isolated lamellae (colloidal membranes) (Fig. 9.3c). The spacing of the layered droplets is 1.2  $\mu\text{m}$ , indicating a lamellar phase similar to S1. The colloidal membranes we observe are composed of a single liquid-like layer of highly

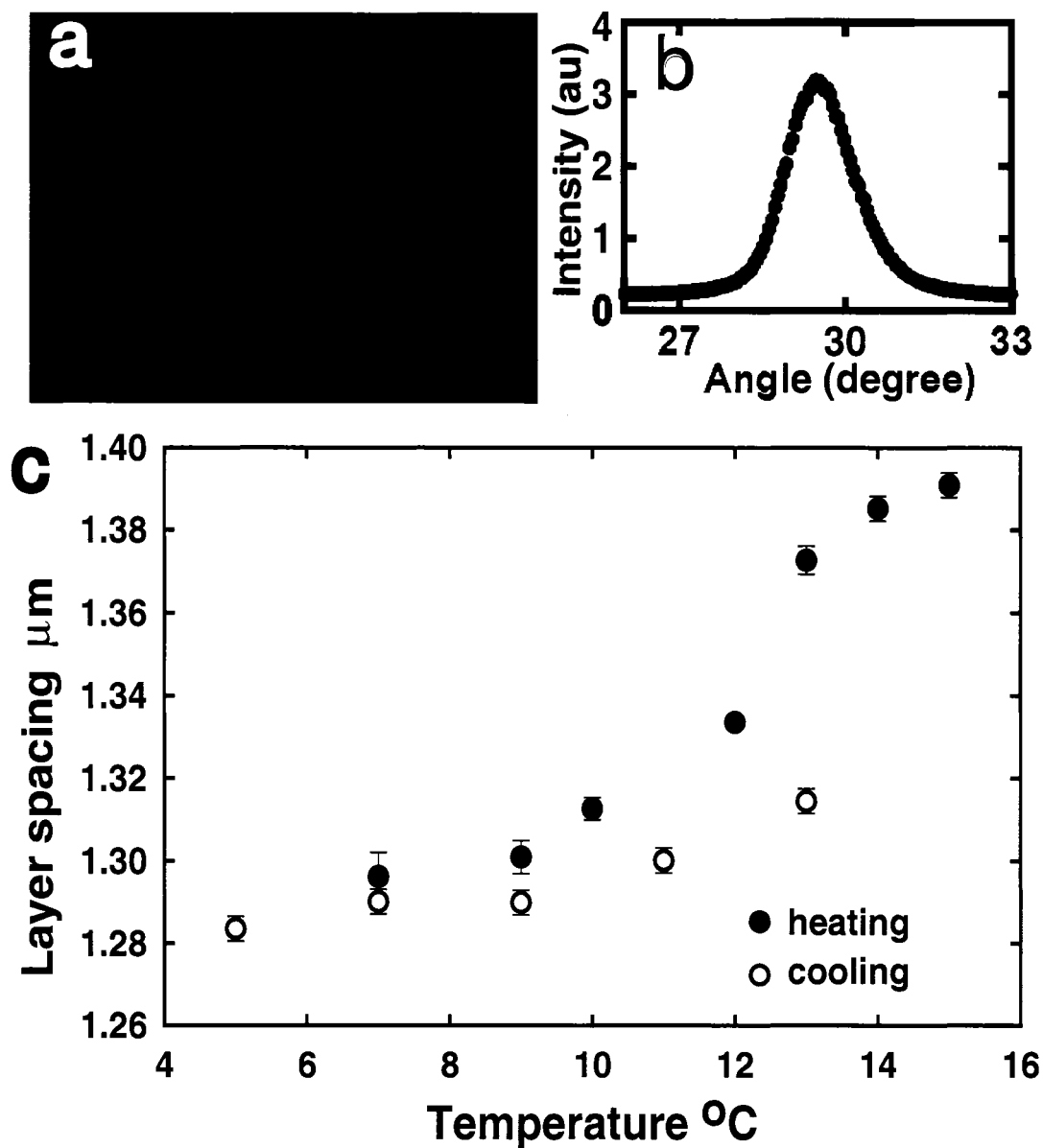


Figure 9.2: Melting of the lamellar sample S1 studied by small angle light scattering. The real space images of the melting behavior are shown in Fig. 9.1.(a) Small angle light scattering pattern of an orientationally disordered lamellar phase at 5°C (b) Angularly averaged intensity profile at 5°C and 13°C. (c) Lamellar periodicity for a sample during heating (filled circles) and cooling (open circles). There is a large hysteresis of layer spacing between heating and cooling cycles.



aligned rods; similar membranes have been observed in athermal rod/polymer mixtures and perhaps in aqueous solutions of  $\beta$ -FeOOH rods [61, 179, 137]. Over time isolated lamellae grow from the interface of the isotropic-lamellar droplet into the isotropic phase; this indicates that single membrane layers are more stable than lamellar droplets.

The coexistence of isolated membranes and lamellar droplets with well defined spacing implies another first order transition, this time from bound to unbound layers. Related binding-unbinding transitions have been studied theoretically in the context of lipid bilayers; the order of these transitions was found to be sensitive to the range of the intermolecular interactions [132, 134]. It is also notable that the suspension of  $fd$  rods usually contain a low volume fraction of dimers. The dimers can affect swelling kinetics of smectic layers and probably increase the stability of the multilayer structure, since they dissolve more easily in a bilayer than in a monolayer.

We have investigated melting and layer reducing dynamics associated with isolated membranes (sample S3). At temperatures above 25 °C lamellar droplets melt into a nematic phase. The mechanism for this melting is similar to melting of the bulk lamellar phase (Fig. 9.3b). The isolated colloidal membranes, however, remain stable at temperatures well above the melting temperature of the multi-layer lamellar droplets. Only upon raising the temperature to almost 30 °C is nucleation of a three-dimensional nematic tactoid observed in the two-dimensional membrane (Fig. 9.3d-f). Once a nematic tactoid is nucleated it quickly grows until the whole membrane melts. If the sample is subsequently cooled, the formation of single layer smectic will be observed only at temperatures below 27 °C. These observations suggest colloidal membranes are metastable superheated structures between 27-30 °C. Nucleation of a 3D nematic tactoid from a 2D membrane requires a large collective fluctuation in which many rods protrude into the third dimension. Our experiments indicate the topological barrier for nucleation of a nematic tactoid is very large. In this sense the melting behavior of lamellae are very different from melting of 3D solids.

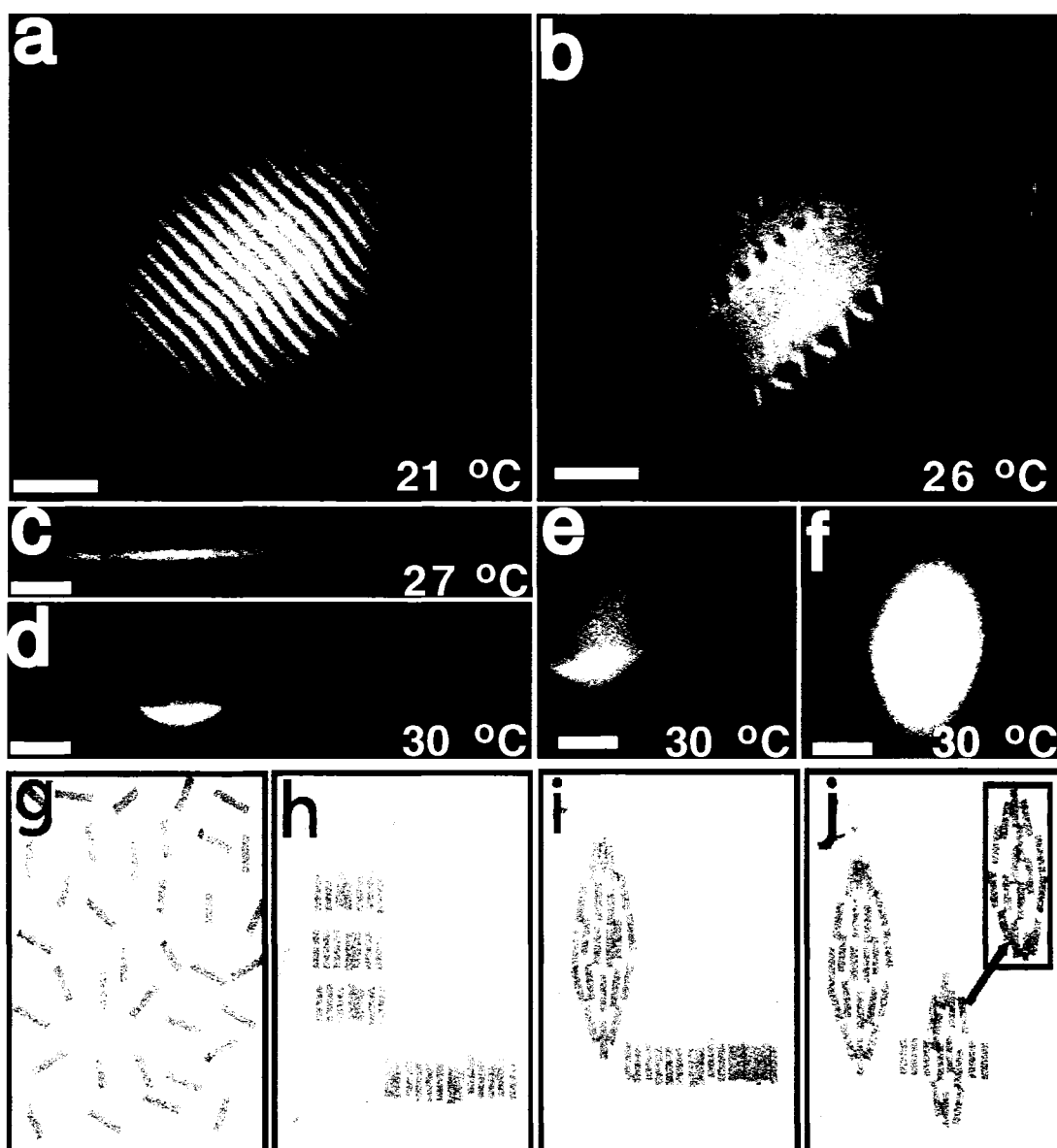


Figure 9.3: Melting behavior of sample S2 (7.5 mg/ml *fd* and 37 mg/ml NIPA). (a) At 24 °C lamellar droplets form in a background isotropic phase. Simultaneously, the formation of isolated layers (shown in image c) is observed. (b) At higher temperature, lamellar droplets melt into a nematic phase by the mechanism described in Fig. 9.1. (c) An isolated membrane is stable for a temperatures from 22-27 °C. (d-f) Sequence of images showing nucleation and growth of a 3D nematic tactoid from an isolated superheated 2D membrane. (g-j) Illustration showing the above described melting processes. At temperatures below 10 °C, the sample forms a miscible isotropic phase. The reason for this is not understood. Scale bars are 5  $\mu\text{m}$ .

## 9.5 Stability of Isolated Lamellar Membranes

Finally we explored the stability of isolated colloidal membranes against external mechanical perturbations (Fig. 9.4). These experiments were done at temperatures below the bulk lamellar melting transition so that the membranes were stable. A silica bead was trapped with an optical tweezer and the colloidal membrane repeatedly punctured (Fig. 9.4a). This mechanical perturbation produced local shear melting of the membrane into a nematic droplet (Fig. 9.4b). We were only able to shear melt membranes at temperatures close to bulk lamellar-nematic phase transition. At lower temperatures the punctured membrane rapidly returned to its equilibrium shape. After the membrane melted, the laser beam is kept in close vicinity of the nematic droplet, locally heating the sample. When the laser beam is on, the nematic droplet coexists with the membrane. The temperature is reduced when the laser beam is turned off, and the nematic droplet quickly freezes into a multilayer smectic structure (Fig. 9.4c). This multilayer smectic structure is unstable and undergoes a sequence of layer reducing transitions until the initial equilibrium membrane configuration is obtained. This experiment provides additional evidence that colloidal membranes are equilibrium structures in this temperature range. By directly visualizing the smectic layers we can discern the mechanism by which a layer reducing transition takes place. The number of layers can be reduced when individual layers slide over each other (Fig 9.4e-f) or by spontaneous formation of dislocations in the main membrane and their subsequent annihilation (Fig. 9.4g-h). These transitions are relevant to layer reducing transitions in superheated smectic films of thermotropic liquid crystals [162].

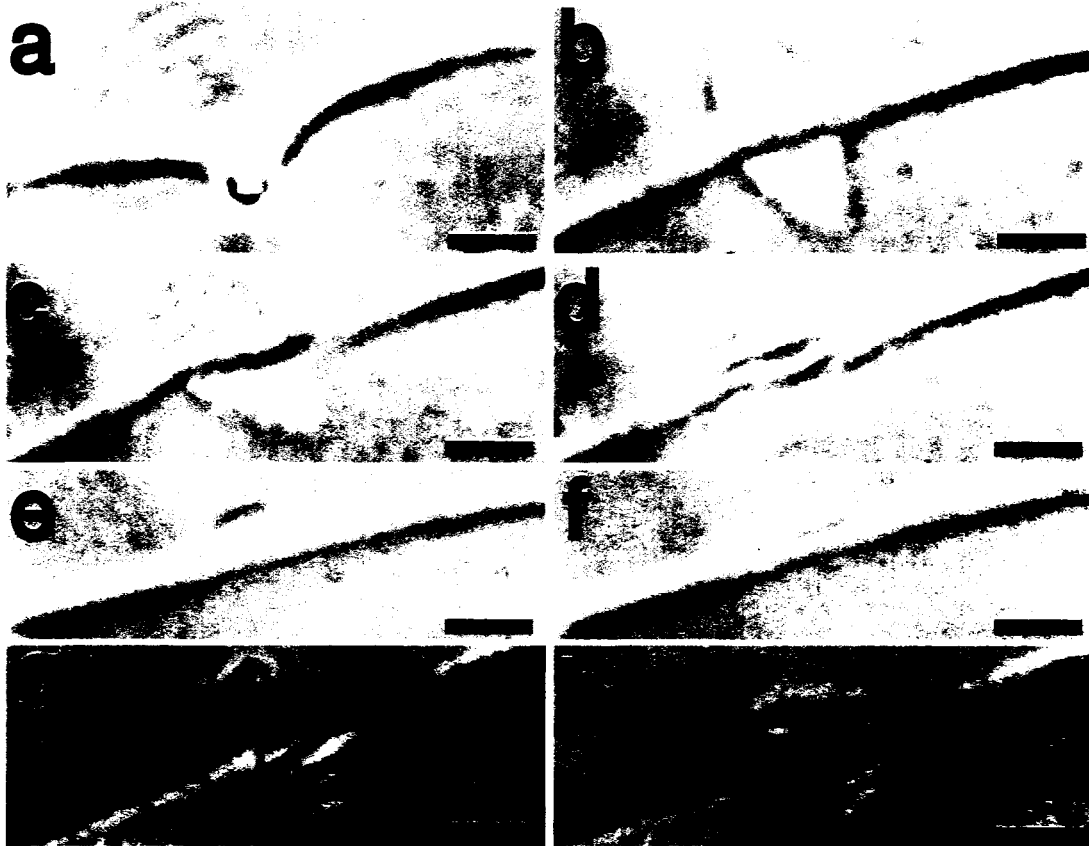


Figure 9.4: Layer reducing transition of a colloidal membrane observed in sample S3 (12 mg/ml *fd*, 31 mg/ml NIPA). The sample temperature is 28 °C, below the melting of the bulk lamellar phase (29 °C). (a) A membrane is repeatedly punctured by a 2.1  $\mu\text{m}$  silica sphere trapped with laser tweezers. (b) A metastable nematic droplet forms due to shear melting. (c) Upon removal of the laser beam the nematic droplet freezes into a multilayer smectic structure. (d-f) The structure undergoes a sequence of layer reducing transitions. (g-h) In a separate experiment a formation of a dislocation in the main membranes is visible. The dislocation subsequently disappears as layers slide over each other which reducing the number of layers by one.

## 9.6 Conclusion

We have investigated the behavior of a novel suspension composed of rod-like *fd* virus and thermo-sensitive polymer Poly(N-isopropylacrylamide) whose phase diagram is temperature and concentration dependent. The system exhibits a rich variety of stable and metastable phases, and, more importantly, provides a unique opportunity to directly observe melting of lamellar phases.

We found that lamellar phase can simultaneously melt into a nematic phase and swell into individual lamellae. The interplay between these two processes creates multiple melting pathways of unexpected complexity. The lamellar phase differs from a conventional 3D crystal in that interfaces between microphase separated layers of aligned rods and polymers in isotropic phase span the entire sample. As a result, melting of these interfaces corresponds to melting of the entire bulk sample and it is possible to superheat the lamellar structure. Typically lamellar phases swell with increasing temperature before melting into the nematic phase. The highly swollen lamellae can even be superheated as a result of topological nucleation barriers that slow formation of nematic phases. Using optical forces we prepare metastable nematic and multilayer structures starting from a single colloidal membrane, and then observe the system evolve back into a single membrane.

Another unique feature of our experiment is the ability to control the phase behavior of a “lyotropic suspension” by temperature, which in turn controls the solvent quality of the polymer phase. This strategy can be used in the future to study phase transitions of other systems in soft condensed matter.

# Chapter 10

## Conclusions and Future Work

In our work, we investigated a very fundamental question: how does melting occur? In 3D crystals we observed that melting begins at grain boundaries and dislocations located within bulk colloidal crystals. The phenomenon is called “premelting”. To show this we developed special colloidal crystals composed of micron-size, nearly hard sphere colloidal microgel particles. The crystals are equilibrium close-packed three-dimensional structures. The microgel particles are also thermally responsive. Thus by changing sample temperature, we precisely varied the volume fraction of particles in the crystal over a significant range, and the crystals were driven from close-packing toward their melting point at lower volume fraction. We used real time video microscopy to track particles in the crystal, and our observations confirmed an important mechanism for theories of melting. The amount of premelting depends on the nature of the interfaces and defects. Particle tracking has enabled us to study particle fluctuations both nearby and far from these defects in ways that are inaccessible to experimental probes of atomic crystals, revealing the excess free energy in these regions through higher values of the Lindemann parameter. Our observations suggest interfacial free energy is the crucial parameter for premelting, in colloidal and atomic scale crystals.

In another set of experiments, we explored how layered 1D lamellar phases melt.

These layered or lamellar structures are fundamentally different from 3-dimensional crystal. Our lamellar phases consisted of layers of temperature sensitive polymer are intercalated between sheets of rods. The structure thus has one-dimensional (1D) quasi-long-range spatial order, and is different from lamellar phases that arise with surfactants, lipids and block copolymers, wherein the molecules are amphiphilic. Specifically our suspensions are composed of monodisperse semiflexible rods of *fd*-virus and temperature-sensitive poly(N-isopropylacrylamide) (NIPA) polymer. The resultant mixture formed isotropic, lamellar, and nematic phases depending on temperature and constituent concentration. We found that lamellar phase can melt into a nematic phase and swell into individual lamellae. The interplay between these two processes creates multiple melting pathways of unexpected complexity. Typically lamellar phases swell with increasing temperature before melting into the nematic phase. The highly swollen lamellae can even be superheated as a result of topological nucleation barriers that slow formation of nematic phases. Using optical forces we prepare metastable nematic and multilayer structures starting from a single colloidal membrane, and then observed the system evolve back into a single membrane. Another unique feature of our experiment was the ability to control the phase behavior of a “lyotropic suspension” by temperature, which in turn controls the solvent quality of the polymer phase. This was the first implementation of this strategy to study phase transitions of other lyotropic systems in soft condensed matter.

Beyond the achievements mentioned above, temperature-sensitive polymers offer a powerful tool to study other fundamental questions in physics. One example is the melting of a two-dimensional crystal lattice. As was mentioned in Sec. 3.2.3, there are interesting open questions about two-dimensional crystal melting. In order to carry this study we need to manufacture a thin cell wherein microgel particles move only in two dimensions. The walls of the cell need to be treated or coated so that particles do not stick on the surfaces. This can be achieved by ultra-cleaning of the surfaces, or by covalently bonding NIPA polymer to the surfaces. The experiment can then be performed in a similar way of our study of three-dimensional colloidal crystal melting.

Another interesting future experiment is to study the sample size dependence in melting and crystallization. Small emulsion droplets of water containing NIPA particles suspended in oil phase can be used for this experiment. Droplet size, the number density of NIPA particles and temperature can all be varied to study their effects on melting and crystallization. Another way to study the sample size dependence in melting and crystallization is to introduce inclusions of small NIPA colloidal crystals into a colloidal crystal made of conventional fixed-size particles. Similar experiments were performed in atomic systems, for example the study of nanosize lead and noble gas inclusions in aluminum [105]. It has been found that when crystals approach certain critical size, many of their properties deviate from the bulk, and the deviations increase as the crystal sizes decrease [10, 106]. Colloidal systems can give more insights into the dynamics and structures of these classes of small crystals.

One can carry out a range of interesting studies of glass-crystal phase transitions using monodisperse NIPA particles. The glassy state can be achieved by quenching the sample from particle volume fractions less than 0.49 (liquid) to particle volume fractions larger than 0.58 (solid). Particle volume fractions then need to be lowered towards the 0.58 value to crystallize the sample. The shear modulus, pair correlation function, particle mean-square-displacement and the rearrangements inside the sample near the transition point can all be measured using video microscopy.

Impurity doping often aggravates or improves the properties of materials. Grain boundaries, in general, play a key role in material strength. Impurities segregate to localized regions along the grain boundary and alter the local bonding environment, thereby strengthening or weakening the material [25, 229]. NIPA colloidal crystals can be doped with different sizes and shapes of impurity particles. We can then study the dynamics of the impurities nearby and away from grain boundaries and defects. The effect of impurity segregation on the premelting behavior of grain boundaries can be also studied. Crystal elastic moduli, nearby and away from grain boundaries, can be measured using microrheology techniques [34].



Finally, we can study the jamming transition using polydisperse NIPA particles. Packing fractions can be tuned easily in this system. Measuring the divergence of the first peak in the pair correlation function, the vanishing of the shear modulus, and the excess number of overlapping neighbors can all be done using confocal and video microscopy [152].

In total, the future is very bright for new experiments with these novel systems.

# Bibliography

- [1] K. F. A. Pavlovska and E. Bauer. *Surface Science* **221**, 233 (1989).
- [2] M. Adams, Z. Dogic, S. L. Keller, and S. Fraden. Entropically driven microphase transitions in mixtures of colloidal rods and spheres. *Nature* **393**, 349 (1998).
- [3] B. J. Alder, W. G. Hoover, and D. A. Young. Studies in molecular dynamics .v. high-density equation of state and entropy for hard disks and spheres. *Journal Of Chemical Physics* **49**, 3688 (1968).
- [4] B. J. Alder and T. E. Wainwright. Phase transition for a hard sphere system. *Journal Of Chemical Physics* **27**, 1208 (1957).
- [5] A. M. Alsayed, M. F. Islam, J. Zhang, P. J. Collings, and A. G. Yodh. Premelting at defects within bulk colloidal crystals. *Science* **309**, 1207 (2005).
- [6] A. Alsayed, Z. Dogic, , and A. Yodh. Melting of lamellar phases in temperature sensitive colloid-polymer suspensions. *Physical Review Letters* **93**, 057801 (2004).
- [7] T. Amiya, Y. Hirokawa, Y. Hirose, Y. Li, and T. Tanaka. Reentrant phase-transition of N-isopropylacrylamide gels in mixed-solvents. *Journal Of Chemical Physics* **86**, 2375 (1987).
- [8] V. J. Anderson and H. N. W. Lekkerkerker. Insights into phase transition kinetics from colloidal science. *Nature* **416**, 811–815 (2002).

- [9] D. E. Angelescu, C. K. Harrison, M. L. Trawick, R. A. Register, and P. M. Chaikin. Two-dimensional melting transition observed in a block copolymer. *Physical Review Letters* **95**, 025702 (2005).
- [10] F. Banhart, E. Hernandez, and M. Terrones. Extreme superheating and supercooling of encapsulated metals in fullerenelike shells. *Physical Review Letters* **90**, 185502 (2003).
- [11] R. Barnett and U. Landman. Surface premelting of Cu(110). *Physical Review B* **44**, 3226 (1991).
- [12] F. S. Bates. Polymer-polymer phase behavior. *Science* **251**, 898–905 (1991).
- [13] B. J. Berne and R. Pecora. *Dynamic Light Scattering: With Applications to Chemistry, Biology, and Physics*. Dover Publications, Inc. Mineola, New York, Dover edition (2000).
- [14] P. G. Bolhuis and D. Frenkel. Tracing the phase boundaries of hard spherocylinders. *J. Chem. Phys.* **106**, 668–687 (1997).
- [15] J. Bongers and H. Versmold. Microscopic investigations of the single particle dynamics in colloidal crystals. *Journal Of Chemical Physics* **104**, 1519 (1996).
- [16] M. Born and E. Wolf. *Principles Of Optics*. Pergamon Press Elmsford, New York, 6<sup>th</sup> edition (1980).
- [17] U. Breuer, O. Knauff, and H. Bonzel. *Journal Of Vacuum Science And Technology* **A8**, 2489 (1990).
- [18] J. Q. Broughton and G. Gilmer. *Physical Review Letters* **56**, 2692 (1986).
- [19] J. Broughton and G. Gilmer. Molecular-dynamics investigation of the crystal fluid interface. 3. dynamical properties of fcc crystal vapor systems. *Journal Of Chemical Physics* **79**, 5119 (1983).

- [20] J. Broughton and G. Gilmer. Molecular-dynamics investigation of the crystal fluid interface .1. bulk properties. *Journal Of Chemical Physics* **79**, 5095 (1983).
- [21] J. Broughton and G. Gilmer. Molecular-dynamics investigation of the crystal fluid interface .2. structures of the fcc (111), (100), and (110) crystal vapor systems. *Journal Of Chemical Physics* **79**, 5105 (1983).
- [22] J. Broughton and G. Gilmer. Molecular-dynamics investigation of the crystal fluid interface .6. excess surface free-energies of crystal liquid-systems. *Journal Of Chemical Physics* **84**, 5759 (1986).
- [23] J. Broughton and G. Gilmer. Molecular-dynamics of the crystal fluid interface .5. structure and dynamics of crystal melt systems. *Journal Of Chemical Physics* **84**, 5749 (1986).
- [24] J. Broughton and L. Woodcock. Molecular-dynamics study of surface melting. *Journal Of Physics C-Solid State Physics* **11**, 2743 (1978).
- [25] P. Buban, K. Matsunaga, J. Chen, N. Shibata, W. Y. Ching, T. Yamamoto, and Y. Ikuhara. Grain boundary strengthening in alumina by rare earth impurities. *Science* **311**, 212 (2006).
- [26] L. Burakovsky, D. L. Preston, and R. R. Silbar. Melting as a dislocation-mediated phase transition. *Physical Review B* **61**, 15011 (2000).
- [27] B. Busch and T. Gustafsson. *Surface Science* **407**, 7 (1998).
- [28] D. A. G. C. S. Johnson. *Laser Light Scattering*. Dover Publications, Inc. Mineola, New York dover edition edition (1994).
- [29] R. W. Cahn. *Nature* **413**, 582 (2001).
- [30] P. Carnevali, F. Ercolessi, and E. Tosatti. Melting and nonmelting behavior of the Au(111) surface. *Physical Review B* **36**, 6701 (1987).

- [31] P. Carnevali, F. Ercolessi, and E. Tosatti. Surface melting behavior of Au(111). *Surface Science* **189**, 645 (1987).
- [32] P. M. Chaikin and T. C. Lubensky. *Principles of Condensed Matter Physics*. Cambridge University Press Cambridge, United Kingdom 2<sup>nd</sup> edition (2000).
- [33] D. S. Chekmarev, D. W. Oxtoby, and S. A. Rice. Melting of a quasi-two-dimensional metallic system. *Physical Review E* **63**, 051502 (2001).
- [34] D. Chen, E. Weeks, J. Crocker, M. Islam, R. Verma, J. Gruber, A. Levine, T. Lubensky, and A. Yodh. Rheological microscopy: Local mechanical properties from microrheology. *Physical Review Letters* **90**, 108301 (2003).
- [35] E. Chen, R. Barnett, and U. Landman. Surface premelting of Ni(110). *Physical Review B* **41**, 439 (1990).
- [36] J. T. Chen, E. L. Thomas, C. K. Ober., and G. P. Mao. Self-assembled smectic phases in rod-coil block-copolymers. *Science* **273**, 343 (1996).
- [37] K. Chen, H. Liu, X. Li, Q. Han, and Z. Hu. Molecular-dynamics simulation of local-structure of aluminum and copper in supercooled liquid and solid-state by using eam. *Journal Of Physics-Condensed Matter* **7**, 2379 (1995).
- [38] T. A. Cherepanova and A. V. Stekolnikov. Statistical-models of crystal-surfaces - 1st-principle approaches. *Journal Of Crystal Growth* **99**, 88 (1990).
- [39] T. A. Cherepanova, A. V. Stekolnikov, and P. Bennema. Weighted-density functional-approach for the solid liquid interfaces in electrolytes. *Journal Of Crystal Growth* **129**, 202 (1993).
- [40] G. Ciccotti, M. Guillope, and V. Pontikis. High-angle grain-boundary premelting transition: A molecular-dynamics study. *Physical Review B* **27**, 5576 (1983).

- [41] J. C. Crocker and D. G. Grier. *Journal Of Colloid And Interface Science* **179**, 298 (1996).
- [42] J. C. Crocker, J. A. Matteo, A. D. Dinsmore, and A. G. Yodh. Entropic attraction and repulsion in binary colloids probed with a line optical tweezer. *Physical Review Letters* **82**, 4352–4355 (1999).
- [43] W. A. Curtin. Density-functional theory of crystal-melt interfaces. *Physical Review B* **39**, 6775 (1989).
- [44] W. A. Curtin and N. W. Ashcroft. *Physical Review A* **32**, 2909 (1985).
- [45] W. A. Curtin and N. W. Ashcroft. *Physical Review Letters* **59**, 2385 (1987).
- [46] J. Däges, H. Gleiter, and J. H. Perepezko. *Mat. Res. Soc. Symp. Proc.* **57** (1986).
- [47] U. Dahmen, S. Hagege, F. Faudot, T. Radetic, and E. Johnson. Observations of interface premelting at grain-boundary precipitates of Pb in Al. *Philosophical Magazine* **84**, 2651 (2004).
- [48] M. Daoud and C. E. Williams. *Soft Matter Physics*. Springer Germany 1<sup>st</sup> edition (1999).
- [49] J. G. Dash. *Reviews Of Modern Physics* **71**, 1737 (1999).
- [50] J. G. Dash, H. Fu, and J. S. Wettlaufer. *Reports On Progress In Physics* **58**, 115 (1995).
- [51] J. D. Debord. *Journal Of Physical Chemistry B* **104**, 6327 (2000).
- [52] J. D. Debord, S. Eustis, S. B. Debord, M. T. Lofye, and L. A. Lyon. *Advanced Materials* **14**, 658 (2002).
- [53] S. B. Debord and L. A. Lyon. *Journal Physical Chemistry B* **107**, 2927 (2003).

- [54] A. R. Denton and N. W. Ashcroft. *Physical Review A* **39**, 1919 (1989).
- [55] P. Deymier, A. Taiwo, and Kalonji. A grain-boundary phase-transition studied by molecular-dynamics. *Acta Metallurgica* **35**, 2719 (1987).
- [56] D. Dhara and P. Chatterji. Swelling and deswelling pathways in non-ionic poly(N-isopropylacrylamide) hydrogels in presence of additives. *Polymer* **41**, 6133 (2000).
- [57] B. Discher, Y.-Y. Won, D. Ege, J.-M. Lee, F. Bates, D. Discher, and D. Hammer. Tough vesicles made from diblock copolymers. *Science* **284**, 1143–1146 (1999).
- [58] S. Divinski, M. Lohmann, C. Herzig, B. Straumal, B. Baretzky, and W. Gust. Grain-boundary melting phase transition in the Cu-Bi system. *Physical Review B* **71**, 104104 (2005).
- [59] Z. Dogic and S. Fraden. The smectic phase in a colloidal suspension of semi-flexible virus particle. *Physical Review Letters* **78**, 2417 (1997).
- [60] Z. Dogic and S. Fraden. Cholesteric phase in virus suspensions. *Langmuir* **16**, 7820–7824 (2000).
- [61] Z. Dogic and S. Fraden. Development of model colloidal liquid crystals and the kinetics of the isotropic-smectic transition. *Philosophical Transactions Of The Royal Society Of London Series A* **359**, 997 (2001).
- [62] Z. Dogic, D. Frenkel, and S. Fraden. Enhanced stability of the layered phases in parallel spherocylinders due to addition of hard spheres. *Physical Review E* **62**, 3925–3934 (2000).
- [63] Z. Dogic, A. P. Philipse, S. Fraden, and J. K. G. Dhont. Concentration-dependent sedimentation of colloidal rods. *Journal Of Chemical Physics* **113**, 8368 (2000).

- [64] Z. Dogic, K. R. Purdy, E. Grelet, M. Adams, and S. Fraden. Isotropic-nematic phase transition in suspensions of filamentous virus and the neutral polymer dextran. *Physical Review E* **69**, 051702 (2004).
- [65] H. Dosch, T. Hofer, J. Peisl, and R. Johnson. *Europhysics Letters* **15**, 527 (1991).
- [66] S. F. Edwards and M. Warner. *Philosophical Magazine* **A 40**, 257 (1979).
- [67] S. F. Edwards and M. Warner. *Philosophical Magazine* **40**, 257 (1979).
- [68] J. D. Eerden, T. V. D. Berg, J. Huinink, and H. Knops. *Journal Of Crystal Growth* **128**, 57 (1993).
- [69] J. D. Eerden, H. Knops, and A. Roos. *Journal Of Chemical Physics* **96**, 714 (1991).
- [70] M. Eisele and W. Burchard. *Macromolecular Chemistry And Physics* **191**, 169 (1990).
- [71] R. Evans. The nature of the liquid-vapour interface and other topics in the statistical mechanics of non-uniform, classical fluid. *Advances In Physics* **28**, 143 (1979).
- [72] H. Feil, Y. Bae, F. Jan, and S. Kim. Effect of comonomer hydrophilicity and ionization on the lower critical solution temperature of N-isopropylacrylamide copolymers. *Macromolecules* **26**, 2496 (1993).
- [73] D. Frenkel, H. Lekkerkerker, and A. Stroobants. Thermodynamic stability of smectic phase in a system of hard rods. *Nature* **332**, 822 (1988).
- [74] J. Frenkel. *Kinetic Theory Of Liquids*. Clarendon Oxford (1946).
- [75] J. W. M. Frenken, B. J. Hinch, J. P. Toennies, , and C. Will. *Physical Review B* **41**, 938 (1990).



- [76] J. W. M. Frenken, P. M. J. Marée, and J. F. V. D. Veen. Observation of surface-initiated melting. *Physical Review B* **34**, 7506 (1986).
- [77] J. W. M. Frenken and J. F. V. D. Veen. Observation of surface melting. *Physical Review Letters* **54**, 134 (1985).
- [78] Y. Furukawa, M. Yamamoto, and T. Kuroda. *J. Cryst. Growth* **125**, 665 (1987).
- [79] U. Gasser, E. R. Weeks, A. Schofield, P. N. Pusey, and D. A. Weitz. Real-space imaging of nucleation and growth in colloidal crystallization. *Science* **292**, 258–262 (2001).
- [80] P. G. D. Gennes and J. Prost. *The Physics Of Liquid Crystals*. Oxford Science second edition (1993).
- [81] N. Georgiev, A. Pavlovska, and E. Bauer. *Physical Review B* **52**, 2878 (1995).
- [82] A. V. D. Gon, R. Smith, J. Gay, and D. O'Connor. *Surface Science* **227**, 143 (1990).
- [83] R. Goodman and G. Somorjai. *The Journal Of Chemical Physics* **52**, 6325 (1970).
- [84] H. H. V. Grunberg, P. Keim, K. Zhan, and G. Maret. Elastic behavior of 2D crystal near melting. *Physical Review Letters* **93**, 0255703 (2004).
- [85] M. M. H. Häkkinen. *Physical Review B* **46**, 1725 (1992).
- [86] A. D. J. Haymet. Theory of the equilibrium liquid-solid transition. *Ann. Rev. Phys. Chem.* **38**, 89 (1987).
- [87] A. D. J. Haymet and D. W. Oxtoby. *Journal Of Chemical Physics* **74**, 2559 (1981).
- [88] A. D. J. Haymet and D. W. Oxtoby. A molecular theory for freezing - comparison of theories, and results for hard-spheres. *Journal Of Chemical Physics* **84**, 1769 (1986).

- [89] T. Hellweg, C. Dewhurst, E. Bruckner, K. Kratz, and W. Eimer. *Colloid And Polymer Science* **278**, 972 (2000).
- [90] S. Hirotsu, Y. Hirokawa, and T. Tanaka. Volume-phase transitions of ionized N-isopropylacrylamide gels. *Journal Of Chemical Physics* **87**, 1392 (1987).
- [91] J. P. Hirth and J. Lothe. *Theory Of Dislocations*. Wiley New York second edition (1982).
- [92] P. S. Ho, T. Kwok, T. Nguyen, C. Nitta, and S. Yip. Vacancy motions in an aluminum bicrystal. *Journal Of Metals* **36**, 30 (1984).
- [93] P. S. Ho, T. Kwok, T. Nguyen, C. Nitta, and S. Yip. Observation of local melting in an aluminum bicrystal by molecular-dynamics simulation. *Scripta Metallurgica* **19**, 993 (1985).
- [94] P. Hohenberg and W. Kohn. *Physical Review* **136**, B864 (1964).
- [95] M. Hosino, H. Nakano, and H. Kimura. Nematic-Smectic transitions in an aligned rod system. *J. Phys. Soc. Jpn.* **46**, 1709 (1979).
- [96] A. Hoss, M. Nold, P. V. Blanckenhagen, and O. Mayer. *Physical Review B* **45**, 8714 (1992).
- [97] J. J. Hoyt, J. Garvin, E. B. Webb, and M. Asta. An embedded atom method interatomic potential for the Cu-Pb system. *Modelling And Simulation In Materials Science And Engineering* **11**, 287 (2003).
- [98] T. E. Hsieh and R. W. Balluffi. *Acta Metallurgica* **37**, 1637 (1989).
- [99] S. Iarlori, P. Carnevali, F. Ercolessi, and E. Tosatti. Dynamics of a liquid-metal surface. *Europhysics Letters* **10**, 329 (1989).

- [100] S. Iarlari, P. Carnevali, F. Ercolessi, and E. Tosatti. Surface melting behavior of Au(111). *Surface Science* **211**, 55 (1989).
- [101] H. Inomata, N. Wada, Y. Yagia, S. Goto, and S. Saito. *Polymer* **36**, 875 (1995).
- [102] S. Inoué and K. R. Spring. *Video Microscopy*. Plenum Press New York And London second edition (1997).
- [103] J. M. J.C. Heyraud and J. Bermond. *Journal Of Crystal Growth* **98**, 355 (1989).
- [104] S. A. Jenekhe and X. L. Chen. Self-assembled aggregates of rod-coil block copolymers and their solubilization and encapsulation of fullerenes. *Science* **279**, 1903–1907 (1998).
- [105] E. Johnson, H. H. Andersen, and U. Dahmen. Nanoscale lead and noble gas inclusions in aluminum: Structures and properties. *Microscopy Research and Technique* **64**, 356 (2004).
- [106] E. Johnson, A. Johnson, U. Dahmen, S. Chen, and T. Fujii. Shapes and sizes of nanoscale Pb inclusions in al. *Mater Sci Eng A* **304306**, 187193 (2001).
- [107] A. B. H. R. D. Kamien and T. C. Lubensky. Microscopic origin of cholesteric pitch. *Physical Review Letters* **78**, 1476 (1997).
- [108] H. Kawasaki, S. Sasaki, and H. Maeda. *Journal Of Physical Chemistry B* **101**, 4184 (1997).
- [109] S. D. Kevan and D. A. Shirley. High-resolution angle-resolved-photoemission studies of the m-point surface state on Cu (001). *Physical Review B* **22**, 542 (1980).
- [110] R. Kikuchi and J. Cahn. Grain boundary melting transition in a two-dimensional lattice-gas model. *Physical Review B* **21**, 1893 (1980).

- [111] E. D. Klug. *Journal Of Polymer Science Part C-Polymer Symposium* **36**, 491 (1971).
- [112] W. Kohn and L. J. Sham. *Physical Review* **140**, A1133 (1964).
- [113] E. Kokufuta, Y. Zhang, and T. Tanaka. Saccharide-sensitive phase-transition of a lectin-loaded gel. *Nature* **351**, 302 (1991).
- [114] E. Kokufuta, Y. Zhang, T. Tanaka, and A. Mamada. Effects of surfactants on the phase-transition of poly(N-isopropylacrylamide) gel. *Macromolecules* **26**, 1053 (1993).
- [115] D. E. Koppel. *Journal Of Chemical Physics* **57**, 4814 (1972).
- [116] J. Kosterlitz and D. Thouless. *Journal Of Physical Chemistry* **6**, L181 (1973).
- [117] J. Krim, J. Coulomb, and J. Bouzidi. *Physical Review Letters* **58**, 583 (1987).
- [118] K. Kubota, S. Fujishige, and I. Ando. Single-chain transition of poly(N-isopropylacrylamide) in water. *Journal Of Physical Chemistry* **94**, 5154 (1990).
- [119] D. Kuhlmann-Wilsdorf. Theory of melting. *Physical Review* **140**, A1599 (1965).
- [120] A. Landa, H. Hakkinen, R. Barnett, P. Wynblatt, and U. U. Landman. Molecular dynamics study of disordering, roughening, and premelting of the Pb(110) surface. *Journal Of Non-Crystalline Solids* **207**, 767 (1996).
- [121] F. C. Larche, J. Appell, G. Porte, P. Bassereau, and J. Marignan. Extreme swelling of a lyotropic lamellar liquid crystal. *Physical Review Letters* **56**, 1700–1703 (1986).
- [122] J. Larese and Q. Zhang. *Physical Review Letters* **64**, 922 (1990).

- [123] A. W. C. Lau, K. H. Lin, and A. G. Yodh. Entropic interactions in suspensions of semiflexible rods: Short range effects of flexibility. *Physical Review E* **66**, 020401 (2003).
- [124] T. D. Lee and C. N. Yang. *Physical Review* **87**, 410 (1952).
- [125] R. Leidl and H. Wagner. *Journal Of Chemical Physics* **98**, 4142 (1993).
- [126] Y. Lereah, G. Deutscher, and R. Kofman. *Europhysics Letters* **8**, 53 (1989).
- [127] Y. Li and T. Tanaka. Phase-transitions of gels. *Annual Review Of Materials Science* **22**, 243 (1992).
- [128] F. A. Lindemann. *Z.Phys.* **11**, 609 (1910).
- [129] R. Lipowsky. *Physical Review Letters* **49**, 1575 (1982).
- [130] R. Lipowsky. *Physical Review B* **28**, 3983 (1983).
- [131] R. Lipowsky. *Physical Review Letters* **57**, 2876 (1986).
- [132] R. Lipowsky. Structure and dynamics of membranes. In R. Lipowsky and E. Sackmann, editors, *Generic Interactions Of Flexible Membranes*. pages 521–602. Elsevier (1995).
- [133] R. Lipowsky, U. Breuer, K. C. Prince, and H. P. Bonzel. Multicomponent order parameter for surface melting. *Physical Review Letters* **62**, 913 (1989).
- [134] R. Lipowsky and S. Leibler. Unbinding transitions of interacting membranes. *Physical Review Letters* **56**, 2541–2544 (1986).
- [135] H. Lowen. *Physics Report* **237**, 249 (1994).
- [136] J. Luo, V. K. Gupta, and D. H. Yoon. Segregation-induced grain boundary pre-melting in nickel-doped tungsten. *Applied Physics Letters* **87**, 231902 (2005).

- [137] H. Maeda and Y. Maeda. Liquid crystals formation in suspension of hard rodlike colloidal particles: Direct observation of particle arrangement and self-ordering behavior. *Physical Review Letters* **90**, 018303 (2003).
- [138] E. S. Matsuo and T. Tanaka. Kinetics of discontinuous volume-phase transition of gels. *Journal of Chemical Physics* **89**, 1695 (1988).
- [139] S. Mizushima. *J. Phys. Soc. Jpn* **15**, 70 (1960).
- [140] S. Modesti, V. Dhanak, M. Sancrotti, A. Santoni, B. Persson, and E. Tosatti. *Physical Review Letters* **73**, 1951 (1994).
- [141] N. F. Mott. *Proc. R. Soc. London* **A215**, 1 (1952).
- [142] C. A. Murray and D. G. Grier. Video microscopy of monodisperse colloidal systems. *Annu. Rev. Phys. Chem.* **47**, 421 (1996).
- [143] C. A. Murray, W. O. Sprenger, and R. A. Wenk. *Physical Review B* **42**, 688 (1990).
- [144] C. A. Murray and D. H. V. Winkle. *Physical Review Letters* **58**, 1200 (1987).
- [145] M. Muthukumar, C. K. Ober, and E. L. Thomas. Competing interactions and levels of ordering in self-organizing polymeric materials. *Science* **277**, 1225–1232 (1997).
- [146] D. Nelson and B. Halperin. *Physical Review B* **19**, 2457 (1979).
- [147] T. Nguyen, P. Ho, T. Kwok, C. Nitta, and S. Yip. Thermal structural disorder and melting at a crystalline interface. *Physical Review B* **46**, 6050 (1992).
- [148] T. Nguyen, P. S. Ho, T. Kwok, C. Nitta, and S. Yip. Grain-boundary melting transition in an atomistic simulation-model. *Physical Review Letters* **57**, 1919 (1986).

- [149] T. Nguyen and S. Yip. Molecular-dynamics study of a bicrystal at elevated-temperatures. *Materials Science And Engineering A* **107**, 15 (1989).
- [150] T. Nguyen, S. Yip, and D. Wolf. Molecular-dynamics study of high-temperature grain-boundary stability in Au (100)  $\sigma=29$  bicrystal model. *Journal De Physique* **49**, 381 (1988).
- [151] A. Oakawa. *J. Phys. Soc. Jpn* **15**, 2191 (1960).
- [152] C. O'Hern, L. Silbert, A. Liu, and S. Nagel. Jamming at zero temperature and zero applied stress: The epitome of disorder. *Physical Review E* **68**, 011306 (2003).
- [153] R. Ohnesorge, H. Lowen, and H. Wagner. Density-functional theory of surface melting. *Physical Review A* **43**, 2870 (1991).
- [154] R. Ohnesorge, H. Lowen, and H. Wagner. Density-functional theory of crystal fluid interfaces and surface melting. *Physical Review E* **50**, 4801 (1994).
- [155] R. Ohnesorge, H. Lowen, and H. Wagner. Density functional theory of crystal-fluid interfaces and surface melting. *Physical Review E* **50**, 4801 (1994).
- [156] R. Ohnesorge, H. Lowen, and H. Wagner. Surface melting - a density-functional approach. *Physical Chemistry Chemical Physics* **98**, 877 (1994).
- [157] R. Ohnesorge, H. Lowen, and H. Wagner. Surface melting - a density-functional approach. *Physical Chemistry Chemical Physics* **98**, 303 (1994).
- [158] Y. N. Ohshima and I. Nishio. Colloidal crystal: Beadspring lattice immersed in viscous media. *Journal Of Chemical Physics* **114**, 8649 (2001).
- [159] L. Onsager. The effects of shape on the interaction of colloidal particles. *Ann. Ny Acad. Sci.* **51**, 627 (1949).

- [160] K. Otake, H. Inomata, M. Konno, and S. Saito. Thermal-analysis of the volume phase-transition with N-isopropylacrylamide gels. *Macromolecules* **23**, 283 (1990).
- [161] D. W. Oxtoby. Density functional methods in the statistical mechanics of materials. *Annual Review Of Materials Research* **32**, 39 (2002).
- [162] S. Pankratz, P. M. Johnson, A. Paulson, and C. C. Huang. Kinetics of layer thinning transitions in overheated smectic films. *Physical Review E* **61**, 6689–6695 (2000).
- [163] S. Park, J. H. Lim, S. W. Chung, and C. A. Mirkin. Self-assembly of mesoscopic metal-polymer amphiphiles. *Science* **303**, 348–351 (2004).
- [164] A. Pavlovska, H. Steffen, and E. Bauer. *Surface Science* **234**, 143 (1990).
- [165] A. Pavlovska, M. Tikhov, G. Yingjun, and E. Bauer. *Surface Science* **278**, 303 (1992).
- [166] L. Pedemonte, G. Bracco, R. Beikler, E. Taglauer, A. Robin, and W. Heiland. *Surface Science* **532-535**, 13 (2003).
- [167] F. L. Pedrotti and L. S. Pedrotti. *Introduction To Optics*. Prentice-Hall Lebanon, Indiana 2nd edition edition (1993).
- [168] R. Pelton. Temperature-sensitive aqueous microgels. *Advances In Colloid And Interface Science* **85**, 1 (2000).
- [169] R. H. Pelton and P. Chibante. Preparation of aqueous lattices with N-isopropylacrylamide. *Colloids And Surfaces* **20**, 247 (1986).
- [170] J. K. Percus. *The Many Body Problem, Proceedings*. Interscience Publisher New York (1957).



- [171] M. S. Pettersen, M. J. Lysek, and D. L. Goodstein. Melting in multilayer adsorbed films. *Physical Review B* **40**, 4938 (1989).
- [172] S. Phillpot, J. F. Lutsko, D. Wolf, and S. Yip. Molecular-dynamics study of lattice-defect-nucleated melting in silicon. *Physical Review B* **40**, 2831 (1989).
- [173] B. Pluis, D. Frenkel, and J. F. V. D. Veen. Surface-induced melting and freezing ii. a semi-empirical landau-type model. *Surface Science* **239**, 282 (1990).
- [174] B. Pluis, A. W. D. V. D. Gon, J. W. M. Frenken, and J. F. V. D. Veen. Crystal-face dependence of surface melting. *Physical Review Letters* **59**, 2678 (1987).
- [175] M. Polcik, L. Wilde, and J. Haase. *Physical Review Letters* **78**, 491 (1997).
- [176] V. Pontikis and P. Sindzinger. *Physica Scripta* **19**, 375 (1987).
- [177] P. Prinsen and P. V. D. Schoot. Shape and director-field transformation of tactoids. *Physical Review E* **68**, 021701 (2003).
- [178] S. Pronk and D. Frenkel. Can stacking faults in hard-sphere crystals anneal out spontaneously? *Journal Of Chemical Physics* **110**, 4589 (1999).
- [179] K. R. Purdy, Z. Dogic, S. Fraden, A. Ruhm, L. Lurio, and S. G. J. Mochrie. Measuring the nematic order of suspensions of colloidal fd virus by x-ray diffraction and optical birefringence. *Physical Review E* **67**, 031708 (2003).
- [180] P. N. Pusey. Freezing and melting: Action at grain boundaries. *Science* **309**, 1198 (2005).
- [181] P. N. Pusey and W. V. Megen. Phase-behavior of concentrated suspensions of nearly hard colloidal spheres. *Nature* **320**, 340 (1986).
- [182] P. N. Pusey and W. V. Megen. Phase-behaviour of concentrated suspensions of nearly hard colloidal spheres. *Nature* **320**, 340 (1989).

- [183] R. A. Quinn and J. Goree. Experimental test of 2D melting through disclination unbinding. *Physical Review E* **64**, 051404 (2001).
- [184] L. Radzihovsky, E. Frey, and D. Nelson. Novel phase reentrant melting of 2D colloidal crystals. *Physical Review E* **63**, 031503 (2001).
- [185] T. V. Ramakrishnan and M. Yussouff. *Physical Review B* **19**, 2775 (1979).
- [186] H. Ringsdorf, J. Venzmer, and F. M. Winnik. Fluorescence studies of hydrophobically modified poly(N-isopropylacrylamides). *Macromolecules* **24**, 1678 (1991).
- [187] W. F. Saam and C. Ebner. Renormalized density-functional theory of nonuniform superfluid He-4 at zero temperature. *Physical Review B* **12**, 923 (1975).
- [188] W. F. Saam and C. Ebner. Density-functional theory of simple classical fluids .1. surfaces. *Physical Review A* **14**, 2264 (1976).
- [189] W. F. Saam and C. Ebner. Density-functional theory of classical systems. *Physical Review A* **15**, 2566 (1977).
- [190] W. F. Saam and C. Ebner. New phase-transition phenomena in thin argon films. *Physical Review Letters* **38**, 1486 (1977).
- [191] W. F. Saam and C. Ebner. Classical fluid structure near solid substrates - comparison of different theories. *Physical Review A* **17**, 1768 (1978).
- [192] P. Schall, I. Cohen, D. A. Weitz, and F. Spaepen. Visualization of dislocation dynamics in colloidal crystals. *Science* **305**, 1944 (2004).
- [193] H. G. Schild. Poly (N-isopropylacrylamide) - experiment, theory and application. *Progress In Polymer Science* **17**, 163 (1992).
- [194] H. Senff and W. J. Richtering. *Chemical Physics* **111**, 1705 (1999).
- [195] M. Shibayama, Y. Fujikawa, and S. Nomura. *Macromolecules* **29**, 6535 (1996).

- [196] M. Shibayama and T. Tanaka. Volume phase-transition and related phenomena of polymer gels. *Advances In Polymer Science* **109**, 1 (1993).
- [197] M. Shibayama, T. Tanaka, and C. Han. Small-angle neutron-scattering study on weakly charged temperature sensitive polymer gels. *Journal Of Chemical Physics* **97**, 6842 (1992).
- [198] M. Stieger, P. Lindner, and W. Richtering. Structure formation in thermoresponsive microgel suspensions under shear flow. *Journal Of Physics-Condensed Matter* **16**, S3861 (2004).
- [199] M. Stieger, J. S. Pedersen, P. Lindner, and W. Richtering. Are thermoresponsive microgels model systems for concentrated colloidal suspensions? a rheology and small-angle neutron scattering study. *Langmuir* **20**, 7283 (2004).
- [200] M. Stieger and W. Richtering. Shear-induced phase separation in aqueous polymer solutions: Temperature-sensitive microgels and linear polymer chains. *Macromolecules* **36**, 8811 (2003).
- [201] M. Stieger, W. Richtering, J. S. Pedersen, and P. Lindner. Small-angle neutron scattering study of structural changes in temperature sensitive microgel colloids. *Journal Of Chemical Physics* **120**, 6197 (2004).
- [202] P. Stoltze, J. Norskov, and U. Landman. Disordering and melting of aluminum surfaces. *Physical Review Letters* **61**, 440 (1988).
- [203] P. Stoltze, J. Norskov, and U. Landman. The onset of disorder in Al(110) surfaces below the melting-point. *Surface Science* **220**, 693 (1989).
- [204] K. J. Strandburg. *Reviews Of Modern Physics* **60**, 161 (1988).
- [205] J. Tang and S. Fraden. Isotropic-cholesteric phase transition in colloidal suspensions of filamentous bacteriophage fd. *Liquid Crystals* **19**, 459–467 (1995).

- [206] J. Tang and S. Fraden. Temperature dependence of the flexibility of fd: Behavior of the isotropic - cholesteric phase boundary and magnetic birefringence. *Biopolymers* **39**, 13 (1996).
- [207] P. Tarazona. *Molecular Physics* **52**, 81 (1984).
- [208] P. Tarazona. *Physical Review A* **31**, 2672 (1985).
- [209] U. Tartaglino, T. Zykova-Timan, F. Ercolessi, and E. Tosatti. Melting and non-melting of solid surfaces and nanosystems. *Physics Reports* **411**, 291321 (2005).
- [210] W. Theis and K. Horn. *Physical Review B* **51**, 7157 (1995).
- [211] T. Tokuhito, T. Amiya, A. Mamada, and T. Tanaka. Nmr-study of poly(N-isopropylacrylamide) gels near phase-transition. *Macromolecules* **24**, 2936 (1991).
- [212] F. D. Tolla, F. Ercolessi, and E. Tosatti. *Physical Review Letters* **74**, 3201 (1995).
- [213] O. Tomagnini, F. Ercolessi, S. Iarlori, F. D. Tolla, and E. Tosatti. *Physical Review Letters* **76**, 1118 (1996).
- [214] R. Trittbach, C. Grütter, and J. Bilgram. *Physical Review B* **50**, 2529 (1994).
- [215] J. F. V. D. Veen. *Surface Science* **433-435**, 1 (1999).
- [216] X. Wang and C. Wu. Light-scattering study of coil-to-globule transition of a poly(N-isopropylacrylamide) chain in deuterated water. *Macromolecules* **32**, 4299 (1999).
- [217] R. W. Cahn. *Nature* **323**, 668 (1989).
- [218] X. Wen, R. B. Meyer, and D. L. D. Caspar. Observation of smectic-A ordering in a solution of rigid-rod-like particles. *Physical Review Letters* **63**, 2760 (1989).

- [219] R. S. Williams, P. S. Wehner, J. Stöhr, , and D. A. Shirley. Thermally induced breakdown of the direct-transition model in copper. *Physical Review Letters* **39**, 302 (1977).
- [220] K. G. Wilson. The renormalization-group and critical phenomena. *Reviews Of Modern Physics* **55**, 583–600 (1983).
- [221] F. M. Winnik. Fluorescence studies of aqueous-solutions of poly(N-isopropylacrylamide) below and above their lcst. *Macromolecules* **23**, 233 (1990).
- [222] F. Winnik. Photophysics of preassociated pyrenes in aqueous polymer-solutions and in other organized media. *Chemical Reviews* **93**, 587 (1993).
- [223] T. A. Witten. Insights from soft condensed matter. *Reviews of Modern Physics* **71**, S367 (1999).
- [224] W. W. Wood and J. D. Jacobson. Preliminary results from a recalculation of the monte carlo equation of state of hard spheres. *Journal Of Chemical Physics* **27**, 1207 (1957).
- [225] C. Wu and X. Wang. Globule-to-coil transition of a single homopolymer chain in solution. *Physical Review Letters* **80**, 4092 (1998).
- [226] J. Wu, G. Huang, and Z. Hu. *Macromolecules* **36**, 440 (2003).
- [227] J. Wu, B. Zhou, and Z. Hu. Phase behavior of thermally responsive microgel colloids. *Physical Review Letters* **90**, 048304 (2003).
- [228] X. S. Wu, A. S. Hoffman, and P. Yager. Synthesis and characterization of thermally reversible macroporous poly(n-isopropylacrylamide) hydrogels. *Journal Of Polymer Science Part A-Polymer Chemistry* **30**, 2121 (1992).
- [229] M. Yamaguchi, M. Shiga, and H. Kaburaki. Grain boundary decohesion by impurity segregation in a nickel-sulfur system. *Science* **307**, 393 (2005).

- [230] C. N. Yang and T. D. Lee. *Physical Review* **87**, 404 (1952).
- [231] H. N. Yang, K. Fang, G. C. Wang, and T. M. Lu. Vacancy-induced disordering in the Pb(100) surface. *Physical Review B* **44**, 1306 (1991).
- [232] A. P. Young. *Physical Review B* **19**, 1855 (1979).
- [233] Y. Zhang, T. Tanaka, and M. Shibayama. *Nature* **360**, 142 (1992).
- [234] J. Zhu, M. Li, R. Rogers, W. Meyer, R. H. Ottewill, S.-. S. S. Crew, W. B. Russel, and P. M. Chaikin. Crystallization of hard-sphere colloids in microgravity. *Nature* **387**, 883–885 (1997).